N° d'ordre :...............

**Université de Saida- Dr. Moulay Tahar**

**Faculté des Sciences**

**Département de Physique**

# Thèse

Présentée pour obtenir le diplôme de

## Doctorat 3ème Cycle

**Spécialité : Physique du Rayonnement**

**Filière : Physique**

Par :

**KHODJA Djamila**

Thème :

## Ab-initio Investigation of the Physical Properties of Some Te Based Half Heusler Alloys

Thèse soutenue le 06/07/2022   devant le jury composé de :

| N° | Nom et prénom | Grade | Etablissement | Qualité |
|----|---------------|-------|---------------|---------|
| 01 | **ELKEURTI Mohamed** | Prof. | Université de Saida – Dr. Moulay Tahar | Président |
| 02 | **DJAAFRI Tayeb** | MCA | Université de Saida – Dr. Moulay Tahar | Rapporteur |
| 03 | **DJAAFRI Abdelkader** | MCB | Université de Saida – Dr. Moulay Tahar | Co-rapporteur |
| 04 | **BENTATA Samir** | Prof. | Université de Mascara | Examinateur |
| 05 | **BELFEDAL Abdelkader** | Prof. | Université de Mascara | Examinateur |
| 06 | **MESKINE Mohamed** | Prof. | Université de Saida – Dr. Moulay Tahar | Examinateur |

بسم الله الرحمن الرحيم

## Dedication

This study is wholeheartedly dedicated to :

"Allah" who gave me strength ,power and led me in the right way for success.

My beloved mother for her loving spirit that substance me well.

My father who made me who I am.

My supervisor: Djaafri Tayeb.

My siblings who shared their words of advice and encouragement to make this study possible.

My respectful husband.

My dear sons : Icherak Sendouce – Miloud Taha- Tasnime zohra .

To the person who was very sympathic with me and I will never forget him :Alkeurti Mohamed - khalfaoui Friha – SADOK CHERIFH Halima

And all who love me.

## *Acknowledgement*

First of all, I would like to express my gratitude to almighty "Allah" for guidance, strength power of mind, protection and enabling me to complete this study.

I convey my sincere gratitude to my supervisor Pr. Djaafri Tayeb without his kind direction and proper guidance this study would have been a little success. In every phase of the project his supervisor and guidance shaped this study be completed perfectly.

I wish to express great thanks to Dr. Djaafri Abdelkader and the jury members Pr. Elkeurti Mohamed, Pr. Bentata Samir, Pr. Belfedal Abdelkader and Pr. Meskine Mohamed who agreed to judge this modest work.

Without forgetting to thank the Physico-chemical studies laboratory members.

Special thanks to all who gave me support help and advice.

Thanks.

**Abstract**:

The investigations of the strain effects on magnetism, elasticity, electronic, optical and thermodynamic properties of PdVTe half-Heusler alloy are carried out using the most accurate methods to electronic band structure, i.e. the full-potential linearized augmented plane wave plus a local orbital (FP-LAPW + lo) approach. The analysis of the band structures and the density of states reveals the Half-metallic behavior with a small indirect band gap $E_g$ of 0.51 eV around the Fermi level for the minority spin channels. The study of magnetic properties led to the predicted value of total magnetic moment $\mu_{tot} = 3\mu_B$, which nicely follows the Slater–Pauling rule $\mu_{tot} = Z_t$ -18. Several optical properties are calculated for the first time and the predicted values are in line with the Penn model. It is shown from the imaginary part of the complex dielectric function that the investigated alloy is optically metallic. The variations of thermodynamic parameters calculated using the quasi-harmonic Debye model, accord well with the results predicted by the Debye theory. Moreover, the dynamical stability of the investigated alloy is computed by means of the phonon dispersion curves, the density of states, and the formation energies. Finally, the analysis of the strain effects reveals that PdVTe alloy preserves its ferromagnetic half metallic behavior, it remains mechanically stable, the ionic nature dominates the atomic bonding, and the thermodynamic and the optical properties keep the same features in a large interval of pressure.

**Résumé :**

L'étude de l'effet de la déformation sur le magnétisme, l'élasticité, et les propriétés électroniques, optiques et thermodynamiques de l'alliage semi-Heusler PdVTe sont effectuées en utilisant la méthode les plus précises basée sur les structure de bande électronique, c'est-à-dire l'onde plane augmentée linéarisée à plein potentiel plus l'orbitale locale (FP-LAPW + lo). L'analyse des structures de bande et de la densité d'états révèle le comportement semi-métallique avec une petite bande interdite indirecte Eg de 0,51 eV autour du niveau de Fermi pour les spins minoritaires. L'étude des propriétés magnétiques a conduit à la valeur prédite du moment magnétique total $\mu_{tot} = 3\mu_B$, qui suit bien la règle de Slater–Pauling $\mu_{tot} = Z_t$ -18. Plusieurs propriétés optiques sont calculées pour la première fois et les valeurs obtenues sont en bon accord avec le modèle de Penn. A partir de la partie imaginaire de la fonction diélectrique complexe on peut constater que l'alliage étudié est optiquement métallique. Les variations des paramètres thermodynamiques calculées s'accordent bien avec les résultats prédits par la théorie de Debye. De plus, la stabilité dynamique de l'alliage étudié est calculée au moyen des courbes de dispersion des phonons, de la densité d'états des phonons et de l'énergies de formation. Enfin, l'analyse des effets de déformation révèle que l'alliage PdVTe conserve son comportement ferromagnétique et semi-métallique, il reste mécaniquement stable, la nature ionique domine la liaison atomique, et les propriétés thermodynamiques et optiques conservent les mêmes caractéristiques dans un grand intervalle de pression.

**الخلاصة:**

تمت دراسة تأثير الإجهاد على الخصائص المغناطيسية والمرونية والالكترونية والضوئية والديناميكية الحرارية لشبه الهاسلر PdVTe باستخدام أكثر الطرق دقة . . أجريت الحسابات على أساس مقاربة الكمون التام للموجات الخطية المتزايدة (FP-LAPW+lo) . من خلال التحليل البنيوي للأشرطة الطاقوية و كثافة المستويات المحسوبة من اجل المركب لوحظ سلوك نصف المعدني مع فجوة صغيرة غير مباشرة بقيمة 0.51 فولت حول مستوى فيرمي لقنوات الدوران الأقلية. أدت دراسة الخصائص المغناطيسية إلى القيمة المتوقعة للعزم المغناطيسي الكلي $\mu_{tot} = 3\mu_B$، والتي تتبع بشكل جيد قاعدة سلاتار و باولي المعطات العلاقة التالية $\mu_{tot} = Z_t -18$ Slater – Pauling. تم حساب العديد من الخصائص البصرية لأول مرة والقيم المتوقعة تتماشى مع نموذج Penn . يتضح من الجزء التخيلي لوظيفة العزل الكهربائي المعقدة أن المادة التي تم فحصها معدنية بصريًا. تتفق تغيرات المعاملات الديناميكية الحرارية المحسوبة بشكل جيد مع النتائج التي تنبأت بها نظرية ديباي. علاوة على ذلك ، يتم حساب الثبات الديناميكي للمادة التي تم فحصها عن طريق منحنيات تشتت الفونون ، وكثافة الحالات ، وطاقات التكوين. أخيرًا ، يكشف تحليل تأثيرات الإجهاد أن PdVTe تحافظ على سلوكها نصف المعدني المغنطيسي ، وتظل مستقرة ميكانيكيًا ، وتهيمن الطبيعة الأيونية على التروابط الذري ، وتحافظ الخصائص الديناميكية الحرارية والخصائص البصرية على نفس الميزات في مجال كبيرة من الضغط.

# Table of content

# Figures

## Tables

# Part I

# General Introduction

# 1. General introduction

Ferromagnetic Heusler alloys exhibited magnetic shape memory effect, magnetic field induced superelasticity and large strain-induced changes in the magnetization are recently very attractive subject of current researches.[1–14] The ferromagnetic martensites are experimentally found in different Heusler alloys such as Ni–Mn–Ga, Ni–Fe–Ga, Co–Ni–Ga and other alloys. The magnetic shape memory effect is related to martensite transformations that are sensitive to pronounced magnetoelastic interaction. A high efficiency of the magneto-mechanical properties makes these materials very attractive for applications as different kind of actuators, sensors, magnetic micro-electro-mechanical systems, for the recording and storage of information, etc. The current advantages in new materials are promising for engineering of new spintronic devices. In this context the problem of local magnetic properties can be one of the most important in the physics of these materials.

It is known that magnetic properties of Heusler alloys are strongly dependent on both the conduction electron concentration and chemical bonding. For example Mn-based compounds demonstrate rather localized magnetism due to configuration of Mn d-orbitals [9,13,14] whereas Co-based compounds show more itinerant behavior.[15] So-called full-Heusler alloys with a general formula unit of $X_2YZ$, here X and Y denote the transition metals and Z is s-p element such as Al, Ga, Sn, Sb, etc., are studied also with respect to the transition from the ferromagnetic phase to an antiferromagntic one with changing of the concentration of the carriers. Half-metallic Heusler ferromagnets (XYZ) have an energy gap for minority spin bands and the conduction electrons at the Fermi level ($E_F$) show 100% spin polarization and can be used as spin-polarized electron sources along with metal oxides and III–V group semiconductors. It is known that the full-Heusler alloys such as $Co_2MnZ$ with Z is Si, Ge demonstrate half-metallic behavior also.

The magnetic properties of the Heusler alloys are very sensitive to the local geometry and chemical composition. In order to understand the dependence of magnetic properties on the atomic composition and crystal structure the ab-initio investigation of the electronic structure can be very useful.

The Ni2MnGa remains most investigated Heusler alloy by both experimental and theoretical approaches. It is known from the literature that the physical properties of this alloy very sensitive to structural disorder and deviations from stoichiometric composition. At present exist several band structure calculations of Ni2MnGa which were performed using different ab-initio techniques, in particular augmented sphericalwave method [9] full-potential linearized augmented-plane-wave method [12,15] pseudo potential plane-wave approach [16] etc. Less attention was paid to other alloys but a number of the theoretical investigations of the full-Heusler alloys are sharply increased.[17] The similar tendency is observed for half-metallic Heusler alloys.[18,19] The calculations were mainly performed using the local spin density approximation (LSDA), which are known to be underestimated lattice constants and provide smaller magnetic moments.

In present thesis we will deal with the general properties of the full and the half-Heusler alloys, from a theoretical and experimental point of view. A review of what has been already published will be presented.

Before starting our discussion about these systems, it is appropriate to point out the differences between full-Heusler and half-Heusler and explain shortly their properties, in order to approach the argument in a systematic way. In order to show the importance of these materials we mentioned in this part briefly their different fields of application.

Main part is consecrated to the investigations of the strain effects on magnetism, elasticity, electronic, optical and thermodynamic properties of PdVTe half-Heusler alloy are carried out using the most accurate methods to electronic band structure, i.e. the full-potential linearized augmented plane wave plus a local orbital (FP-LAPW + lo) approach. The analysis of the band structures and the density of states reveals the Half-metallic behavior with a small indirect band gap Eg of 0.51 eV around the Fermi level for the minority spin channels. The study of magnetic properties led to the predicted value of total magnetic moment µtot = 3µB, which nicely follows the Slater–Pauling rule µtot = Zt -18. Several optical properties are calculated for the first time and the predicted values are in line with the Penn model. It is shown from the imaginary part of the complex dielectric function that the investigated alloy is optically metallic. The variations of thermodynamic parameters calculated using the quasi-harmonic Debye model, accord well with the results predicted by the Debye theory. Moreover, the dynamical stability of the investigated alloy is computed by means of the phonon dispersion curves, the density of states, and the formation energies. Finally, the analysis of the strain effects reveals that PdVTe alloy preserves its ferromagnetic half metallic behavior, it remains mechanically stable, the ionic nature dominates the atomic bonding, and the thermodynamic and the optical properties keep the same features in a large interval of pressure.

Finally, in the last part, we summarized the main results and we shall conclude that this work opens interesting perspectives, including the study of a several properties in order to use this type of materials in the technological applications.

# References

[1] Heusler F, Verh. Dtsch. Phys. Ges. **5**, (1903) 219

[2] R. A. de Groot, F. M. Mueller, P. G. van Engen and K. H. J. Buschow Appl. Phys. **55**, (1984) 2151

[3] I. Galanaki and P. H. Dederich,J. Phys.: Condens. Matter **676,** (2005) 1

[4] K. Endo, T. Phayama and R. Kitamura, J. Phys. Soc. Jpn. **19,** (1964) 1494

[5] J. Kubler, Physica B **127,** (1984) 257

[6] R. Dunlap, G. Stroink and K. Dini, J. Phys. F: Met. Phys. **16,** (1986) 1083

[7] W. Zukovski, A. Andrejezuk, L. Dobrzyeski, M. J. Cooper, M. A. G. Dixon, S. Gardelis, P. K. Lawson, T. Buslaps, S. Kaprzyk, K. U. Neumann and K. R. Ziebeck, J. Phys.: Condens. Matter **9**, (1997) 10993

[8] J. Worgull, E. Petti and J. Trivisonno, Phys. Rev. B **54**, (1996) 15695

[9] S. Plogmann, T. Schlatholter, J. Braun and M. Neumann, Phys. Rev. B **60,** (1999) 6428

[10] S, Ishada, J, Ishada, S. Asano and J. Yamashita, J. Phys. Soc. Jpn. **45**, (1978) 1239

[11] J. Kubler, A. R. Williams and C. B. Sommers, Phys. Rev. B **28**, (1983)1745

[12] S. Fujii, S. Ishida and S. Asano, J. Phys. Soc. Jpn. **58**, (1989) 3657

[13] P. J. Webster and K. R. A. Ziebeck, J. Phys. Chem. Solids **34,** (1973) 1647

[14] A. A. Aquela, J. Enkovaara, K. Uliakko and R. E. Nieminen, J. Phys.: Condens. Matter **11,** (1999) 2017

[15] V. A. Chernenko, V. A. L'vov, R. Mullner, G. Kostorz and T. Takagi, Phys. Rev. B **69,** (2004) 134410

[16] S. E. Kulkova, S. V. Eremeev, T. Kakeshita, S. S. Kulkov and G. E. Rudenski, Mater. Trans. **47**, (2006) 599

[17] R. A. de Groot, A. M. van der Kraan and K. H. J. Buschow, J. Magn. Magn. Mater. **61,** (1986) 330

[18] A. Bouhemadou, R. Khenata and B. Amrani, Physica B **404,** (2009) 3534

[19] M. J. Otto, R. A. M. van Woerden, P. J. van der Valk, J. Wijngaard, C. F. van Bruggen, C. Haas and K. H. J. Buschow, J. Phys.: Condens. Matter **1,** (1989)2341

# Part II

## Full and half-Heusler Alloys

# 2 Full and half-Heusler alloys

## 2.1 Areas of technological application

Since the discovery of giant magnetoresistance (GMR) spintronics has become a field of intense commercial and research interest. A magnetoresistive sensor can be found in the read head of every hard disk drive sold every year. The field of spintronics continues to grow with renewed interest and vigour as second generation magnetic random access memory (MRAM) becomes commercially viable. All spintronic devices need a source of spins. This is usually in the form of a ferromagnet. However, these typical transition metal ferromagnets have low spin polarisation or low spin injection efficiency, typically less than 50%. Half-metallic ferromagnets are a leading candidate to replace current materials and offer much greater spin polarisation, possibly up to 100%. However there are a number of key issues that must be overcome before these films can be used in commercial devices.

### 2.1.1 Spintronics

Today the integrated circuit and semiconductors are the backbone of modern technology. Complementary metal-oxide-semiconductor (CMOS) and metal-oxide-semiconductor field effect transistor (MOSFET) technologies form the building blocks of this backbone [1]. In recent years there have been a number of astonishing advances in this technology, driven by advances in the scalability of these devices. The drive towards the current state of technology is due to Moore's law [2] which states that the number of transistors on a single chip doubles every 18 months. This has held true for over 30 years to the point where today's most advanced home computer components have 7.1bn transistors per chip [3].

However, this trend cannot continue. We are approaching the physical limit where these devices can function, either due to high leakage currents [4] or simply the limitations of lithography to pattern them. This technological advancement is mirrored in the magnetic storage industry where the same trend is seen for areal density, information stored per unit area. However this is beginning to plateau due to material limitations in both the hard disk and the read head sensor. New technologies are required to overcome these difficulties and continue the technological advance.

Spin-electronics is a promising candidate to allow further development of current semiconductor technologies as it is widely used in the hard disk industry for read head sensors. This means that the processes for commercialising spintronics are already in-place. To improve spintronic devices beyond their current limitations new materials and device technologies must be implemented. Spintronics is a field comprising many sub disciplines although these can be broadly divided up into semiconductor spintronics [5] and magnetoelectronics [6,7]. The latter is concerned with all metallic systems such as magnetoresistive devices.
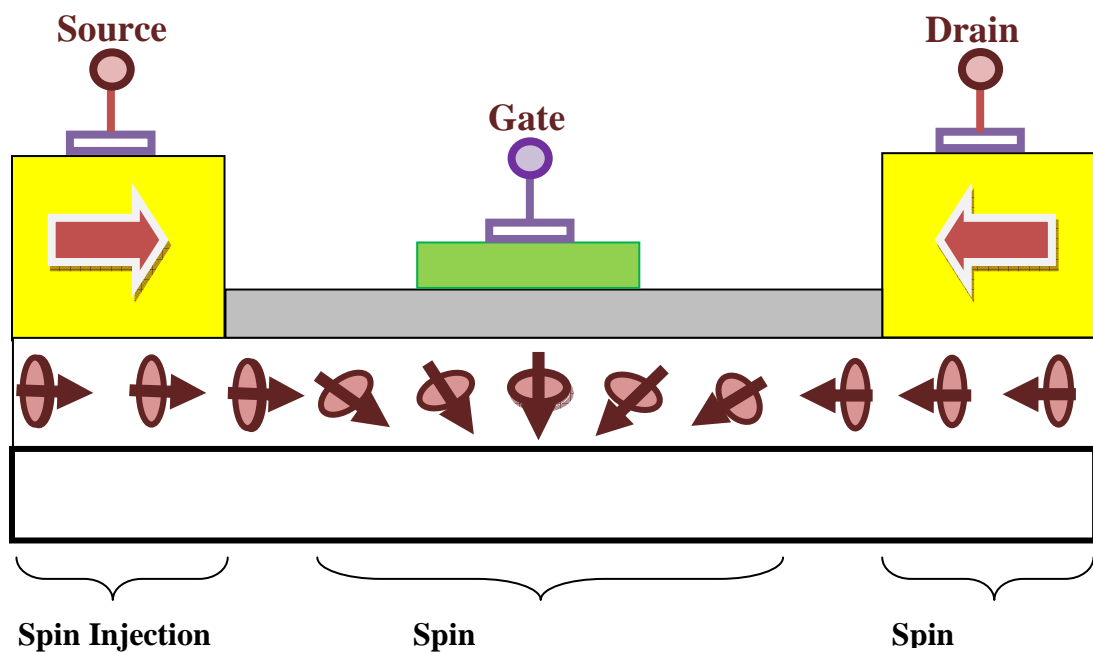


**Fig. 2.1:** Schematic diagram of Datta-Das Spin FET. **[8]**

Spintronics is based around the concept of using quantised angular momentum, spin, of an electron instead of or as well as its charge. Although the effects of the spin of the electron had been observed experimentally in the late 19th century it was not defined until the early 20th century by *Dirac*. In 1857 *Lord Kelvin* (formally W. Thomson) observed anisotropic magnetoresistance (AMR) [9]. AMR is the directional dependence of the resistivity of a material relative to a magnetic field. AMR is one of many forms of magnetoresistance which shall be discussed more thoroughly in the next section. Since these early observations of spin dependent electron transport many different devices have been designed and fabricated all using slightly different spin dependent phenomena. The most basic and best example of the requirements of a spintronic device is the spin field effect transistor (SpinFET) as designed by *Datta* and *Das* [8], shown in Figure 1.1.

This work is primarily concerned with the spin source where a high spin polarisation is required. The simplest spin source is a typical ferromagnet interfaced with non-magnetic metal or semiconductor. The Heusler alloys used in this work are intended for use in such a spin source. However spin generation has also been achieved through the manipulation of magnetisation dynamics, resulting in a phenomenon known as spin pumping [10].

### 2.1.2 Magnetoresistance

Although AMR was discovered in 1857 it was mainly of academic importance due to it only having a small effect (a few per cent). It was used for a number of early hard disk designs until superseded by the discovery of other magnetoresistive effects such as giant magnetoresistance (GMR).

GMR was discovered in 1988 through electrical magnetotransport measurements of ferromagnetic/non-magnetic/ferromagnetic multi-layered systems. This was an attempt to further understand the dependence of interlayer exchange coupling on the spacer thickness in thin film multilayers [11].

Grünberg [12] and *Fert* [13] discovered the effect simultaneously while measuring Fe/Cr/Fe superlattices spaced sufficiently to induce antiferromagnetic coupling between the two Fe layers. The pair received the Nobel prize in Physics for their discovery in 2007. In their initial publications both observed a large change in resistance for the structures when the spaced magnetic layers were changed from anti-parallel to parallel alignment.

This was explained using the two current model initially proposed by *Mott* in 1936 [14,15]. Simply that the current through a transition metal can be separated into two spin channels. This model has since been extended by *Campbell* [16] and *Fert* [17] to include a large number of different electron scattering terms that provide better agreement with the experimental data. This effect in a GMR multilayer is often best explained pictorially as shown in Figure 1.2.
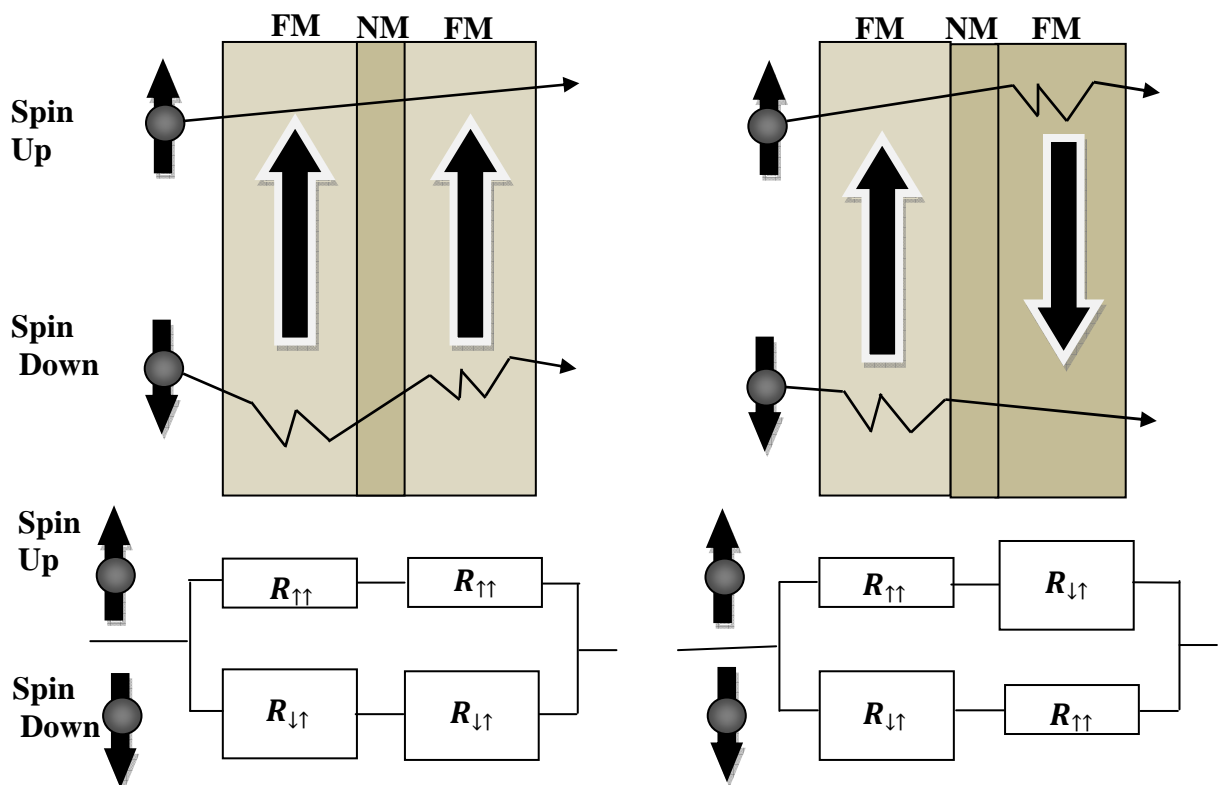


**FiG. 2.2 :** Schematic of the GMR effect [18].

For the parallel aligned case, one spin channel experiences small or no spin scattering through both ferromagnetic layers. This leads to a low resistance state. In the anti-parallel aligned case, both spin channels experience spin scattering in one of the ferromagnetic layers leading to a high resistance state. Initially this effect was small (1.5% at room temperature) [12]. Since its discovery, large developments have seen the magnitude of the GMR effect increase to 34% at room temperature [19]. There have also been demonstrations of the effect in two different orientations, known as current-in-plane (CIP) and current-perpendicular-to-plane (CPP) [18]. These two orientations have a number of different properties, however CPP-GMR is the current focus of much research interest due to its applicability to current generation MRAM.

If the non-magnetic spacer is replaced by a non-metallic spacer then another phenomenon known as tunnelling magnetoresistance (TMR) can occur. This was first observed by *Julliere* in 1975 [20] with a resistance change of 14% between parallel and anti-parallel states at 4.2K. It was not until the early 1990s that this effect was observed at room temperature, initially by *Miyazaki* (18%) [21] and then by *Moodera* (11.8%) [22]. These experiments used amorphous insulating spacers such as AlOx however, since the pioneering theoretical work of *Butler* in 2001 [23], there has been much greater interest in using crystalline MgO barriers. These were predicted to allow TMR ratios of over 1000%. Experimentally, values of 600% at room temperature have been achieved by *Ikeda et al.* using CoFeB/MgO/CoFeB multilayer films [24]. Although similar in many ways to GMR, TMR is fundamentally quite different.

TMR depends on the conduction states available to tunnel into across the barrier, not just the spin dependent scattering within the electrodes. This is shown schematically in figure 1.3. For the parallel orientation there are a large number of majority conduction states and majority valance states resulting in a large electron flow and thus low resistance. For the anti-parallel orientation there are fewer majority and minority states resulting in a high resistance.

This makes TMR dependent upon the number of available states for each spin direction at the Fermi energy or the spin polarisation, equation 1.1.

$$TMP = \frac{\Delta R}{R} = \frac{2P_1 P_2}{1 - P_1 P_2}$$ (1.1)

where $P_1$ and $P_2$ are the spin polarisations of ferromagnetic layers in the junction. This means that for the most of the Heusler alloys the achievable TMR should be extremely high due to large values of spin polarisation from these materials.
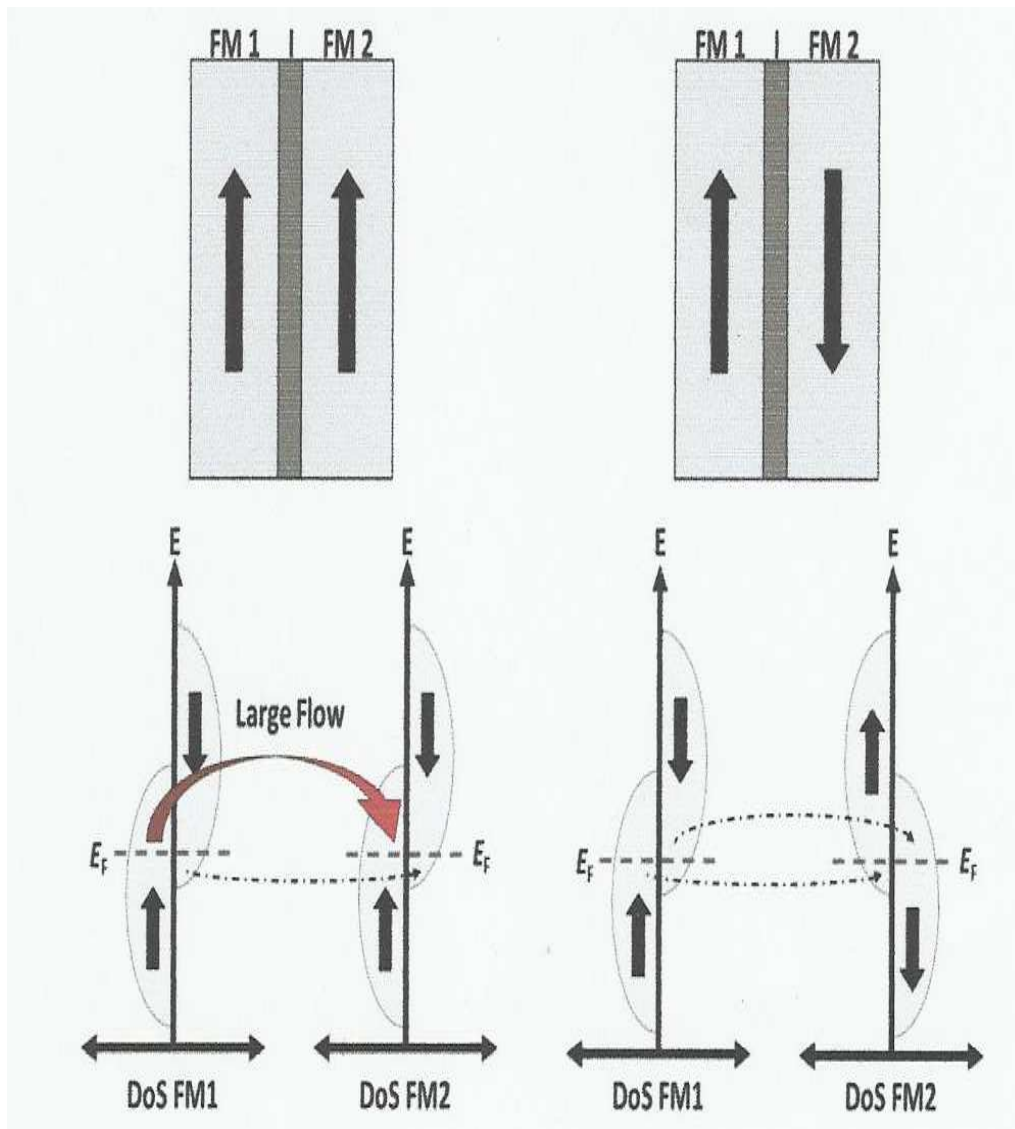


**Fig. 2.3 : Schematic of the TMR effect.**

### 2.1.3 Spin Transfer Torques

The most promising new spintronic technology is MRAM. This will potentially replace current semiconductor based dynamic random access memory (DRAM). MRAM has a large number of advantages, most importantly it is non-volatile. This means that when the power is turned off the information is retained. 1st generation MRAM used the Oersted field generated by a current carrying wire to write information to an array of magnetic spin valves. The 2nd generation of MRAM will use a phenomenon known as spin-transfer-torque (STT) as a much more efficient way to write data.

STT was first considered as a way to reverse the magnetisation in a magnetic multilayer by *Slonczewski* [25]. However the effect of spin transfer had been introduced by *Berger* 12 years earlier [26]. STT is easiest to consider in the case of a ferromagnetic/non-magnetic/ferromagnetic junction like those used for GMR. The two ferromagnetic layers have their magnetisations aligned at an angle to one another. When electrons flow into the junction they are initially aligned or polarised to the direction of the magnetisation in the first ferromagnetic layer. When the electrons then travel to the second ferromagnetic layer their spins align with the magnetisation of that layer. However as the spins align to the new direction of magnetisation they exert a torque on that magnetisation. This is the spin transfer torque. Figure 1.4 shows this effect schematically.

If a sufficient number of electrons are injected into the second ferromagnetic layer the torque can be large enough to overcome the torque due to the magnetisation of the material and as a result align the magnetisation of the second ferromagnetic layer $M_2$ with that of the first $M_1$. It is also possible to reverse the direction of $M_2$ back to its original state by injecting the electrons in the opposite direction. In this situation the spins align with $M_2$ and are then injected into $M_1$. However, those spins aligned antiparallel to $M_1$ are reflected back at the interface and injected back into the second ferromagnetic layer where they once again exert a torque on $M_2$.

Thus the magnetisation in one ferromagnetic layer can be switched by changing the polarity of the applied voltage. The form of the spin transfer torque is given by equation 1.2 [10]:

$$\tau_{STT} = M_1 \times (M_1 \times M_2) P \frac{\gamma_{gm}}{M_s V e} I \tag{1.2}$$

Here the cross products of the magnetisations $M_1$ and $M_2$ give the direction of the torque. The magnitude of the torque is then dictated by the spin polarisation of the ferromagnets $P$, the saturation magnetisation $M_s$, the volume of the magnetic layer on which the torque is acting $V$ and the current applied to the junction $I$. $\gamma_{gm}$ is the gyromagnetic ratio. The dependence of STT on the spin polarisation of the electrodes makes Heusler alloys a promising candidate for use in these devices due to their high spin polarisation. A detailed examination of spin transfer torques in a large number of systems can be found in *Maekawa* [27].
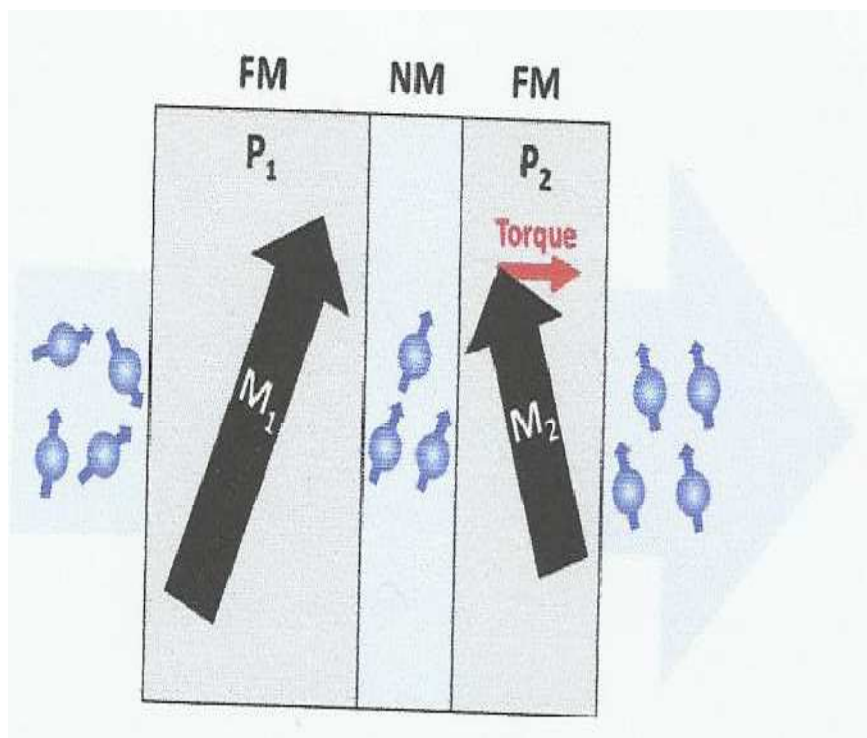


**Fig.2.4 :** Schematic diagram of the spin transfer torque effect on magnetisation in a FM/NM/FM junction.

## 2.1.4 Half Metallic Ferromagnets

Half metallic ferromagnets (HMF) are a possible route to highly spin polarised materials. This class of materials was initially proposed by *de Groot et al.* [28] in the early 1980s. In conventional ferromagnets, the spin polarisation arises from an imbalance in the density of states for up (majority) and down (minority) spin electrons. In HMFs the conduction properties for the minority channel are completely different to that of the majority spin channel. The majority band has filled electron states up to the Fermi energy giving metallic conduction while the minority states have a band gap resembling a semiconductor. This is shown schematically in Figure 2.5.

Since the original studies of half-metallic ferromagnetism on NiMnSb [28] a large number of compounds have been found to be half metallic. Many of these are complex alloys, predominantly Heusler alloys [29-31] although half-metallic ferromagnetism has been shown in $CrO_2$ [32] and even predicted in graphene [33]. Because of these unusual conduction properties HMFs could potentially provide a material with 100% spin polarisation. This would provide extremely high values of TMR and GMR (TMR 832% [34] and GMR of 80% [19]) as well as large spin transfer torques for future spintronic devices. A more detailed discussion of the origin of this half metallicity in Mn-based Heusler alloys can be found in chapter 4.
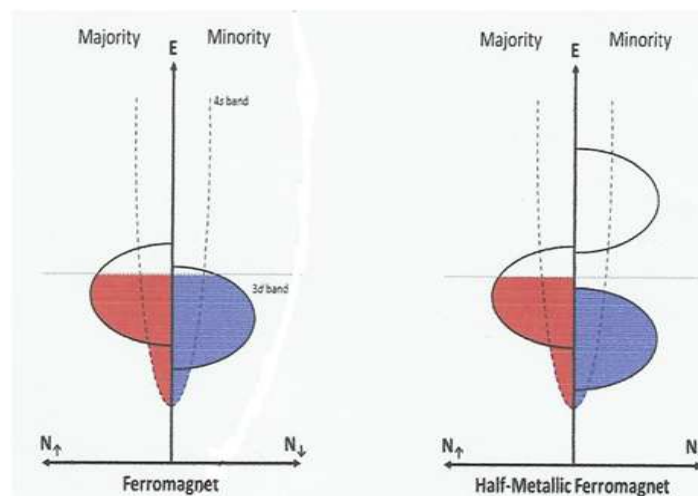


**Fig. 2.5:** Schematic diagrams of the band structures for a ferromagnet and a half metallic ferromagnet.

## 2.1.5 Heusler Alloys in Magnetoresistive Devices

Since the discovery of half metallic ferromagnetism in a number of Heusler alloys they have been a field of great research interest for spintronic devices. Co-based Heusler alloys are of particular interest due to their high magnetic moment and Curie temperature, as well as their predicted 100% spin polarisation. Alloys of $Co_2$(Mn1-xFex)Si [35], $Co_2$Fe(Al1-x,Six)[34] and $Co_2$MnGe [36] have found application in many different devices.

The properties of Heusler alloy devices are extremely dependent upon their structure. This includes the Heusler film itself as well as any effects from those films around it. As such, many different structures and growth methods have been used to optimise these properties. Initially, $Co_2$FeSi films deposited on V buffered Si substrates resulted in reasonable values of TMR of up to 52% at 16K (28% at room temperature) [37]. However this has been improved using $Co_2$FeSi/$Co_2$MnSi multi-layered electrodes [37]. Improved values from single layer $Co_2$FeSi electrodes have been achieved using MgO substrates and crystalline MgO tunnel barriers (TMR = 42% at RT) [38]. The real improvements to these values have occurred since the optimisation of the alloy composition to $Co_2$FeAl$_{0.5}$Si$_{0.5}$.

$Co_2$FeAl$_{0.5}$Si$_{0.5}$ is optimised so that the Fermi energy lies in the middle of the minority band gap resulting in much improved spin polarisation (90%) [39,40]. Optimisation of both the alloy and the deposition conditions has led to the highest reported value of TMR in a Heusler alloy system, 832% at 9K and 386% at 300K [34].

GMR structures have also been created using Co2FeAl0.5Si0.5 electrodes with both Ag [41,42] and Cr [43] spacers. Extremely high values of GMR, 80% at 14K (34% at room temperature), have been achieved in these systems [41]. Magnetisation switching through spin transfer torque has also been observed in these structures with critical current densities for switching as low as 106 A/cm2 [42]. However, all these devices have a number of flaws for commercial applications.

The main problems are the high temperatures required to crystallise the Heusler alloy electrodes as well as the UHV deposition conditions. Recently, polycrystalline films have been used in device structures resulting in GMR values of up to 10% at room temperature. These films have significant advantages of reduced fabrication temperatures as well as much lower resistance values (30mΩμm2) [44].

## 2.2 Theoretical and experimental background

In this chapter we will deal with the general properties of the full and the half-Heusler alloys, from a theoretical and experimental point of view. A review of what has been already published will be presented. Before starting our discussion about these systems, it is appropriate to point out the differences between semimetals and half-metals and explain shortly their properties, in order to approach the argument in a systematic way.

### 2.2.1 Semimetals and half-metals

A semimetal is defined as a material which presents a small overlap in the energy of the conduction band and valence bands. One band is almost filled whereas the other band is nearly empty at zero temperature. Each atom is positioned closer to three of its neighbor atoms than to the rest. As an example, the structure of antimony and arsenic is composed of spheres that intersect along at circular areas. The covalent character of the bonds joining the four closest atoms is linked to the electronegative nature of the semimetals, reflected by their position in the periodic table. They lie between metals and non metals. Members of this group are fairly brittle, and do not conduct heat and current as well as the native metals. The bond type suggested by these properties is intermediate between metallic and covalent; it is consequently stronger and more directional than pure metallic bonding, resulting in crystals of lower symmetry. The classic semimetallic elements are arsenic, antimony and bismuth.

These are also considered metalloids but the concepts are not synonymous. Semimetals, in contrast to metalloids, can also build compounds such as HgTe; tin and graphite are typically not considered metalloids. The electronegativities and ionization energies of the metalloids are between those of the metals and nonmetals, so the metalloids exhibit characteristics of both classes. Silicon, for example, possesses a metallic luster, though it is an inefficient conductor and is brittle. The reactivity of the semimetals depends on the element with which they react. For example, boron acts as a nonmetal when reacting with sodium and as a metal when reacting with fluorine. The boiling points, melting points, and densities of the semimetals vary widely. The intermediate conductivity of semimetals means that they tend to make good semiconductors.

A half-metal is defined as a ferromagnetic metal showing a band gap at the Fermi energy for one spin direction. Consequently, only charge carriers of one spin direction contribute to the conduction. Since the band gap is the essential ingredient in half-metals, it is important to consider its origin. Dozens of half-metals are known by now.

Three categories can be distinguished on the basis of the nature of the band gap: (1) half-metals with covalent band gaps; (2) Charge transfer band gaps, and (3) d - d band gaps. This distinction is important because the origin of the half-metallicity is different in each category. Hence the influence of external perturbations (e.g., pressure) is different as well as the sensitivity to disorder, behavior at surfaces and interfaces, etc. A description of the three different categories follows below.

### 2.2.1.1 Covalent band gaps

The origin of the band gap in these materials is strongly related with the well known semiconductors of group III-V type, like GaAs. A well known example is NiMnSb. It crystallizes in the half-Heusler structure "$C1_b$", which is closely related with the zincblend structure: one of the empty positions is occupied by the third constituent, Ni in this case, and both Mn and Sb have to occupy sites with tetrahedral

coordination. The presence of occupied d minority states is essential in these materials: half-metals of this category are weak magnets.

### 2.2.1.2   Charge-transfer band gaps

This category is found in strongly magnetic compounds, where the d bands of the transition metals are empty for the minority spin direction and the itinerant s,p electrons of the transition metals have been localized on the anions. Examples of half-metals in this category are $CrO_2$, the colossal magnetoresistance (CMR) materials and double perovskites such as $La_{0.7}Sr_{0.3}MnO_3$. The presence of band gaps in these materials is not very dependent on the crystal structure. Compounds in this category are strong magnets.

### 2.2.1.3   d-d band gap

Half metals in this category show rather narrow bands, so that gaps occur between crystal- field split bands. The exchange splitting can be such that the Fermi level is positioned in a gap for one spin direction only. These materials are weak magnets by definition. Examples in this category are $Fe_3O_4$, $Fe_xCo_{1-x}S_2$ and $Mn_2VAl$.

As a comparison, in figure 2.1 we show the band structures of three half metals, each of them belonging to one of the different categories described above. The images were taken from refs [45], [46], respectively. In figure 2.1.a the band structure for NiMnSb is shown. This system crystallizes in the structure $C1_b$. As we will see later on, also another Heusler structure exists (called $L2_1$), where the fourth position is filled. If this is the case, compounds like $Ni_2MnSb$, which is a normal ferromagnet, can result. According to what has been studied by Weht et al. [45], the half metallic properties of NiMnSb should be attributed to the lower density with respect to $Ni_2MnSb$.

In figure 2.1.b the structure of $CrO_2$ is presented. As already stated, this system is a strong ferromagnet and shows for the minority channel a clear gap between the empty and nonempty states at the Fermi level. $CrO_2$ crystallizes in the rutile structure. This structure allows for stoichiometric (001) surface, which is unlikely to reconstruct or to show surface segregation. Calculations show two oxygen-derived surface states in the band gap for the minority spin direction, but these states are located well below the Fermi energy and do not corrupt the half-metallic properties at the surface.

Experimentally $CrO_2$ shows the highest degree of spin polarization of all materials studied by Andreev reection. As a third example we show the band structure calculations for $Mn_2VAl$ [46]. We notice that the majority and minority bands, within 1 eV of the Fermi level are very different.
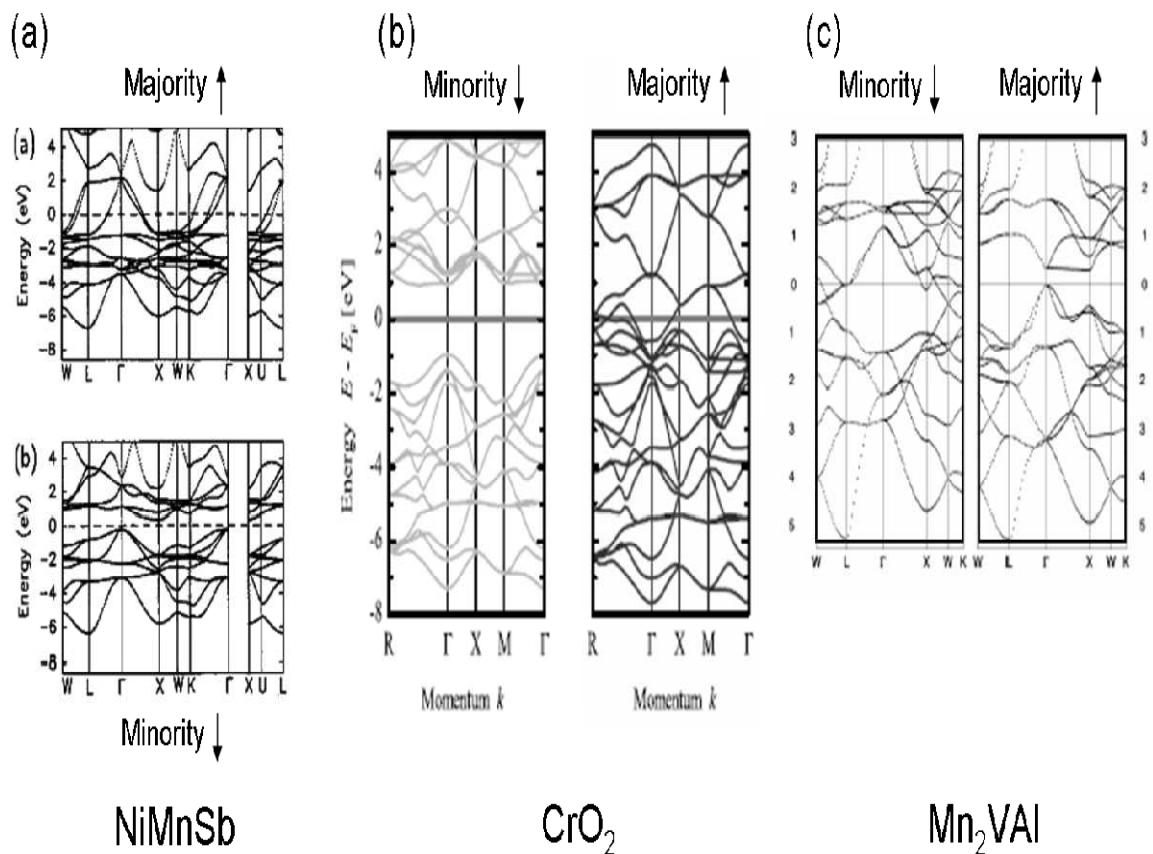


**FiG. 2.6 :** Band structures of (a) NiMnSb, (b) $CrO_2$, (c) $Mn_2VAl$.

In figure 2.2 we observe the different materials which are commonly classified as half-metals. They can assume different structures known as rutile, zincblend, spinel, perovskite and Heusler. We will focus our attention on the Heusler alloys, since most of this thesis work has been devoted to them.
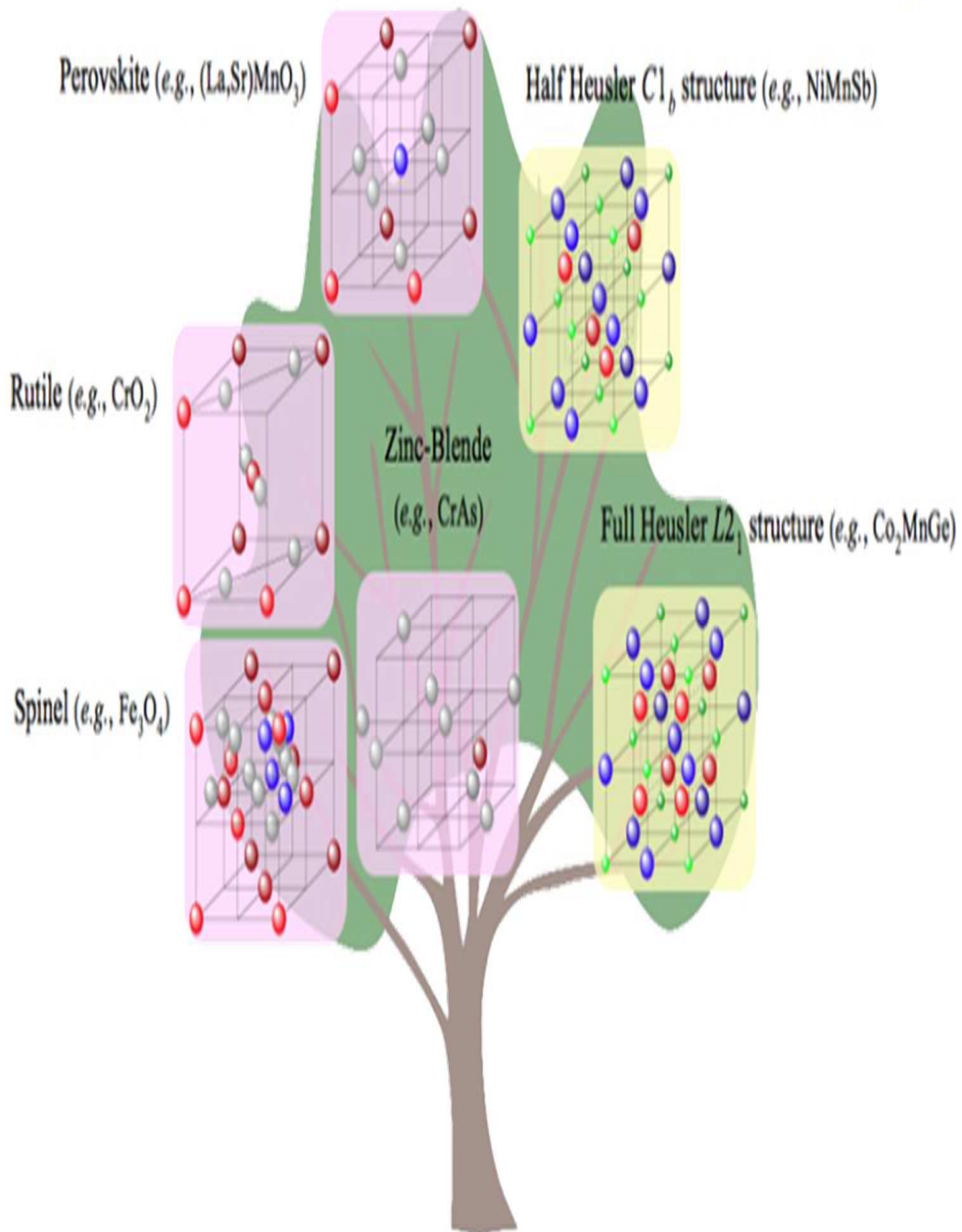


**Fig. 2.7:** The tree of half metallic ferromagnets.

## 2.3 Stuctural properties of full and half-Heusler alloys

The discovery of Heusler alloys dates back to 1903 when A. Heusler reported that the addition of sp elements (Al, In, Sn, Sb or Bi) in a Cu-Mn alloy turn it into a ferromagnetic material, even though no ferromagnetic element was contained [47]. The basic understanding of crystal structure and composition of these alloys remained unknown for a long time. In 1929 X-ray measurements of Potter [48] on a Cu-Mn-Al alloy revealed that all constituents of this system were ordered in a fcc lattice. Bradley and Rodgers [49] investigated the Cu-Mn-Al system in detail using X-ray and anomalous X-ray scattering.

They established a relationship between composition, chemical order and magnetic properties. After a successful interpretation of the crystal structure numerous investigations were made on these systems. It was found that the Heusler structure is formed essentially from the ordered combination of two binary B2 compounds XY and XZ. Both compounds may have the CsCl type crystal structure, for instance CoMn and CoAl yield $Co_2MnAl$. Thus the ability of compounds to form B2 structure indicates the possibility of forming new Heusler compounds. It was also discovered that it is possible to leave one of the four sublattices unoccupied ($C1_b$ structure). The latter compounds are often called half- or semi-Heusler alloys, while the $L2_1$ compounds, where all four sublattices are occupied are referred to as full-Heusler alloys. Extensive experimental studies showed that the majority of Heusler compounds order ferromagnetically in stoichiometric composition. Crystal structure, composition and heat treatment were found to be important parameters for determining magnetic properties.
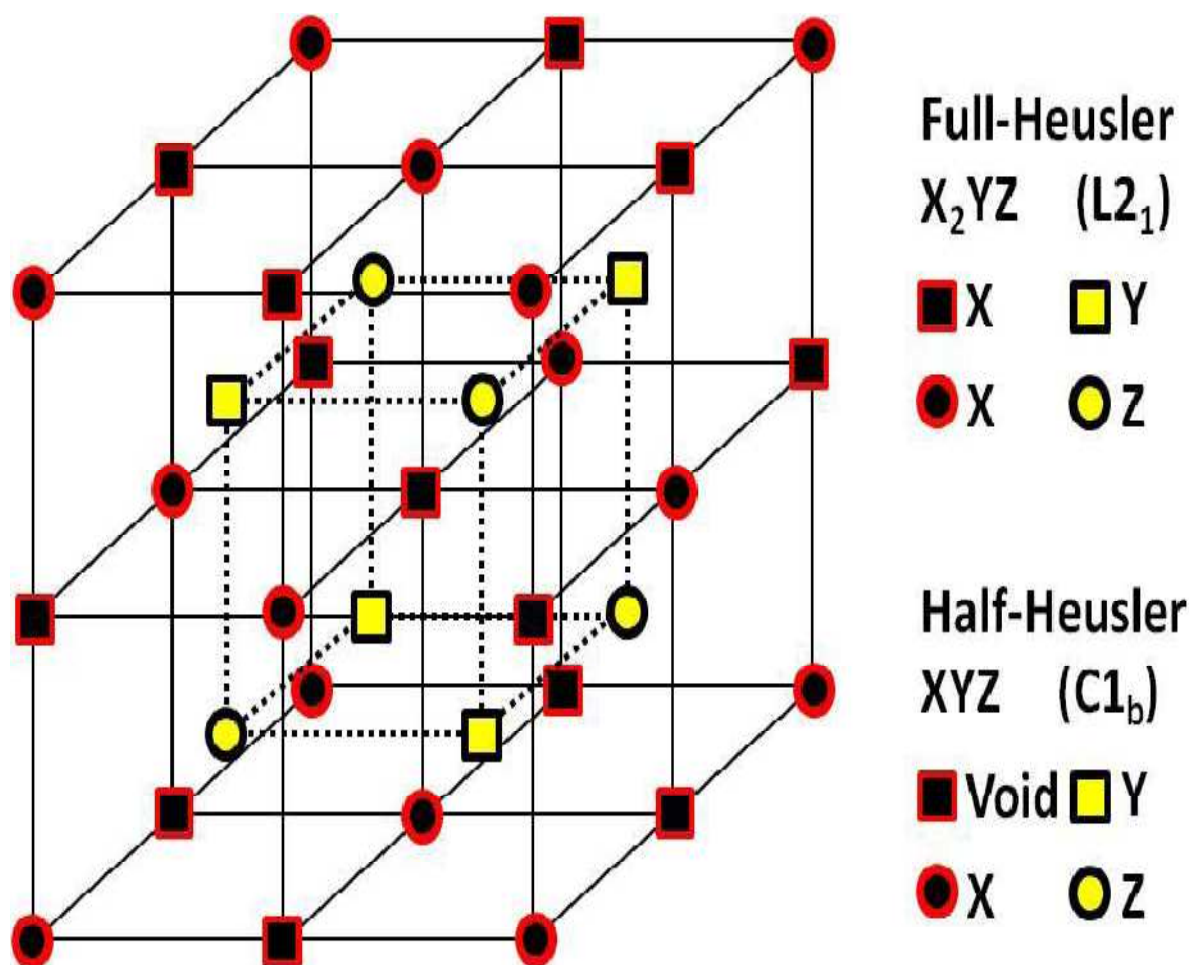
**Fig. 2.8 :** Structure of full and half-Heusler

With the discovery of half-metallic ferromagnetism in NiMnSb and the observation of shape memory effect in $Ni_2MnGa$ compound, Heusler alloys received tremendous experimental and theoretical interest. In the following we will briefly present the previous experimental and theoretical studies on structural and magnetic properties of Heusler alloys. Also, an overview of the experimental and theoretical studies in literature will be given.
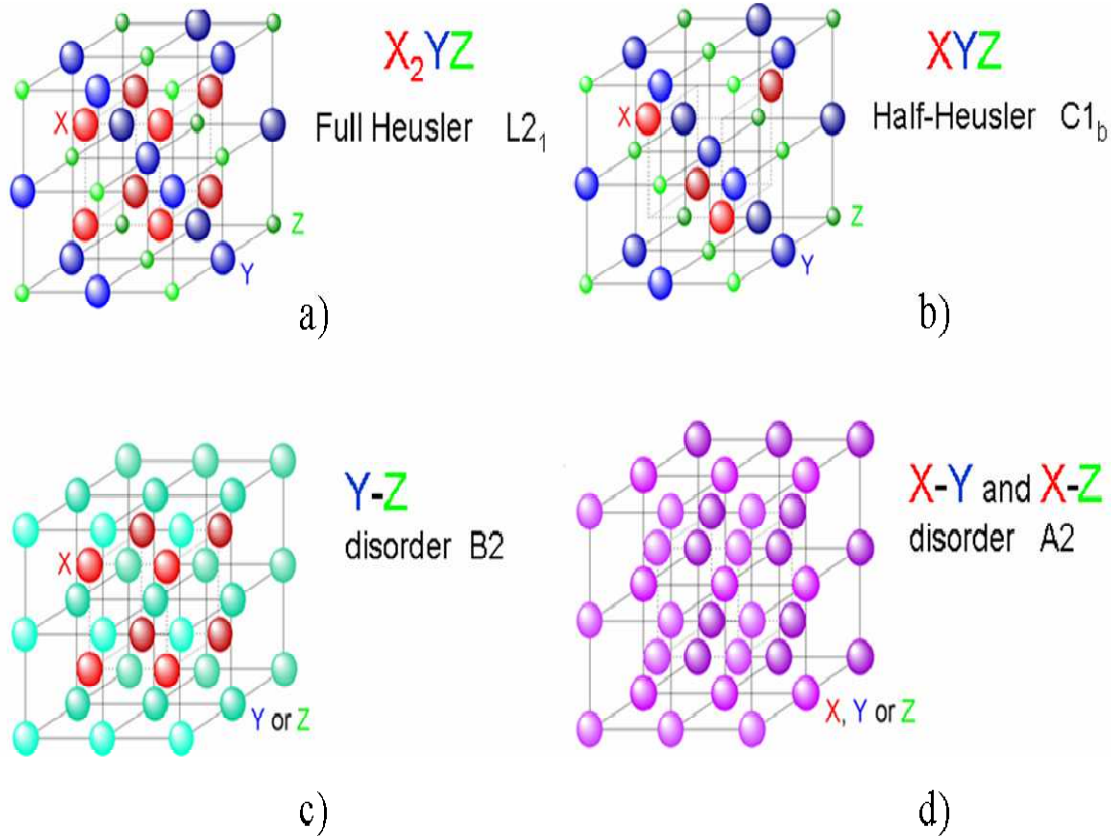
**Fig. 2.9 :** (a) L2$_1$ full-Heusler and (b) C1$_b$ half-Heusler ordered structures. The structure consists of 4 interpenetrating fcc lattices. In the case of the half-Heusler alloys one of the four sublattices is empty. One notices that if all atoms are identical, the lattice is simply bcc.

Heusler alloys are ternary intermetallic compounds. At the stoichiometric composition, the full Heusler alloys X$_2$Y Z and the half-Heusler XYZ crystallize in the L2$_1$ and C1$_b$ structures, respectively. The elements associated with X and Y are transition metal elements; the atom which sits in position Z is non-magnetic. The unit cell consists of four interpenetrating fcc sublattices with the positions (000) and ($\frac{1}{2},\frac{1}{2},\frac{1}{2}$) for X, ($\frac{1}{4},\frac{1}{4},\frac{1}{4}$) for Y and ($\frac{3}{4},\frac{3}{4},\frac{3}{4}$) for Z atom. The site ($\frac{1}{2},\frac{1}{2},\frac{1}{2}$) is empty in half-Heusler compounds as shown in the figures 2.8 and 2.9. The two structures are closely related with vacant site.

The $C1_b$ structure can be obtained from the $L2_1$ one by replacing the half of the X sites in an ordered manner. In most of the Heusler alloys Mn enters as the Y element. The compounds where Mn occupies the X positions are very rare: $Mn_2VAl$ [50] and $Mn_2VGa$ [51, 46] are two examples.

## 2.4 Magnetic properties of Heusler alloys

Heusler alloys are very interesting materials which possess attractive magnetic properties. One can study in the same family of alloys a series of interesting diverse magnetic phenomena like itinerant and localized magnetism, antiferromagnetism, helimagnetism, Pauli paramagnetism or heavy-fermionic behavior [52], [53], [54], [55].

### 2.4.1 Ferromagnets

The majority of the full and the half-Heusler alloys order ferromagnetically and saturate in weak applied magnetic fields. If the magnetic moment is carried by Mn atoms, as it often happens in the alloys $X_2MnZ$, a value close to 4μB is usually observed. Although they are metals, these compounds have localized magnetic properties and are ideal model systems for studying the effects of both atomic disorder and changes in the electron concentration on magnetic properties. In order to reveal the role played by the 3d (X) and sp (Z) atoms on the magnetic properties of Heusler alloys, extensive magnetic measurements have been performed on quaternary Heusler alloys [57]. It has been shown that sp electron concentration has a primary importance in establishing magnetic properties, inuencing both the magnetic moment formation and the type of the magnetic order.

### 2.4.2 Antiferromagnets and ferrimagnets

Although the majority of Heusler alloys are ferromagnetic, some of them order antiferromagnetically, in particular those compounds containing 3d element in which the magnetic moment is only carried by Mn atoms at the Y site.

Experimentally, antiferromagnetic order is measured both in half-Heusler ($C1_b$ structure) and in full-Heusler alloys ($L2_1$ and B2 structure). Antiferromagnetism is more favorable in full Heusler alloys presenting B2-type crystal structure due to smaller interatomic Mn-Mn distances. Antiferromagnetic behaviour has been reported in several B2-type disordered $X_2MnZ$ (X=Ni, Pd; Z=Al,In) Heusler alloys [57]. The situation is different in half-Heusler alloys. Due to large Mn-Mn distances in $C1_b$ structure the antiferromagnetic interaction between Mn atoms is assumed to be mediated by intermediate atoms (X or Z). Ferrimagnetic ordering (antiferromagnetic coupling of X and Y atoms) is very rare in Heusler alloys compared to ferromagnetic or antiferromagnetic order, though ferrimagnetism has been detected in CoMnSb, $Mn_2VAl$ and $Mn_2VGa$ compounds. $Mn_2VAl$ received much experimental attention, because it is among the few Heusler alloys where Mn sits in the X position. This compound is somewhat peculiar regardless of its detailed electronic structure: while there are many Heusler compounds of the form $X_2YZ$ where Y is Mn, in this compound the X site is occupied by Mn. When Mn sits on the Y site, it has a spin around $4\mu B$, while when sitting on the X site (which is the case for $Mn_2VAl$) it has a lower spin moment, in agreement with LDA calculation. Although V and Al atoms may substitute on each others sublattice, in the system $Mn_2V_{1-x}Al_{1-x}$ the lattice constant and x-ray intensities show a kink at x = 0, clearly identifying the stoichiometric composition. The structure remains the Heusler one from x between -0.3 and +0.2, with linearly varying saturation moment. At stoichiometry the saturation moment is reported to be $1.9\mu B$ , close to the integral value characteristic of the spin moment of half-metallic magnets and the Curie temperature is $T_C = 760K$.

## 2.5 band structure calculations

The band structure calculations of Heusler alloys has been initiated by Ishida et al., in the early eighties. The authors used non-self-consistent spherical augmented plane wave method (SAPW) to study electronic structure of $Ni_2MnSn$, $Pd_2MnSn$ [62] and $Cu_2MnAl$ [63].

In 1983 Kübler et al., gave a detailed study on the formation and coupling of the magnetic moments in several Heusler alloys using self-consistent augmented spherical wave method (ASW) [64]. In the same year de Groot et al., [65] discovered the half-metallic ferromagnetism in semi Heusler compounds NiMnSb and PtMnSb. Since then many efforts have been devoted to the study of electronic and magnetic properties of these systems on the basis of band structure calculations. Here we would like to present the theoretical explanations given in literature, which should help us to clarify the behaviour of these systems, starting from a theoretical background.

The origin of ferromagnetic behaviour in Heusler alloys is rather complicated and the mechanisms of magnetic moment localization in transition metals (and their alloys) is one of the most interesting problems in modern magnetism. The picture that emerged from the systematic calculations of Kübler et al. of the microscopic mechanism responsible for the formation of magnetic moments in these systems is that the magnetization is very much confined to the Mn atoms. The localized character of the magnetic moment results from the fact that the large exchange splitting of the Mn d states implies that Mn atoms support d states of only one spin direction. In the ferromagnetic state the spin-up d electrons of the Mn atom hybridize with those of the X atoms in forming a common d band, but spin-down d electrons are almost completely excluded from the Mn sites. Thus we are left with the completely localized magnetic moments composed of completely itinerant electrons. Using the calculated total energies, it was possible to compare the relative stability of various magnetic phases (one ferromagnetic phase and two different antiferromagnetic ones) for a number of Heusler compounds [64] and study the coupling of magnetic moments. Based on these results, it was found that there is no significant direct interaction between the d states on different Mn atoms.

## 2.5.1 Half-metallic ferromagnetism

The concept of half-metallic ferromagnetism was introduced by de Groot et al., on the basis of band structure calculations in NiMnSb and PtMnSb semi Heusler compounds [64]. In these materials one of the spin sub-bands (usually majority spin band) is metallic, whereas the Fermi level falls into a gap of the other sub-band. Ishida et al. have proposed that also the full-Heusler alloys of the type $Co_2MnZ$, (Z=Si,Ge) are half-metals. Since then a number of further systems were predicted to be half-metallic. Among them the binary magnetic oxides ($CrO_2$ and $Fe_3O_4$), colossal magnetoresistance materials ($Sr_2FeMoO_6$, $CrO_2$ and $La_{0,7}Sr_{0,3}MnO_3$), diluted magnetic semiconductors (GaAs, $Ga_{1-x}Mn_xAs$) and zinc-blende compounds MnAs and CrAs.

## 2.5.2 Origin of the half-metallic gap

The half-metallic ferromagnetism of Heusler alloys is intimately connected to their $C1_b$ crystal structure and consequently to the symmetry of the system. Due to a vacant site at the position (1/2,1/2,1/2) in the $C1_b$ crystal structure the symmetry of the systems is reduced to tetrahedral from the cubic in the case of $L2_1$ type full Heusler alloys. As described by Galanakis et al. [66] the gap arises from the covalent hybridization between the lower-energy d states of the high-valent transition metal atom (like Ni or Co) and the higher-energy d states of the lower-valent atom, leading to the formation of bonding and anti-bonding bands with a gap in between. The bonding hybrids are localized mainly at the high-valent transition metal atom site while the unoccupied anti-bonding states are mainly at the lower-valent transition metal atom site. This is shown schematically in figure 2.10. All Mn atoms are surrounded by six Z nearest neighbors - for the Mn atom at the (0,0,0) these neighbors are at (1/2,0,0), (0,1/2,0); (0,0,1/2), (-1/2,0,0),(0, -1/2,0) and (0,0,1/2). As a result the interaction of Mn with the Z sp states splits the Mn 3d states into a low-lying triplet of $t_{2g}$ states (dxy; dxz and a higher lying doublet of eg states $dx^2-y^2$ , $d3z^2-r^2$ ). The splitting is partly due to the different electrostatic repulsion, which is strongest for the eg states which directly point at the Z atoms.

In the majority band the Mn 3d states are shifted to lower energies and form a common 3d band with X (X=Ni, Co) 3d states, while in the minority band the Mn 3d states are shifted to higher energies and are unoccupied. A band gap at $E_F$ is formed, which separates the occupied d bonding states from the unoccupied d antibonding states as shown in the figure 2.10.

For instance, in the compound NiMnSb the minority occupied bonding d states are mainly of Ni character while the unoccupied anti-bonding states are mainly of Mn character. These structures are particularly stable when only the bonding states are occupied. The p states strongly hybridize with the transition metal d states and the charge in these bands is delocalized. What counts is that the s and p bands accommodate eight electrons per unit cell, effectively reducing the d charge of the transition metals atoms. The sp-elements like Sb play an important role for the existence of the Heusler alloys with a gap at the $E_F$. Thus NiMnSb is a half-metal with a gap at $E_F$ in minority band and a metallic DOS at the Fermi level in majority band. Also for systems with more (or less) than 18 electrons, the gap can still exist.
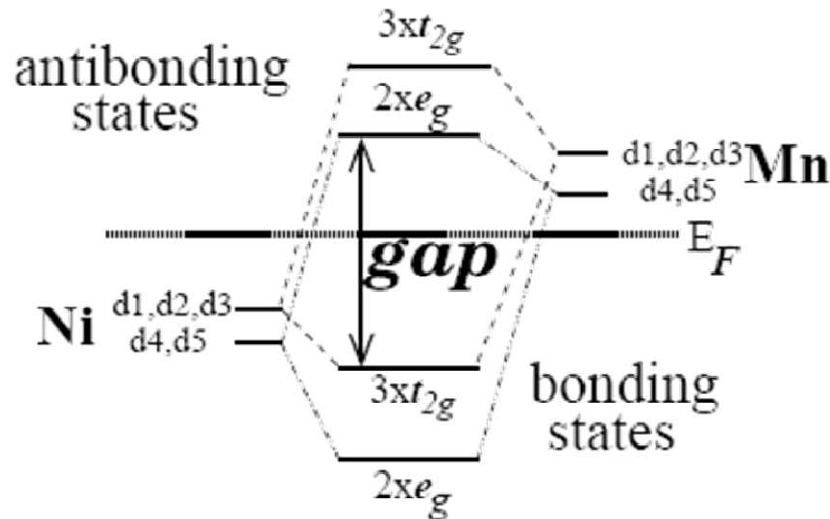


**Fig. 2.10:** Illustration of the origin of the gap in the minority band in half-Heusler alloys, as described in ref. [66].

The explanation of the valence and conduction bands given in ref.[66] is internally consistent. It explains the existence of exactly nine minority valence bands and simultaneously describes the magnetic properties of these compounds. With small modifications it can be also extended to explain the properties of the half-ferromagnetic full-Heusler alloys like $Co_2MnGe$. Nevertheless the Sb atoms or in general the sp atoms are important for the properties of the Heusler alloys. The calculated total magnetic moment is $4\mu B$ per unit cell and mostly located in Mn atom. NiMnSb has 22 valence electrons per unit cell, 10 from Ni, 7 from Mn and 5 from Sb. Because of the gap at $E_F$ , in the minority band exactly 9 bands are fully occupied (1 Sb-like s band, 3 Sb-like p bands and 5 Ni-like d bands) and the remaining 13 electrons are accommodated in majority band, resulting in a magnetic moment of 13-9=4$\mu B$ per unit cell. Note that half-Heusler alloys like CoTiSb with 18 valence electrons show semiconducting behavior. It should be noted that the halfmetallic character of half-Heusler compounds is highly sensitive to the crystal structure and symmetry e.g., the cubic point symmetry at Mn sites in ordinary $X_2MnZ$ Heusler alloys gives rise to a symmetry of Mn-3d-t2g, states that is different from the symmetry of the Sb p states. Hence, these states do not hybridize, so that no gap is opened in the minority spin band.

### 2.5.3 Slater-Pauling behavior

The total moment of the half- and full-Heusler alloys follows the rule: $M_t = Z_t - 18$ (half) and $M_t = Z_t - 24$ (full) where $Z_t$ is the total number of valence electrons [23]. $Z_t$ is given by the sum of the number of spin-up and spin-down electrons $Z_t = N\uparrow + N\downarrow$, while the total moment $M_t$ is given by the difference $M_t = N\uparrow - N\downarrow$. Since 9 (12) minority bands of half (full) Heusler alloys are fully occupied, a simple rule of 18 (24) is obtained for half-metallicity in $C1_b$-type ($L2_1$) Heusler alloys. This is analogous to the well-known Slater-Pauling behavior of the binary transition metal alloys.
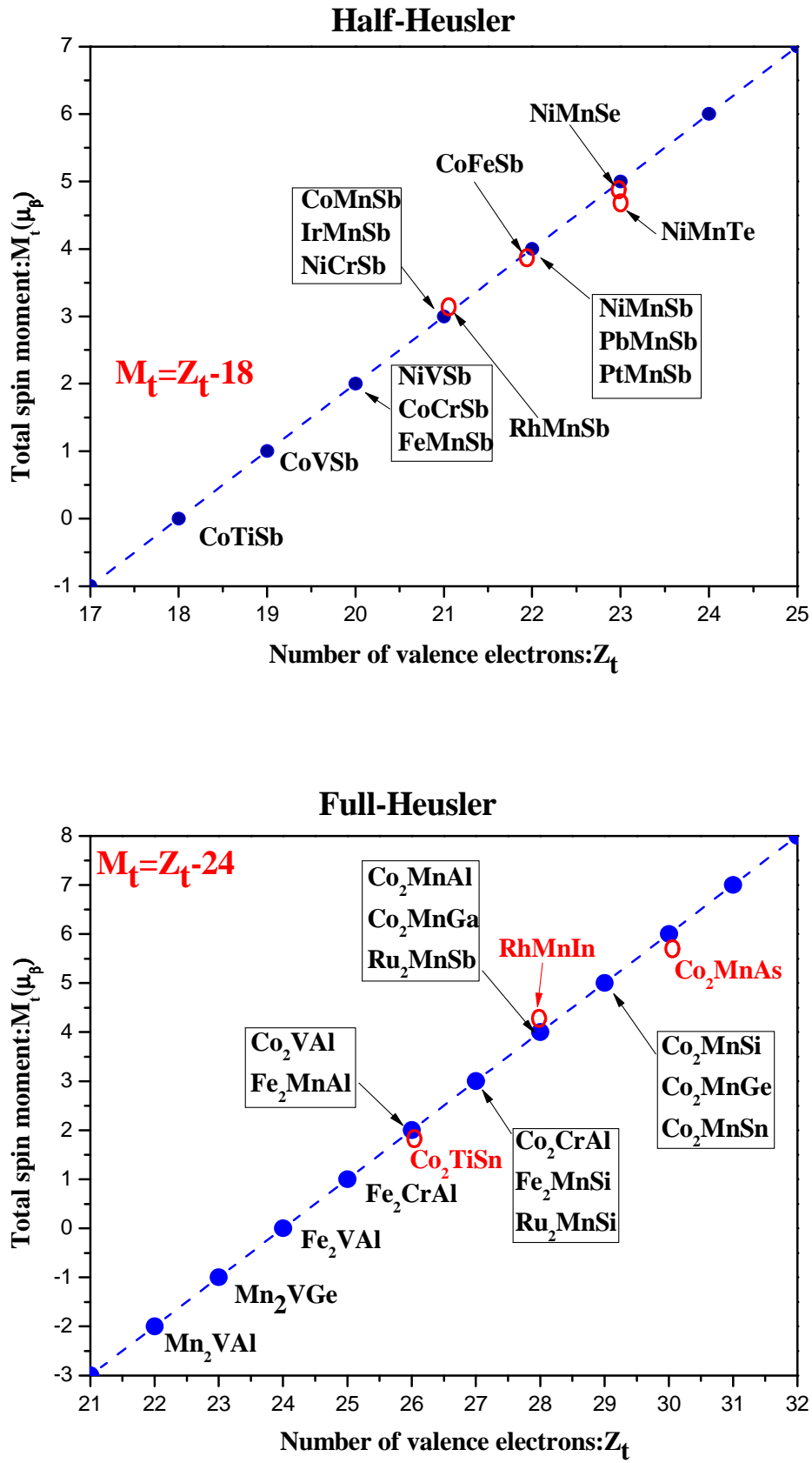
**Fig 2.11:** Total spin moments for half- Heusler alloys  and full- Heusler

The dashed line represents the Slater Pauling behavior. The open circles indicate the compounds deviating from SP behavior. The difference with respect to these alloys is that in the half-Heusler alloys the minority population is fixed to 9 and 12, so that the screening is achieved by filling the majority band, while in the transition metal alloys the majority band is filled with 5d states or completely empty and charge neutrality is achieved by filling the minority or majority states. Therefore in the transition metals alloys the total moment is given by $M_t = 10 - Z_t$ for the systems on the left side and $M_t = Z_t$ for the systems on the right side of the Slater-Pauling curve. For the half-metallic zinc-blende compounds like CrAs the rule is: $M_t = Z_t - 8$, since the minority As-like valence bands accommodate 4 electrons. In all cases the moments are integer. In Figure 2.11 the calculated total spin magnetic moments for both Heusler alloys, plotted as a function of the total number of valence electrons, are gathered. The dashed line represents the rule $M_t = Z_t - 18$ ($M_t = Z_t - 24$) fulfilled by these compounds. The total moment Mt is an integer quantity, assuming the values 0, 1, 2, 3, 4 and 5 if $Z_t > 18$. In the case of full Heusler alloys ($Z_t = 24$) $M_t$ can also take -2, -1 and 6. The value 0 corresponds to the semiconducting phase [67].

# References

[1] S. M. Sze and K. K. Ng, Physics of Semiconductor Devices. Wiley, (2006)

[2] G. E. Moore, Proceedings of the IEEE **86**, (1998) 82-85

[3] B. D. Rizzo, NVIDIA Introduces Ge Force GTX TITAN: DNA Of The World's Fastest Supercomputer, Powered By World's Fastest GPU, <http://nvidianews.nvidia.com/Releases/NVIDIA-Introduces-GeForce -GTX-TITAN-DNA-of-the-World-s-Fastest-Supercomputer-Powered-by-World-s-Fa-925.aspx> (2013)

[4] N. S. Kim, T.Austin, D. Baauw, T. Mudge, K. Flautner, J. S. Hu, M. J. Irwin, M. Kandemir and V. Narayanan, Computer **36**, (2003) 68-75

[5] D. D. Awschalom and M. E. Flatte, Nature Physics **3**, (2007) 153-159,

[6] G. A. Prinz, Science **282**, (1998)1660-1663

[7] G. A. Prinz Journal of Magnetism and Magnetic Materials **200**, (1999) 57-68

[8] S. Datta and B. Das Applied Physics Letters **56**, (1990) 665-667

[9] W. Thomson, Proceedings of the Royal Society of London **8**, (1856) 546-550

[10] A. Brataas, A. D. Kent and H. Ohno, Nature Materials **11**, (2012) 372-381

[11] S. S. P. Parkin, Physical Review Letters **67**, (1991) 3598-3601

[12] G. Binasch, P. Grünberg, F. Saurenbach and W. Zinn, Physical Review B **39**, (1989) 4828-4830

[13] M. N. Baibich, J. M. Broto, A. Fert, F. N. Van Dau, F. Petroff, P. Etienne, G. Creuzet, A. Friederich, and J. Chazelas, Physical Review Letters **61**, (1988) 2472-2475

[14] N. F. Mott, Proceedings of the Royal Society of London. Series A, Mathematical and Physical Sciences **153**, (1936) 699-717

[15] N. F. Mott, Proceedings of the Royal Society of London. Series A, Mathematical and Physical Sciences **156**, (1936) 368-382

[16] I. A. Campbell, A. Fert, and R. Pomeroy, Philosophical Magazine **15**, (1967) 977-983

[17] A. Fert, and I. A. Campbell, Physical Review Letters **21**, (1968) 1190-1192

[18] S. M. Thompson, Journal of Physics D: Applied Physics **41**, (2008) 093001

[19] T. M. Nakatani, , T. Furubayashi, and K. Hono, Journal of Applied Physics **109**, (2011) 724-723

[20] M. Julliere, Physics Letters A 54, (1975) 225-226

[21] T. Miyazaki, and N. Tezuka, Journal of Magnetism and Magnetic Materials 139, (1995) 231-234

[22] J. S. Moodera, L. R. Kinder, T. M. Wong, and R. Meservey, Physical Review Letters 74, (1995) 3273-3276

[23] W. H. Butler, X. G. Zhang, T. C. Schulthess, and J. M. MacLaren, Physical Review B **63**, (2001) 054416

[24] S. Ikeda, J. Hayakawa, Y. Ashizawa, Y. M. Lee, K. Miura, H. Hasegawa, M. Tsunoda, F. Matsukura, and H. Ohno, Applied Physics Letters **93**, (2008) 082508-082503

[25] Slonczewski, J. C. Journal of Magnetism and Magnetic Materials 159, (1996) 1-7

[26] L. Berger, Journal of Applied Physics **55**, (1984) 1954-1956

[27] S. Maekawa, S. O. Valenzuela, E. Saitoh and T. Kimura, Spin Current. OUP Oxford, (2012)

[28] R. A. de Groot, F. M. Mueller, P. G. v. Engen and K. H. J. Buschow, Physical Review Letters 50, (1983) 2024-2027

[29] C. Felser, and B. Hilllebrands, Journal of Physics D: Applied Physics (2007) 40

[30] H. C. Kandpal, G. H. Fecher and C. Felser, Journal of Physics D: Applied Physics **40**, (2007) 1507

[31] C. G. F. Blum, C. A. Jenkins, J. Barth, C. Felser, S. Wurmehl, G. Friemel, C. Hess, G. Behr, B. Buchner, A. Reller, S. Riegg, S. G. Ebbinghaus, T. Ellis, P. J. Jacobs, J. T. Kohlhepp and H. J. Swagten, M. Applied Physics Letters **95**, (2009) 161903-161903

[32] R. S. Keizer, S. T. B. Goennenwein, T. M. Klapwijk, G. Miao, G. Xiao and A. Gupta, Nature **439**, (2006) 825-827

[33] Y. W. Son, M. L. Cohen and S. G. Louie, Nature **444**, (2006) 347-349

[34] N. Tezuka, N. Ikeda, F. Mitsuhashi and S. Sugimoto, Applied Physics Letters **94**, (2009) 162504-162503,.

[35] V. K. Lazarov, K. Yoshida, J. Sato, P. J. Hasnip, M. Oogane, A. Hirohata and Y. Ando, Applied Physics Letters **98**, (2011) 242508-242503,.

[36] T. Ambrose, J. J. Krebs and G. A. Prinz, Applied Physics Letters **76**, (2000) 3280-3282

[37] D. Ebke, J. Schmalhorst, N. N. Liu, A. Thomas, G. Reiss and A. Hutten, Applied Physics Letters **89**, (2006) 162506-162503

[38] K. Inomata, S. Okamura, A. Miyazaki, M. Kikuchi, N. Tezuka, M. Wojcik and E. Jedryka, Journal of Physics D: Applied Physics **39**, (2006) 816

[39] T. M. Nakatani, A. Rajanikanth, Z. Gercsi, Y. K. Takahashi, K. Inomata and K. Hono, Journal of Applied Physics 102, (2007) 033916-033918

[40] R. Shan, H. Sukegawa, W. H. Wang, M. Kodzuka, T. Furubayashi, T. Ohkubo, S. Mitani, K. Inomata and K. Hono, Physical Review Letters **102**, (2009) 246601

[41] T. M. Nakatani, T. Furubayashi, S. Kasai, H. Sukegawa, Y. K. Takahashi, S. Mitani and K. Hono, Applied Physics Letters **96**, (2010) 212501-212503

[42] H. Sukegawa, S. Kasai, T. Furubayashi, S. Mitani and K. Inomata, Applied Physics Letters **96**, (2010) 042508-042503

[43] T. Furubayashi, K. Kodama, H. S. Goripati, Y. K. Takahashi, K. Inomata and K. Hono, Journal of Applied Physics **105**, (2009) 305-303,.

[44] T. M. Nakatani, Y. Du, Y. K. Takahashi, T. Furubayashi and K. Hono, Acta Materialia **61**, (2013) 3695-3702

[45] C. M. Fang, G. A. de Wijs, and R. A. de Groot, J. of Appl. Phys., vol. **91**, (2002)8340-8344

[46] R. Weht and W. E. Pickett, Phys. Rev. B, vol. **60**, (1999) 006-010

[47] F. Heusler, Verh. Dtsch. Phys. Ges., vol. **5**, (1903) 219

[48] H. H. Potter, Proc. Phys. Soc., vol. **41**, (1929) 135

[49] A. J. Bradley and J. W. Rodgers, Proc. R. Soc. London Ser. A, vol. **144**, (1934) 340

[50] H. Itoh, T. Nakamichi, Y. Yamaguchi, and N. Kazama, Trans. Jpn. Inst. Met., vol. **24**, (1983) 265

[51] K. H. J. Buschow and P. G. van Engen, J. Mag. Magn. Mater., vol. **25**, (1981) 90

[52] P. J. Webster and K. R. A. Ziebeck, Alloys and Compounds of d-Elements with Main Group Elements - Part 2. H. P. J. Wijn, Landolt-Bornstein, New Series, Group III, Vol. 19/c (Springer, Berlin), (1988).

[53] P. J. Webster, K. R. A. Ziebeck, and K.-U. Neumann, Magnetic Properties of Metals. Landolt-B ornstein, New Series, Group III, Vol. 32/c (Springer, Berlin), (2001).

[54] J. Pierre, R. V. Skolozdra, J. Alloys Comp., vol. **101**,  (1997) 262-263

[55] J. Tobola, J. Pierre, S. Kaprzyk, R. Skolozdra, and M. Kouacou, J. Phys.: Condens. Matter, vol. **10**, (1998) 1013

[56] S. Ishida, Y. Kubo, J. Ishida, and S. Asano, J. Phys. Soc. Jpn., vol. **48**, (1980) 814

[57] S. Ishida, J. Ishida, S. Asano, and J. Yamashita, J. Phys. Soc. Jpn., vol. **45**, (1978) 1239

[58] J. Kuebler, A. R. Williams, and C. B. Sommers, Phys. Rev. B, vol. **28**, (1983) 4

[59] R. A. de Groot, F. M. Mueller, P. G. van Engen, and K. H. J. Buschow, Phys. Rev. Lett, vol. **50**, (1983) 2024

[60] I. Galanakis, P. H. Dederichs, and N. Papanikolaou, Phys. Rev. B, vol. **66**, (2002) 134428

[61] I. Galanakis, P. H. Dederichs, and N. Papanikolaou, Phys. Rev. B, vol. **66**, (2002) 174429

[62] S. Ishida, S. Akazawa, Y. Kubo, and J. Ishida, J. Phys. F: Met. Phys., vol. **12**, (1982) 1111

[63] S. Kaemmerer, S. Heitmann, D. Meyners, D. Sudfeld, A.Thomas, A. Huetten, and G. Reiss, Journ. Appl. Phys., vol. **93**, (2003) 10

[64] T. Saito, T. Katayama, T. Ishikawa, M. Yamamoto, D. Asakura, and T. Koide, Appl. Phys. Lett., vol. **91**, (2007) 262502

[65] A. Bergmann, PhD thesis, Ruhr-University, Bochum, (2006)

[66] J. Sagar, PhD thesis, Department of Physics, University of York, (2013)

[67] M. Vadala, PhD thesis, faculty of physics and astronomy, Ruhr-University, Bochum, (2008)

# Part III

# Density Functional Theory (DFT)

# 3 Density Functional Theory

P hysics and chemistry use a theory called Density functional theory (DFT), which is a quantum mechanical theory, to examine the electronic structure of many body systems, especially, atoms, molecules and the condensed phases. DFT is one of the most common and flexible technique obtainable in condensed matter physics, computational physics, and computational chemistry [1], due to its capability to deal with large numbers of electrons with complete precision [2].

Time-dependent density-functional theory (TDDFT) is the generalization of ground-state DFT to include time-dependent external potentials on electrons, and its formal validity was set up with the Runge- Gross theorem [3]. The analogous connection between time-dependent densities and time-dependent potentials for a given preliminary state guides to the time-dependent Kohn-Sham system, which is a set of no interacting presumptive electrons moving in a time-dependent Kohn-Sham potentials.

TDDFT has been applied to many problems in atomic, molecular and solid state systems, including optical response, dynamic polarizabilities and hyper-polarizabilities, excitation energies, species in intense laser fields and highly energetic collisions [4].

The principle of DFT is to illustrate an interconnecting system of fermions by means of its density and not by its many-body wave function [5]. While DFT chiefly gives a good explanation and portrayal of ground state qualities. Practical applications of DFT rely on rough calculations for the so-called exchange-correlation probability. The exchange-correlation probability portrays the influences of the Pauli principle and the Coulomb possibility beyond a pure electrostatic interaction of the electrons. The precise exchange-correlation probability gives a solution of the many-body problem precisely, which is obviously not possible in solids [6].

In spite of the fact that density functional theory has its theoretical roots in the Thomas-Fermi model, it was put on a solid hypothetical foundation by the two Hohenberg-Kohn theorems (H-K) [7]. The original H-K theorems held only for non-degenerate ground states in the absence of a magnetic field, although they have since been generalized to include them [8].

The ground state properties of a many-electron system are exclusively decided by an electron density that depends only on 3 spatial coordinates, this is shown in the first H-K theorem. It puts down the base work for reducing the many-body problem of N electrons with 3N spatial coordinates to only 3 spatial coordinates, by the use of functional of the electron density. This theorem can be expanded to the time-dependent sphere to build up time-dependent density functional theory, which can be applied to portray stimulated conditions. The second H-K theorem defines an energy functional for the system and gives evidences to prove that the proper ground state electron density reduces this energy functional [1].

The intractable many-body problem of interacting electrons in a static external potential, within the framework of Kohn-Sham DFT(KSDFT), is reduced to a tractable problem of non-interacting electrons moving in an effectual potential. The effective potential contains the external potential and the effects of the Coulomb interactions between the electrons, e.g., the exchange and correlation interactions. Modeling the latter two interactions becomes the difficulty within KS DFT. The simplest rough calculation is the local-density approximation (LDA), which depends on precise exchange energy for a uniform electron gas, which can be obtained from the Thomas-Fermi model, and from fits to the correlation energy for a uniform electron gas.

## 3.1 The Hohenburg-Kohn Theorems

Hohenberg and Kohn [6] were the first to formulate the special place of DFT in 1964 which becomes directly clear from the fundaments, Here a derivation of DFT and its formula.

The nuclei of the treated molecules or clusters, as usual in many body electronic structure calculations, are seen as fixed (the Born-Oppenheimer approximation), generating a static external potential $V$ in which the electrons are moving. A stationary electronic state is then portrayed by a wave function $\Psi(\vec{r}_1, \dots, \vec{r}_N)$ satisfying the many-electron Schrodinger equation:

$$
\begin{aligned}
\widehat{H}\Psi &= \left[\widehat{T} + \widehat{V} + \widehat{U}\right]\Psi \\
&= \left[\sum_i^N -\frac{\hbar^2}{2m}\nabla_i^2 + \sum_i^N V(\vec{r}_i) + \sum_{i<j}^N U(\vec{r}_i, \vec{r}_j)\right]\Psi \\
&= E\,\Psi
\end{aligned}
\tag{3.1}
$$

Where $\widehat{H}$ is the electronic molecular Hamiltonian, N is the number of electrons, $\widehat{T}$ is the N-electron kinetic energy, $\widehat{V}$ is the N–electron potential energy from the external field, and $\widehat{U}$ is the electron-electron interaction energy for the N-electron system. The operators $\widehat{T}$ and $\widehat{U}$ are so-called universal operators as they are alike for any system, while $\widehat{V}$ is system dependent, i.e. non-universal. The differentiation between having separate single-particle problems and the much more complex many-particle problem stems from the interaction term $\widehat{U}$.

The many-body Schrodinger equations solved by many complicated technique based on the extension of the wave function in Slater determinants. While the easiest one is the Hartree-Fock technique, more sophisticated techniques are usually classified as post-Hartree-Fock techniques. However, the problem with these techniques is the vast computational effort, which makes it almost unfeasible to apply them competently to larger, more complicated systems.

Here DFT offers an attractive substitute, being much more adaptable as it provides a way to systematically map the many-body problem, with $\hat{U}$, onto a single-body problem without $\hat{U}$. In DFT the key changeable is the particle density $n(\vec{r})$ , which for a normalized is given by:

$$n(\vec{r}) = N \int d^3r_1 \int d^3r_2 \dots \int d^3r_N \Psi^*(\vec{r}_1\vec{r}_2, \dots, \vec{r}_N)\Psi(\vec{r}_1\vec{r}_2, \dots, \vec{r}_N) \qquad (3.2)$$

This relation can be reversed, that is to say, for a given ground-state density $n_0(\vec{r})$ it is principally potential, to work out the equivalent ground-state wave function $\Psi_0(\vec{r}_1,\dots, \vec{r}_N)$. That is to say, $\Psi_0$ is a sole functional of $n_0$, $\Psi_0 = \Psi[n_0]$ and as a result the ground-state expectation value of an observable $\hat{O}$ is also a functional of $n_0$

$$O[n_0] = \langle \Psi[n_0] | \hat{O} | \Psi[n_0] \rangle \qquad (3.3)$$

In particular, the ground-state energy is a functional of $n_0$

$$\begin{aligned} E_0 = E[n_0] &= \langle \Psi[n_0] | \hat{T} + \hat{V} + \hat{U} | \Psi[n_0] \rangle \\ &= \langle \Psi[n_0] | \hat{T} | \Psi[n_0] \rangle + \langle \Psi[n_0] | \hat{V} | \Psi[n_0] \rangle + \langle \Psi[n_0] | \hat{U} | \Psi[n_0] \rangle \\ &= \hat{T}[n_0] + \hat{V}[n_0] + \hat{U}[n_0] \qquad (3.4) \end{aligned}$$

Where the contribution of the external $\langle \Psi[n_0] | \hat{V} | \Psi[n_0] \rangle$

The potential can be written clearly in terms of the ground-state density $n_0$

$$V[n_0] = \int V(\vec{r}) n_0(\vec{r}) d^3r \qquad (3.5)$$

More commonly, the contribution of the external potential $\langle \Psi | \hat{V} | \Psi \rangle$ can be written clearly in terms of the density n,

$$V[n] = \int V(\vec{r})n(\vec{r})d^3r \qquad (3.6)$$

As mentioned above, the functional $T[n]$ and $U[n]$ are called universal functional, whereas $V[n]$ is called a non-universal functional, as it relies on the system under study. Having a definite system, i.e., having specified $\hat{V}$, one then has to reduce the functional

$$E(n) = T[n] + U[n] + \int V(\vec{r})n(\vec{r})d^3r \qquad (3.7)$$

In regards to $n(\vec{r})$, taking for granted one has got dependable terms for $T(n)$ and $U(n)$. A successful reduction of the energy functional will produce the ground-state density $n_0$ and thus all other ground-state observables.

The Lagrangian technique of undetermined multipliers [7] can be applied to solve the variation problems of minimizing the energy functional $E(n)$. First, one takes into accounts an energy functional that doesn't clearly have an electron-electron interaction energy term,

$$E_s[n] = \langle \Psi_s[n] | \hat{T}_s + \hat{V}_s | \Psi_s[n] \rangle \qquad (3.8)$$

where $\hat{T}_s$ indicates the non-interacting kinetic energy and $\hat{V}_s$ is an external effectual potential in which the particles are moving. Clearly, if $\hat{V}_s$ is $n_s(\vec{r}) = n(\vec{r})$ selected to be

$$\hat{V}_s = \hat{V} + \hat{U} + (\hat{T} - \hat{T}_s) \qquad (3.9)$$

Consequently, one can solve the so-called Kohn-Sham equations of this assisting non-interacting system,

$$\left[-\frac{\hbar^2}{2m}\nabla^2 + V_s(\vec{r})\right]\Phi_i(\vec{r}) = \epsilon_i\Phi_i(\vec{r}) \tag{3.10}$$

which produces the $\Phi_i$ orbital that reproduce the density $n(\vec{r})$ of the authentic many-body system.

$$n(\vec{r}) = n_s(\vec{r}) = \sum_i^N |\Phi_i(\vec{r})|^2 \tag{3.11}$$

The effective single-particle potential can be written in more detail as

$$V_s(\vec{r}) = V(\vec{r}) + \int \frac{e^2 n_s(\vec{r}')}{|\vec{r}-\vec{r}'|} d^3r' + V_{XC}[n_s(\vec{r})] \tag{3.12}$$

where the second term stands for the so-called Hartree expression portraying the electron-electron Coulomb repulsion, while the last expression $V_{XC}$ is called the exchange-correlation possibility. Here, $V_{XC}$ has all the many-particle interactions. Since the Hartree expression and $V_{XC}$ rely on $n(\vec{r})$ , which relies on the $\Phi_i$ , which in turn relies on $\hat{V}_s$ , the problem of solving the Kohn-Sham equation has to be done in a selfconsistent way. One typically begins with an first guess for $n(\vec{r})$ , then works out the equivalent $\hat{V}_s$ and solves the Kohn-Sham equations for the $\Phi_i$ [1].

To conclude, techniques in DFT are complex and different, but can roughly be partitioned into three categories [8]:

- Techniques that apply a local density rough calculation (LDA). The LDA is decided exclusively and based on the qualities of the electron density. The significant supposition of this approximation is that, for a molecule with many electrons in a gaseous state, the density is consistent throughout the molecule.

This is not the case for molecules, where the electron density is decidedly not consistent.

This approximation does, however, work well with electronic band structures of solids, which illustrates the scope of energies in which electrons are allowed or not allowed . Outside of these applications, however, LDA's are not very acceptable.

- Techniques that unite the electron density calculations with a gradient correction factor. A gradient in mathematics is a function that measures the rate of change of some property. In this case, the gradient seems to explain the non-uniformity of the electron density, and as such is known as gradient-corrected. Another expression for this is non-local.

- Techniques that are a mixture of a HF approximation to the exchange energy and a DFT approximation to the exchange energy, all united with a functional that has electron correlation. These Techniques are known as hybrid techniques, and are now the most common and popular DFT techniques used in practically.

## 3.2 Kohn-Sham Equations

A set of eigen value equations within density functional theory (DFT) are called Kohn Sham equations. As mentioned above , DFT tries to minimize a many-body problem for the N particle wave function $\Psi_0(\vec{r}_1, \ldots, \vec{r}_N)$ to one in terms of the charge density $n(\vec{r})$ which relies on 3 variables, using the Hohenberg-Kohn theorems[9]. The total energy $E$ of the system as a functional of the charge density can be written as:

$$E(n) = T(n) + \int V_{ext}(r)n(r)dr + V_H[n] + E_{xc}[n] \tag{3.13}$$

where $T$ is the kinetic energy of the system, $V_{ext}$ is an external potential acting on the system, and

$$V_H = \frac{e^2}{2} \int \frac{n(r)n(r')}{|r-r'|} dr dr' \qquad (3.14)$$

Is the Hartree energy and Ex*c* is the exchange-correlation energy.

The straight forward application of this formula has two barriers:

First, the exchange-correlation energy Ex*c* is not known precisely, and second, the kinetic term must be created in terms of the charge density. As was first suggested by Kohn and Sham, the charge density n(r) can be written as the sum of the squares of a set of orthonormal wave functions $\Phi_i(r)$:

$$n(r) = \sum_i^N |\Phi_i(r)|^2 \qquad (3.15)$$

The unit of charge density n(r) is (c/m$^3$).

Equation (3-15) represents the solution to the Schrodinger equation for *N* non-interacting electrons moving in an effectual potential $V_{eff}(r)$

$$-\frac{\hbar^2}{2m} \nabla^2 \Phi_i(r) + V_{eff}(\vec{r})\Phi_i(r) = \varepsilon_i \Phi_i(r) \qquad (3.16)$$

where the effectual potential is defined to be

$$V_{eff}(r) = V_{ext}(r) + e^2 \int \frac{n(r')}{|r-r'|} dr' + \frac{\delta E_{xc}[n]}{\delta n} \qquad (3.17)$$

These three equations form the Kohn-Sham orbital equations in their standard form. This system is then solved iteratively, until self-consistency is approached. Note that the eigen values $\varepsilon_i$ have no physical meaning, only the total sum, which matches the energy of the entire system *E* through the equation [10]:

$$E = \sum_i^N \varepsilon_i - V_H[n] + E_{xc}[n] - \int \frac{\delta E_{xc}[n]}{\delta n(r)} n(r) dr \qquad (3.18)$$

Schematic representation of the self-consistent loop for solution of the Kohn-Sham equations. Generally speaking one must repeat two such circles at once for the two spins, with the potential for each spin relying upon the density of both spins [11].

Practically, there are several distinct ways in which Kohn-Sham theory can be applied depending on what is being examined. In solid state calculations, the local density approximations are still commonly used along with plane wave basis sets, as an electron gas approach is more suitable for electrons delocalized through an infinite solid. In molecular calculations, however, more complicated functional are needed, and a huge variety of exchange-correlation functional have been developed for chemical applications. Some of these are incompatible with the uniform electron gas approximation, however, they must reduce to LDA in the electron gas limit. For molecular applications, in particular for hybrid functional, Kohn-Sham DFT techniques are usually applied just like Hartree-Fock itself [12].

The main difficulty with DFT is that the precise functional for exchange and correlation are not identified except for the free electron gas. However, rough calculations exist which allow the calculation of certain physical amounts rather precisely. In physics the most widely used approximation is the local-density approximation (LDA).

# Self-Consistent Kohn–Sham Equations

**Initial Guess**

$$n^{\uparrow}(r), n^{\downarrow}(r)$$

**Calculate Effective Potential**

$$V^{\sigma}(r) = V_{ext}(r) + V_{Hart}[n] + V_{xc}^{\sigma}[n^{\uparrow}, n^{\downarrow}]$$

**Solve KS Equation**

$$\left( -\tfrac{1}{2}\nabla^2 + V^{\sigma}(r) \right)\psi_i^{\sigma}(r) = \varepsilon_i^{\sigma}\psi_i^{\sigma}(r)$$

**Calculate Electron Density**

$$n^{\sigma}(r) = \sum_i f_i^{\sigma}\left|\psi_i^{\sigma}(r)\right|^2$$

**Self-consistent?**

No

Yes

**Output Quantities**

**Compute Energy, Forces, Stresses**
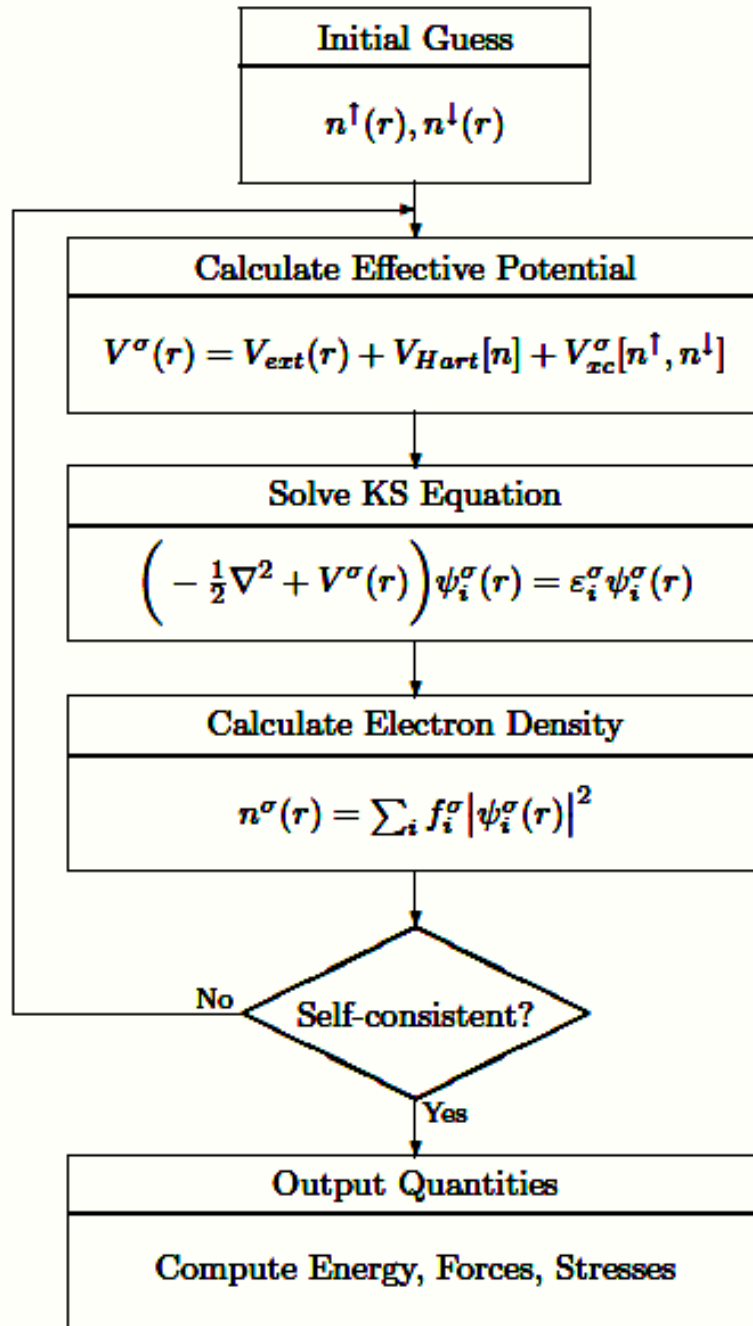
**Fig. 3.1:** flow chart of solving the self-consistent Kohn-Sham equation

## 3.3 Local Density Approximation

One of the efficient rough calculation techniques for working out the exchange-correlation term in the density functional theory (DFT) is the local density approximation (LDA). LDA has widely been applied to portray a variety of close-ranged exchange-correlation interactions of, for instance, covalent bonding systems. However, LDA has serious limitation that this approximation cannot provide estimation to the long-ranged exchange-correlation interaction, as typified by the Van der Waals (VdW) interaction. The VdW interaction is one of the long-ranged electronic interactions which mainly add to the first stage of the material reactions such as the chemical reaction, crystal growth and physical absorption. To assess the VdW interaction, many efforts have been devoted to develop useful calculating recipes for the non-local exchange-correlation term [13].

Kohn and Sham applied LDA approximation to DFT [9]. The Hohenberg-Kohn theorem states that the energy of the ground state of a system of electrons is a functional of the electronic density, especially, the exchange and correlation (XC) energy is also a functional of the density (this energy can be seen as the quantum part of the electron-electron interaction). This XC functional is not identified accurately and must be approximated [6]. LDA is the simplest approximation for this functional, it is local in the sense that the electron exchange and correlation energy at any point in space is a function of the electron density at that point only.

The XC functional is the total of a correlation functional and an exchange functional:

$$E_{xc} = E_x + E_c \tag{3.19}$$

LDA uses the exchange for the uniform electron gas of a density equal to the density at the point where the exchange is to be assessed:

$$E_{xc} = \int d^3 r n(\vec{r}) \left(\frac{-3e^2}{4\pi}\right) (3\pi^2 n(\vec{r}))^{1/3} \tag{3.20}$$

In SI units, $n(\vec{r})$ is the electron density per unit volume at the point $\vec{r}$ ; and e is the charge of an electron [14].

While looking for the ways out to the system of Schrodinger equation:

$$E\Psi(x) = -\frac{1}{2m} \nabla^2 \Psi(x) + V(x)\Psi(x) \tag{3.21}$$

It is found that all amounts are represented as functional of the electronic $\varepsilon_{xc}(r)$ charge density. The significant point that makes this system easier to solve (or more accurately, needs less computation) than, for instance the Hartree-Fock equations, is that the efficient possibility is local. Therefore there is no more complication added in solving Schrodinger equation than there is in the Hartree approximation. Of course, this is only true if the exchange-correlation energy can be portrayed as a function of the local charge density. A technique of doing so is known as the local density approximation (LDA) [9]. As mentioned above in LDA, the exchange-correlation energy of an electronic system is built by taking for granted that the exchange-correlation energy for each electron at a point $\vec{r}$ in the electron gas is equal to the exchange-correlation energy for each electron in a identical electron gas that has the same electron density at the point $\vec{r}$ . It follows that:

$$E_{xc}[n(\vec{r})] = \int \varepsilon_{xc}(n(\vec{r})n(\vec{r})dr \tag{3.22}$$

So that

$$\mu_{xc}(\vec{r}) = \frac{\delta[n(\vec{r})\varepsilon_{xc}(n(\vec{r}))]}{\delta n(\vec{r})} \tag{3.23}$$

With

$$\varepsilon_{xc}\big(n(\vec{r})\big) = \varepsilon_{xc}^{hom}(n(\vec{r}))  \qquad\qquad (3.24)$$

Where $\varepsilon_{xc}^{hom}(n(\vec{r}))$ is exchange-correlation energy in identical electron gas. Equation (3-24) is the supposition that the exchange correlation energy is purely local. Several parameterizations for $\varepsilon_{xc}^{hom}(n(\vec{r}))$ exist, but the most commonly used is that of Perdew and Zunger [15]. This parameterisation is based on the quantum Monte Carlo calculations of Ceperley and Alder [16] on homogeneous electron gases at various densities. The parameterization uses interpolation formulas to link these precise outcomes for the exchange and correlation energy at many dissimilar densities.

Adjustment to the exchange-correlation energy because of the inhomogeneities in the electronic charge density about $\vec{r}$ are overlooked, in LDA,. Therefore, it may at first seem somewhat surprising that such calculations are so successful, when taking into account this inexact nature of the approximation. This can be to some extent ascribed to the fact that LDA gives the accurate sum rule to the exchange-correlation hole. That is, there is a total electronic charge of one electron excluded from the vicinity of the electron at $\vec{r}$. Endeavors to improve on LDA, such as gradient extensions to correct for in-homogeneities do not seem to show any enhancement in results got by the simple LDA. One of the reasons for this failure is that the sum rule is not obeyed by the exchange-correlation hole.

The contributions of electron-electron interactions in N-electron systems are shown briefly in Figure (3.2). It demonstrates the conditional electron probability distributions *n* (*r*) of *N*-1 electrons around an electron with given spin located at r = 0.

All electrons are dealt with as independent, in the Hartree approximation [19], Figure (3-2a), therefore is structureless. Figure (3-2b) stands for the Hartree-Fock approximation where the N-electron wave function reflects the Pauli exclusion principle.

Around the electron at r = 0. The exchange hole can be seen where the density of spins equal to that of the central electron is reduced. Electrons with opposite spins are unchanged. In the LDA (Figure (3-2c)), where spin states are degenerate, each sort of electron sees the same exchange-correlation hole (the sum rule being demonstrated where the size of the hole is one electron).

Figure (3-2d) shows electron-electron interaction for non-degenerate spin systems (the local spin density approximation (LSDA). It can be seen that the spin degenerate LDA is basically the average of the LSDA.

GGA's approximation has minimized the LDA errors of atomization energies of standard set of small molecules. This enhanced precision has made DFT an important element of quantum chemistry.
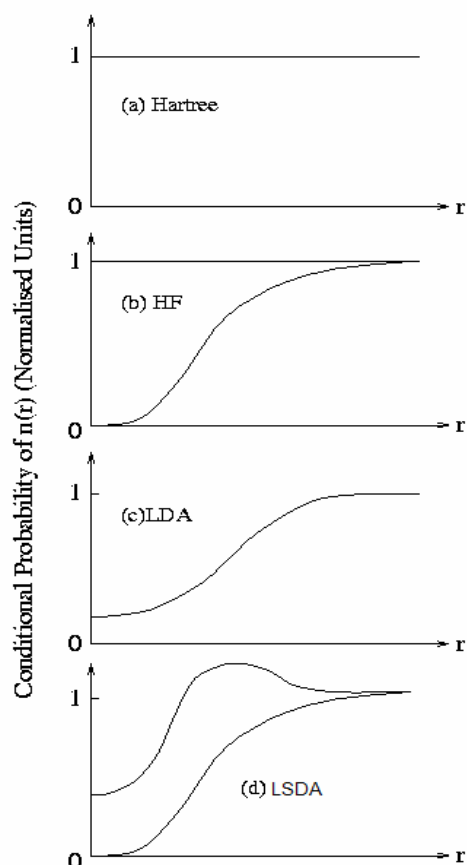


**Fig. 3.2:** Summary of the electron-electron interaction (excluding coulomb effects) in (a) the Hartree approximation, (b) the Hartree-Fock approximation, (c) the local density approximation and (d) the local spin density approximation which allows for different interactions for like-unlike spins.

## **3.4 Generalized Gradient Approximation (GGA)**

The local spin density (LSD) approximation has been the basis of electronic structure calculations in solid-state physics for many years [9]. This rough calculation may be written as:

$$E_{xc}^{LSD}(n_\uparrow, n_\downarrow) = \int d^3 r n(\vec{r}) \varepsilon_{xc}^{unif}[n_\uparrow(\vec{r}), n_\downarrow(\vec{r})] \tag{3.25}$$

$\varepsilon_{xc}^{unif}(n_\uparrow, n_\downarrow)$ exchange-correlation energy for each particle of a uniform electron gas [50]. The LSD exchange-correlation energies are inadequately negative (by about 10%) for almost all atoms, molecules, and solids. The LSD is a dependable, moderate-accuracy approximation. For many solid state objectives , the LSD level of precision is adequate, but LSD is not precise enough of most chemical applications, which need the determination of energy diversities with substantial accuracy. Hence the disinterest of the quantum chemistry community toward density functional techniques until recently [19]. New gradient-corrected functional of the form:

$$E_{xc}^{GGA}[n_\uparrow, n_\downarrow] = \int d^3 r \, f(n_\uparrow(\vec{r}), n_\downarrow(\vec{r}), \nabla n_\uparrow, \nabla n_\downarrow) \tag{3.26}$$

where *f* are functionals for different energies of the same system. These functionals may be partitioned into two wide categories : locally based functional, whose construction starts from the uniform electron gas, and "semi empirical" functional, which has one or more parameters fitted to a particular finite system, which have minimized LSD atomization energy errors by about a factor of 5 [20]. The generalized gradient approximation (GGA) has attracted much attention for its abstract simplicity and moderate computational workloads. At present, two GGA functional, one suggested by Becke and Perdew (BP)] and one suggested more recently by Perdew and Wang (PW), are the most popular ones in the literature [21].

Many calculations assessing the accuracy of the GGA have been reported and commonly demonstrate that the GGA substantially corrects the LDA error in the cohesive energies of molecules and solids [22]. Generalized gradient approximations (GGA s) to the exchange-correlation (XC) energy in density-functional theory, are at present receiving increasing attention as a straightforward substitute to improve over the local-density approximation (LDA) in ab initio total-energy calculations [18]. In a variety of fields, the GGA provided evidence to be more suitable than the LDA:

1. Binding energies of molecules and solids became more precise, correcting the trend of the LDA to over binding [24].

2. Activation energy obstacles, e.g., for the dissociate adsorption of $H_2$ on metal and semiconductor surfaces, are in distinctly better accordance with experiment. Reaction and activation energies for a variety of chemical reactions give the same enhancement [25].

3. The relative constancy of structural phases seems to be anticipated more realistically for magnetic and for nonmagnetic materials, too [26].

Bulk structural qualities are often not developed within the GGA. While the lattice parameters always rise in comparison with the LDA, a closer agreement with experimental data is reported for alkali metals, *3d* metals, and some *4d* metals. However, an overestimation of up to several percent is found for *5d* metals and common semiconductors, their bulk moduli accordingly turning out to be too small (typically by $\leq 25\%$) [27].

## 3.5 The full-potential linearized augmented-plane wave technique

The full-potential linearized augmented-plane wave (FP-LAPW) technique is well known to allow most precise calculation of the electronic structure and magnetic qualities of crystals and surfaces.

The application of atomic forces has greatly maximized its applicability, but it is still commonly supposed that FP-LAPW computations need considerable higher computational effort in comparison with the pseudopotential plane wave (PPW) based techniques [28].

FP-LAPW has recently showed important progress. For example, researchers habitually work out magnetism and nuclear quantities (for example, isomer shifts, hyperfine fields, electric field gradients, and core level shifts) [29]. Also, forces and molecular dynamics have been applied, and recent optimizations have decreased the CPU time of FP-LAPW calculations significantly [28]. Nevertheless, because the computational expense and memory requirements are still fairly high, FP-LAPW implementations are suitable only to fairly complicated systems.

One successful implementation of the FP-LAPW technique is the program package WIEN2K, a code enhanced by Blaha, Schwarz and coworkers [30]. It has been successfully implemented to a various scope of difficulties such as electric field gradients [31] and systems such as high-temperature superconductors, minerals [32], surfaces of transition metals [33], or antiferromagnetic oxides [34] and even molecules [35]. Reducing the total energy of a system by comforting the atomic counterparts for complicated systems became potential by the application of atomic forces, and even molecular dynamics became possible. So far the main disadvantage of the FP-LAPW-technique in comparison with the pseudopotential plane-wave (PPW) [36] method has been its higher computational expense. This may be largely because of an inconsistency in optimization efforts spent on both techniques, and so we have investigated the FP-LAPW technique from a computational arithmetical viewpoint.

Lately, the development of the Augmented Plane Wave (APW) techniques from Slater's APW, to LAPW and the new APW+lo was portrayed by Schwarz et al. [37]. One of the most precise techniques for performing electronic structure calculations for crystals is the full potential linearized augmented plane wave FP-LAPW technique.

It is based on the density functional theory for the handling of exchange and correlation and uses (for example, the local spin density approximation) (LSDA).

Effects, for valence states relativistic, can be incorporated either in a scalar relativistic handling or with the second dissimilarity technique including spin-orbit coupling. Core states are treated fully relativistically.

The FP-LAPW technique ,which is Like most ``energy-band techniques ,is a process for solving the Kohn-Sham equations for the ground state density, total energy, and (Kohn-Sham) eigen values (energy bands) of a many-electron system by presenting a basis set which is particularly modified to the problem.
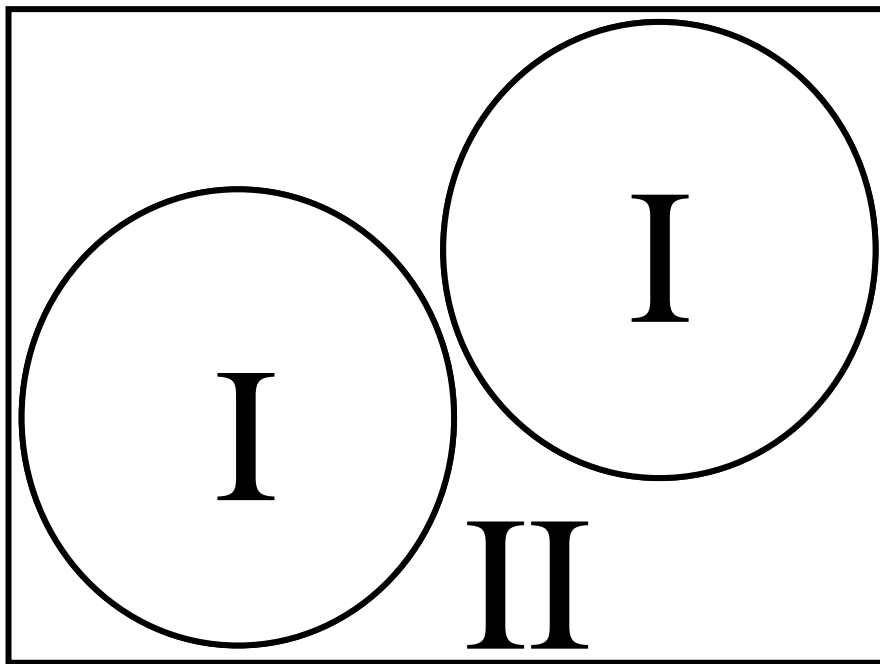


**Fig. 3.3:** Partitioning of the unit cell into atomic spheres (I) and an interstitial region (II).

This alteration is achieved by partitioning the unit cell into (I) nonoverlapping atomic circles (centered at the atomic sites) and (II) an interstitial region, that is to say, a region between two spaces. In the two sorts of regions diverse basis sets are used:

- Inside atomic sphere $I$ of radius $R_I$ a linear combination of radial functions times spherical harmonics $Y_{lm}(r)$ is used

$$\Phi_{kn} = \sum_{lm}[A_{lm}u_1(\vec{r}, E_l) + B_{lm}\dot{u}_1(\vec{r}, E_l)]\, Y_{lm}(\vec{r}) \qquad (3.27)$$

where $u_1(r, E_1)$ is the (at the origin) normal way out of the radial Schrodinger equation for energy $E_1$ and the spherical part of the potential inside sphere, $\dot{u}_l(r, E_l)$ is the energy derived of $u_1$ taken at the similar energy. A linear mixture of these two functions comprise the linearization of the radial function; the coefficients $A_{lm}$ and $B_{lm}$ are functions of $k_n$ decided by requiring that this root function $\dot{u}_l$ goes with the equivalent basis function of the interstitial region; $u_l$ and are achieved by numerical integration of the radial Schrodinger equation on a radial mesh inside the sphere.

- (II) in the interstitial zone a plane wave extension is applied

$$\Phi_{kn} = \frac{1}{\sqrt{w}}e^{iK_n r} \qquad (3.28)$$

where $K_n = k + k_n$, $k_n$ are the mutual lattice vectors and k is the wave vector inside the first Brillouin zone . Each plane wave is increased by an atomic-like function in every atomic sphere.

The solutions to the Kohn-Sham equations are extended in this joint basis set of LAPW's according to the linear dissimilarity technique

$$\Psi_k = \sum_n C_n \Phi k_n \qquad (3.29)$$

and the coefficients $C_n$ are decided by the Rayleigh-Ritz variation rule. The union of this basis set is controlled by a disconnected parameter $R_{mt}K_{max}$, where $R_{mt}$ is the smallest atomic sphere radius in the unit cell and $K_{max}$ is the magnitude of the largest $K$ vector.

Additional ($K_n$ independent) basis functions can be added to improve upon the linearization and to make possible a reliable treatment of semi core and valence states in one energy window. They are called "local orbitals" and consist of a linear combination of 2 radial functions at 2 dissimilar energies and one energy derivative:

$$\Phi_{lm}^{LO} = \left[A_{lm}u_l(\vec{r}, E_{1,l}) + B_{lm}\dot{u}_l(\vec{r}, E_{1,l}) + C_{lm}u_l(\vec{r}, E_{2,l})\right]Y_{lm}(\hat{r}) \tag{3.30}$$

The coefficients $A_{lm}$, $B_{lm}$, and $C_{lm}$, are decided by the necessities that $\Phi^{LO}$ should be regularized and has zero value and slope at the sphere border.

The FP- LAPW technique, in its general form, extends the potential in the following form

$$V(\vec{r}) = \begin{cases} \sum_{lm} V_{lm}(\vec{r})Y_{lm}(\hat{r}) & insidesphere \\ \sum_K V_K e^{ikr} & outsidesphere \end{cases}$$
(3.31)

And the charge densities analogously. Thus no form of rough calculations are made, a process often called the "full- potential" technique.

The "muffin-tin" rough calculation applied in early band calculations matches to keeping only the *L= 0* and *M=0* component in the initial idiom of final equation. and only the *K=0* constituent in the second. This process matches to take the spherical rate inside the spheres and the volume rate in the interstitial region. The entire energy is calculated according to Weinert *et al* [38]. The forces at the atoms are worked out according to Yu *et al* [39].

The Fermi energy and the weights of each band state can be worked out using an adapted tetrahedron (having four surfaces) technique [40].

# References

[1] http://en.wikipedia.org/wiki/DFT

[2] P. Hessler, N. T. Maitra, K. Burke , Journal of Chemical Physics. **117**, (2002) 72-81

[3] E. Runge, E. K. U. Gross, Physical. Review. Lett. **52**, (1984) 997

[4] O. J. Wacker, R. Kummel, E. K. U. Gross, Physical. Review. Lett. **73**, (1994) 2915

[5] http://www.physics.ohio-state.edu/~aulbur/dft.html

[6] P. Hohenberg, W. Kohn, Physical. Review. **136**, (1964) 864-871

[7] G. Vignale, Rasolt, Mark, Physical. Review. Lett. **59**, (1987) 2360-2363

[8] http:// chemistry.ncssm.edu/book/Chap9DFT

[9] W. Kohn and L. J. Sham, Physical. Review. **140**, (1965) 1133

[10] R. G. Parr and W. Yang, Density-Functional Theory of Atoms and Molecules. Oxford Science Publications, (1989) 145-147

[11] Richard M. Martin, Electronic Structure Basic Theory and Practical Methods. Cambridge University Press, (2004) 173

[12] http:// en.wikipedia.org/wiki/Density_functional_theory

[13] J. Dobson et al, Physical. Review. Lett **96**, (2006) 073201

[14] J. Tao and John P. Perdew, Physical. Review. Lett. **95**, (2005) 196403

[15] J. P. Perdew and A. Zunger, Physical. Review. B **23**, (1981) 5048

[16] D. M. Ceperley and B. J. Alder, Physical. Review. Lett. **45**, (1980) 566

[17] http:// cmt.dur.ac.uk/sjc/thesis/thesis/node13.html

[18] R. O. Jones and O. Gunnarsson, Rev. Mod. Phys. **61**, (1989) 689

[19] S. H. Vosko, L. Wilk, and M. Nusair, Can. J. Phys. **58**, (1980) 1200

[20] K. Burke, J. P. Perdew, and M. Levy, in Modern Density Functional Theory, J. M. Seminario and P. Politzer, Eds , Elsevier, Amsterdam (1995)

[21] A. D. Becke, Physical. Review. A **38**, (1988) 3098

[22] P. Bagno, O. Jepsen and O. Gunnarsson, Physical. Review. B **40**, (1989) 1997

[23] A. D. Becke, J. Chem. Phys. **97**, (1992) 9173

[24] D. Porezag and M. R. Pederson, J. Chem. Phys. **102**, (1995) 9345

[25] D. R. Hamann, Physical. Review. Lett. **76**, (1996) 660

[26] G. Ortiz, Physical. Review. B **45**, (1992) 328

[27] M. Petersen, F. Wagner, L. Hufnagel, M. Schffler, P. Blaha, and K. Schwarz. Computer Physics communications . **126**, (2000) 294-309

[28] D. J. Singh, Physical Review. B. **60**, (1999) 16359-16363

[29] P. Blaha, K. Schwarz, P. Sorantin, S.B. Trickey, Comput. Phys. Commun. **59**, (1990) 399

[30] P. Blaha, K. Schwarz, P. Herzig, Physical. Review. Lett. **54**, (1985) 1192

[31] B. Winkler, P. Blaha, K. Schwarz, Am. Mineralogist **81**, (1996) 545.

[32] B. Kohler, P. Ruggerone, S. Wilke, M. Scheffler, Physical. Review. Lett. **74**, (1995) 1387.

[33] X. G.Wang, W. Weiss, Sh.K. Shaikhutdinov, M. Ritter, M. Petersen, F. Wagner, R. Schlgl, M. Scheffler, Physical. Review. Lett. **81**, (1998) 1038

[34] M. Bockstedte, A. Kley, J. Neugebauer, M. Scheffler, Comp. Phys. Commun. **107**, (1997) 187

[35] K .Schwarz, P.Blaha and Madsen, G. K. H, Comp.Phys.Commun (2001)

[36] Weinert M., Wimmer E., and Freeman A. J, Physical. Review. B **26**, (1982) 4571

[37] Yu R., Singh D. and Krakauer H., Physical. Review. B **43**, (1991) 6411

[38] Bl chl P.E., Jepsen O. and Andersen O.K., Physical. Review. B **49**, (1994) 16223

[39] Omar Mahmood PhD thesis, An-Najah National University, Nablus, Palestine, (2008)

[40] Haneen Yousef, PhD thesis, An-Najah- National University, Nablus, Palestine, (2009)

# Part IV

# Investigation of Strain Effects on Some Physical Properties of PdVTe half Heusler alloy

# 4. Investigation of Strain Effects on the Physical Properties of PdVTe Alloy

## 4.1 Introduction

$\int\!\!\!\int$ erromagnetism and the half metallic behavior of the half Heusler compounds have been an active field of experimental and theoretical researches, due to their frequently promising novel properties and their technological applications since their first discovery in 1903 by Fritz Heusler [1]. Groot found that some of these compounds were ferromagnetic, although none of its basic constituents show magnetic behavior by themselves [2,3]. It is noticeable that most of their physical properties can be predicted easily by counting the number of their valence electrons [3,4]. The objective of recent investigation related to half-Heusler compounds is to study ferromagnetic alloys revealing the magnetic field induced super-elasticity, large strain-induced changes in the magnetization, and magnetic shape memory effect [4–8].

One sub-class of more than 200 Heusler alloys have semiconductor behavior [9]. They are the most suitable choice for the spintronic applications and the green energy related fields, such as thermoelectrics or solar cells. Remarkably, their band gaps can easily be changed from 0 to 4 eV by modifying their chemical composition. Half Heusler alloys are usually depicted by a generic formula XYZ [10-17], where X and Y are transition metal elements and Z stand for s-p elements.

Their physical properties are related to the nature of elements X, Y and Z, where the compounds XYZ can be characterized by ferromagnetism, antiferromagnetism, semiconductivity, and optical properties [18,19].

These properties are sensitive to phase change, temperature and pressure [20]. They are good candidates for use in optoelectronic [21], topological insulator [22], photovoltaic, thermoelectric [23] and spintronic [24] devices. Therefore, Gokhan Surucu et *al.* [25] have investigated theoretically the structural, electronic, magnetic and lattice dynamical properties for XCoBi (X: Ti, Zr, Hf) Half-Heusler compounds. They concluded that γ-XCoBi compounds have suitable electronic characteristic for flexible electronics. Another theoretical study suggests that physical properties of PdCoX (X = Si and Ge) and XRhSb (X : Ti and Zr) half-Heusler compounds depend on the different atomic arrangements which are called α, β and γ phases [26,27].

The investigation of the structural, electronic, elastic and mechanical properties of ZrNiPb half-Heusler alloy under pressure reveals that the investigated compound is a favorable thermoelectric material [28].

In order to contribute to this active area of research, we have investigated the strain effects on the magnetism, structure, electronic, elasticity, thermodynamic, optical properties and the half metallic behavior of PdVTe alloy by the use of the most accurate methods to electronic band structure, i.e. ab initio density functional theory calculations DFT [8].

At the stoichiometric composition, PdVTe alloy crystallizes in $C1_b$ structure. As shown in Fig. 1, the atoms Pd, V and Te take the positions (0, 0, 0), (1/4, 1/4, 1/4) and (3/4, 3/4, 3/4), respectively. The symmetry of its $C1_b$ crystal structure, total number of valence electrons and the large swap splitting of the d state of Pd and V elements due to the strong hybridization led to the half-metallic ferromagnetic features of this alloy.

This behavior is very similar to those of YCrSb and YMnSb [29], they display metallic behavior in spin up and semiconducting behavior in the spin down.

The computational value of total magnetic moment for this compound ($3\mu_B$) is in line with the Slater–Pauling rule $\mu_{tot} = Z_t$ -18, which is usually applied to a several compounds [30]. The local magnetic moment of V atom dominants the total magnetic moment of this compound, whereas the local magnetic moments of Pd and Te are negligible.

The calculated elastic constants, using the stress-strain approach [31], show that PdVTe compound is mechanically stable. Furthermore, the study of Poisson's ratio $\nu$ supports the ionic character of this compound. The obtained values of Pugh's ratio *B/G* and Cauchy pressure ($C_{12}$-$C_{44}$) demonstrate that this compound is brittle and PdVTe is stiffer than NaMgAl and RhMnSb compounds [32,33].

The optical properties including imaginary and real parts of complex dielectric function, refractive index, reflectivity, and absorption coefficient are predicted for first time. Imaginary part of dielectric function reveals that the PdVTe alloy is optically metallic. The calculated values are in line with the Penn model [34-35].

We have investigated the thermodynamic properties using the quasi-harmonic Debye model and we have obtained the dependence on temperature and pressure of numerous parameters including the thermal heat capacities $C_V$ and $C_p$, expansion coefficient $\alpha$, bulk modulus, Debye temperature $\theta$ and Grüneisen constant $\gamma$. The calculated variations of the thermodynamic parameters are in line with the results obtained by the Debye theory applied to several materials.

The phonon dispersion curves, the density of states, and the formation energies are calculated to investigate the dynamical stability.

Finally, the investigation of strain effects on the physical properties reveals that the this compound preserves its ferromagnetic half-metallic behavior, remains mechanically stable, the optical and thermodynamic properties keep the same features and the ionic nature dominates the atomic bonding in the large range of pressure.

## 4.2 Computational Details

Calculations concerning magnetism, structure, elasticity, electronic and optical properties are carried out within a state of the full-potential linearized augmented plane wave plus a local orbital (FP-LAPW + lo) approach as performed in the WIEN2k code based on DFT theory [8,11]. To include an exchange correlation potential, GGA-PBE and LDA are adopted [12-13].

We have applied Koelling and Harmon approach to integrate the relativistic effects on the computations,.as shown in Figs.1 and 2, the convergence test led to the value of cut off parameter RMT, Kmax = 8.0, l=10 and 3000 k-points are sufficient to obtain the energy precision of $10^{-6}$ Ry/formula unit. The values of radius RMT are 2.32, 2.26 and 2.32 for Pd, V and Te, respectively.

Optimization of the volume ($V_0$), equilibrium lattice constant ($a_0$) and energy ($E_0$) is performed using the Murnaghan method [14].

The "stress-strain" approach is used to predict the independent elastic constants $C_{ij}$ and to study the elastic behavior of the PdVTe compound [15]. While PdVTe alloy crystallizes in C1$_b$ structure the Born's stability criteria's are applied as shown in the equation (1) [16].

$$C_{11} + 2C_{12} > 0, \ C_{11} - C_{12} > 0, \ C_{44} > 0 \tag{1}$$
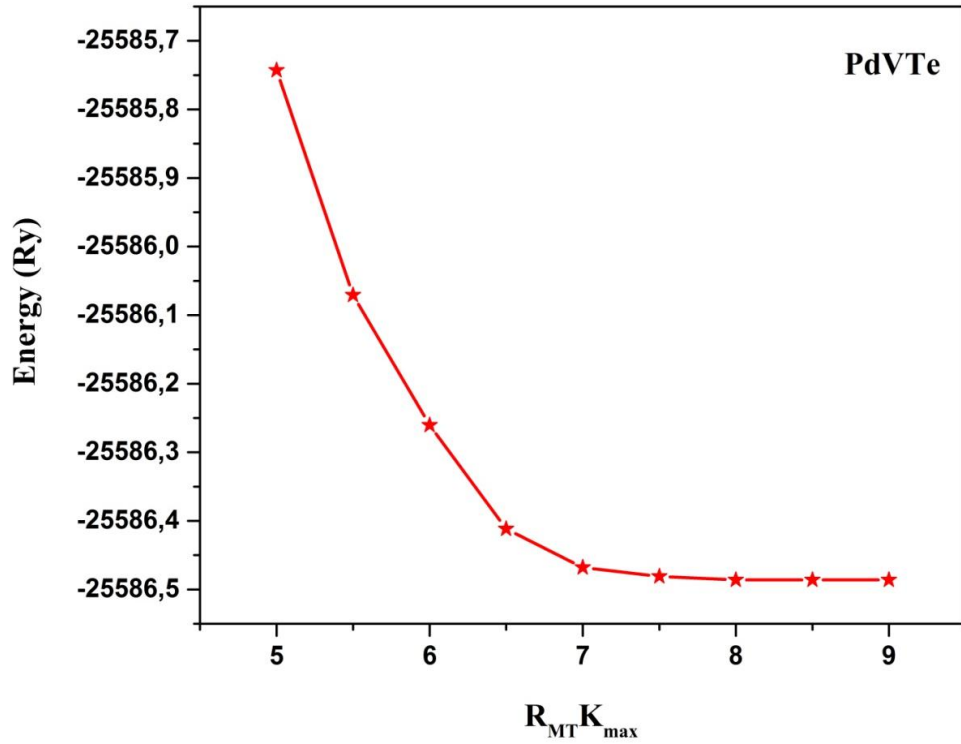
**Fig. 4.1:** Total energy as a function of $R_{MT}K_{max}$
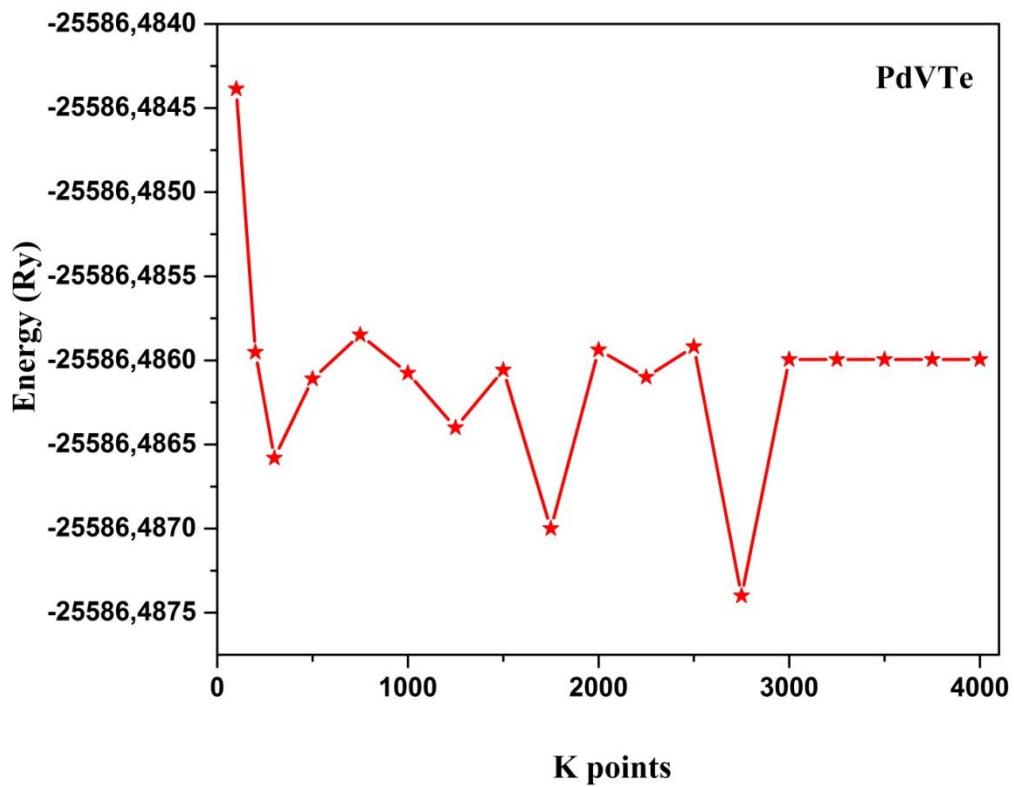


**Fig. 4.2:** Total energy as a function of K points

The adiabatic bulk modulus $B$, Poisson's ratio $v$, shear modulus $G$, Young's modulus $E$ and anisotropy factor $A$ are predicted using the Voigt-Reuss-Hill (VRH) approximation [17] :

$$B = \frac{C_{11} + 2C_{12}}{3} \tag{2}$$

$$G = \frac{1}{2}\left[\left(\frac{5(C_{11} - C_{12})C_{44}}{4C_{44} + 3(C_{11} - C_{12})}\right) + \left(\frac{C_{11} - C_{12} + 3C_{44}}{5}\right)\right] \tag{3}$$

$$v = \frac{3B - 2G}{2(3B + G)} \tag{4}$$

$$E = \frac{9BG}{3B + G} \tag{5}$$

$$A = \frac{2C_{44}}{C_{11} - C_{12}} \tag{6}$$

The optical properties are deducted from the calculated parameters given by the complex dielectric function $\varepsilon\,(\omega)$ using the Ehrenreich and Cohen's equation [18]:

$$\varepsilon\,(\omega) = \varepsilon_1(\omega) + i\varepsilon_2\,(\omega) \tag{7}$$

The real and the imaginary parts are carried out by the use of Kramers–Kronig approach [18]:

$$\varepsilon_1(\omega) = 1 + \frac{2}{\pi}P\int_0^\infty \frac{\omega'\varepsilon_2(\omega')}{\omega'^2 - \omega^2}d\omega' \tag{8}$$

$$\varepsilon_2(\omega) = \frac{8}{2\pi\omega^2}\sum_{nn'}\int_{BZ}|P_{nn'}(k)|^2 \tag{9}$$

Where $k$ is the wave vector in irreducible Brillouin zone and $P_{if}$ is the momentum matrix elements.

The refractive index $n(\omega)$ is derived from the complex dielectric function [19]

$$n(\omega) = \frac{1}{\sqrt{2}}\left(\varepsilon_1 + (\varepsilon_1{}^2 + \varepsilon_2{}^2)^{1/2}\right)^{1/2} \tag{10}$$

The reflectivity ($R$) describes the quantity of phonons reflected from the incident solids given by the equation [20]:

$$R(\omega) = \left| \frac{\sqrt{\varepsilon(\omega)} - 1}{\sqrt{\varepsilon(\omega)} + 1} \right|^2 \tag{11}$$

The thermodynamic properties are predicted using the quasi-harmonic Debye model realized in the Gibbs program. In this model, the thermodynamic parameters are described in the following form [21]:

$$B(P,T) = V \left( \frac{\partial^2 G^*(V; P, T)}{\partial V^2} \right) \tag{12}$$

$$C_V = 3nk_B \left[ 4D \left( \frac{\theta}{T} \right) - \frac{3\theta/T}{e^{\theta/T} - 1} \right] \tag{13}$$

$$C_P = C_V(1 + \alpha\gamma T) \tag{14}$$

$$\alpha = \frac{\gamma C_V}{BV} \tag{15}$$

$$\gamma = -\frac{dln\theta(V)}{dlnV} \tag{16}$$

### 4.3 Results and discussion

#### 4.3.1 Magnetism, electronic, and half metallic behavior

Structural optimization of PdVTe half-Heusler alloy was used to predict its ground state. Three cases were considered (paramagnetic (PM), antiferromagnetic (AFM) and ferromagnetic (FM) phases).

The variations of the total energies as function of the volume reported in Fig.3, reveal that the ferromagnetic phase has lowest energy as compared with the paramagnetic and antiferromagnetic phases, that is to say, the ferromagnetic phase is more stable, thus PdVTe is ferromagnetic half Heusler alloy [27,36-39].
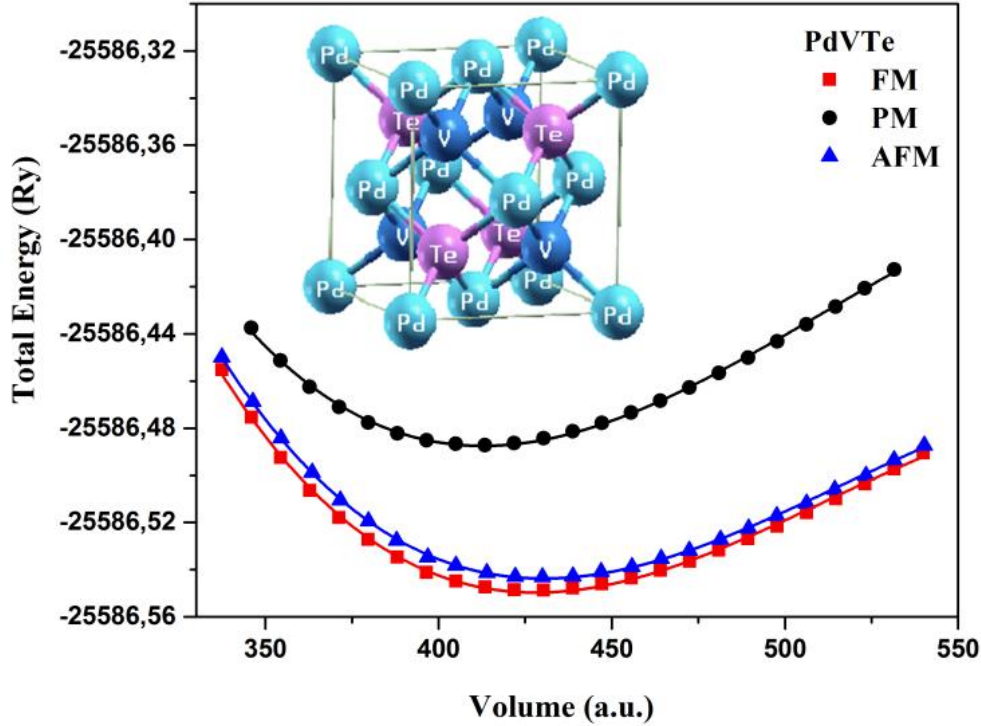
**Fig. 4.3:** Total energy as a function of the volume per formula unit for the ferromagnetic (FM), antiferromagnetic (AFM) and paramagnetic (PM) states of PdVTe alloy. Inset is the corresponding crystal structure

The optimized values obtained using the Murnaghan approach for volume ($V_0$), equilibrium lattice constant ($a_0$) and energy ($E_0$) predicted for the ferromagnetic phase using GGA and LDA approaches are shown in table 1. Obviously, the computed lattice constant ($a_0$) is about 6.3284 Å as predicted by GGA, while that predicted by LDA is lower as expected at 6.1599 Å. At the same time, bulk modulus B values are about 161.24 GPa (GGA) and 161.14 GPa (LDA).

**Table 1:** Predicted equilibrium lattice constant $a_0$, energy $E_0$, volume $V_0$ at the ferromagnetic phase

| PdVTe | $a_0/\text{Å}$ | $E_0/\text{eV}$ | $V_0/\text{a.u}^3$ |
|-------|------|--------------|-----------|
| GGA | 6.3284 | - 348122.8515 | 427.5823 |
| LDA | 6.1599 | -347789.7684 | 419.1820 |

The Curie point, or Curie temperature ($T_C$), is defined as the temperature above which some materials lose their permanent magnetic properties, which can be replaced by induced magnetism [38]. This important parameter may be predicted from mean field approximation [39] using obtained ground state energy difference ($\Delta E$) between ferromagnetic and antiferromagnetic phase as given in Eq. 17:

$$T_c = \frac{2}{3K_B}\Delta E \tag{17}$$

The computed Curie temperature $T_C$ is about the room temperature (298 K), thus the magnetic properties of PdVTe alloy is not be suppressed. Therefore, PdVTe alloy is suitable for spintronic applications. The obtained Curie temperature $T_C$ is highest than that of NaVTe (150 K) compound [40].

The predicted band structures for minority and majority spin channels in the ferromagnetic phase are illustrated in Fig.4 for PdVTe Alloy. It is evident that the minority spin electrons show an indirect band gap, between the $\Gamma$ point of the valence band and the X point for the conduction band, about 0.51eV (GGA) around the Fermi level, which reveals its semiconducting nature, furthermore the majority spin channels display metallic character. These features are very similar to those of CoMnTe and RuMnTe and demonstrate that these alloys are ferromagnetic half-metallic [41].

As is well known, the local spin density approximation (LDA) in density functional theory (DFT) always underestimate the band gaps of solids due to the lack of derivative discontinuity [42]. The Band gap within LDA is 0.49eV.
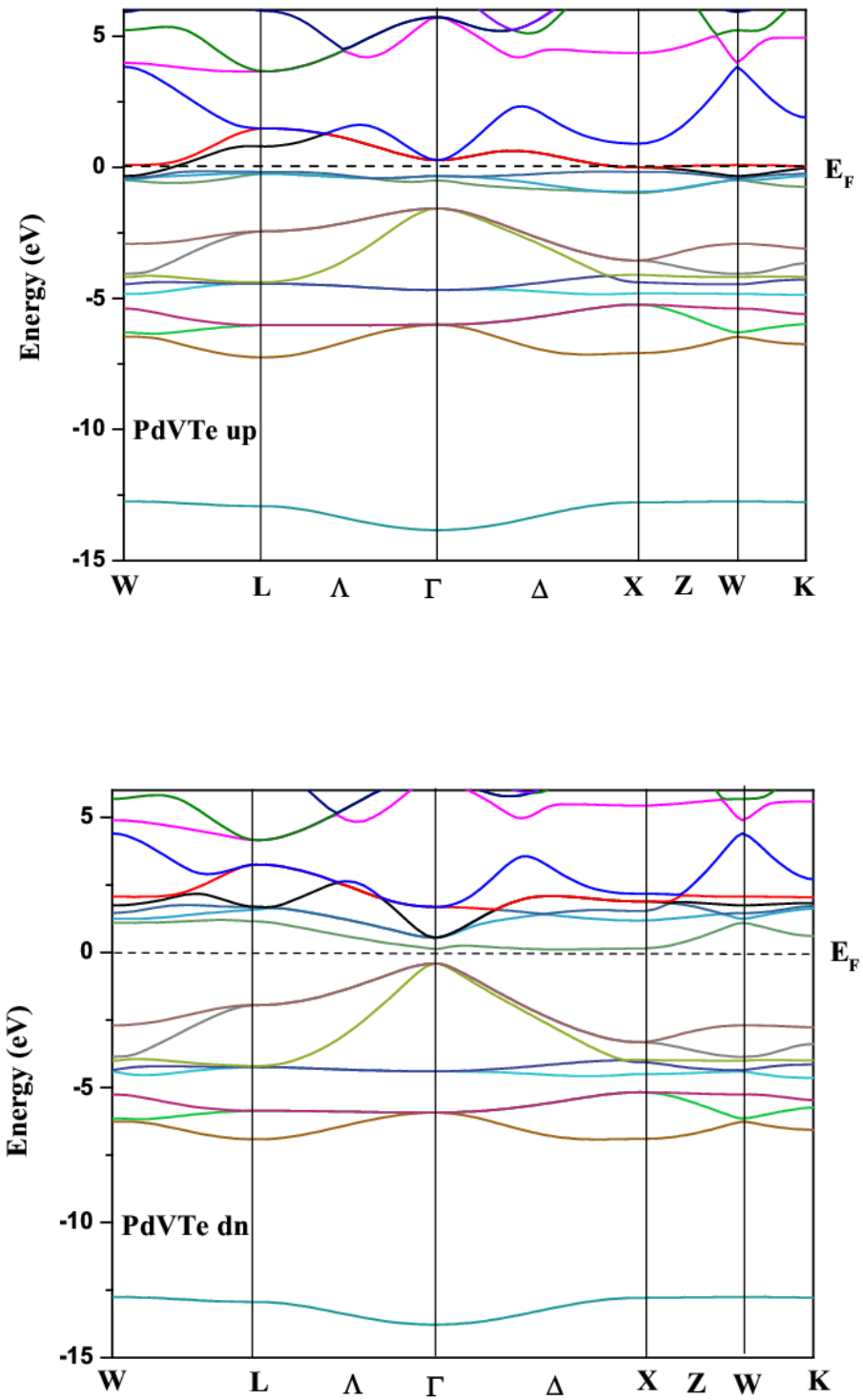
**Fig. 4.4:** Electronic band structure for majority and minority spin electrons of PdVTe alloy

To better understand the origin of the indirect band gap in the minority spin channels and the attitude of electronic states, partial and total densities of states are estimated. The results are shown in Fig.5 for the PdVTe alloy, the calculated total and partial densities of states for the minority spin electrons are represented by the negative values. We can remark that the total density of states around the half-metallic gap is largely dominated by the (d) states of the lower valent transition metal (V) atom, where the main peaks are about 3.73 and -4.49 states/eV situated approximately at -0.64 and 2.07 eV, respectively. Whereas, the main peaks of d states for Pd element are 5.42 and -6.25 states/eV located about -4.41 and -4.25eV, respectively. The influences of the (s) and (p) states are negligible around the half metallic gap, and their contributions are positioned chiefly in the lowest zones of the total density of states around -5.89 eV for (p) states and -12.81 eV for (s) states; furthermore, the main peaks in total density of states around the Fermi level maintain the same positions as in the local densities of states. Obviously, the total density of states for PdVTe alloy is the superposition of the contributions of each local density of states. The Fermi level is represented by the vertical dashed line in the densities of states DOS presented in Fig.5.

Noticeably, the behaviors of the calculated densities of states are comparable to those of CoCrSi compound, though the band gap is narrow 0.66 eV for CoCrSi [32]. We illustrate in the Fig.6(a) the predicted band gaps of minority spin channels of some of Te-based half Heusler XYTe alloys. It is remarkable that the highest value of the half metallic gap is about 1.4 eV for MnTiTe. The half-metallicity of PdVTe alloy is mainly the consequence of the symmetry of its $C1_b$ crystal structure and the strong hybridization between the d states of V atom and the d states of Pd atom [43].

Consequently, the compound PdVTe exhibits semiconducting behavior in the spin down bands with a band gap $E_g$ around the Fermi level $E_F$ and metallic nature in the spin up bands. Tellure (Te) with (s) and (p) states determines some of the physical properties and the structural stability of this alloy [44].
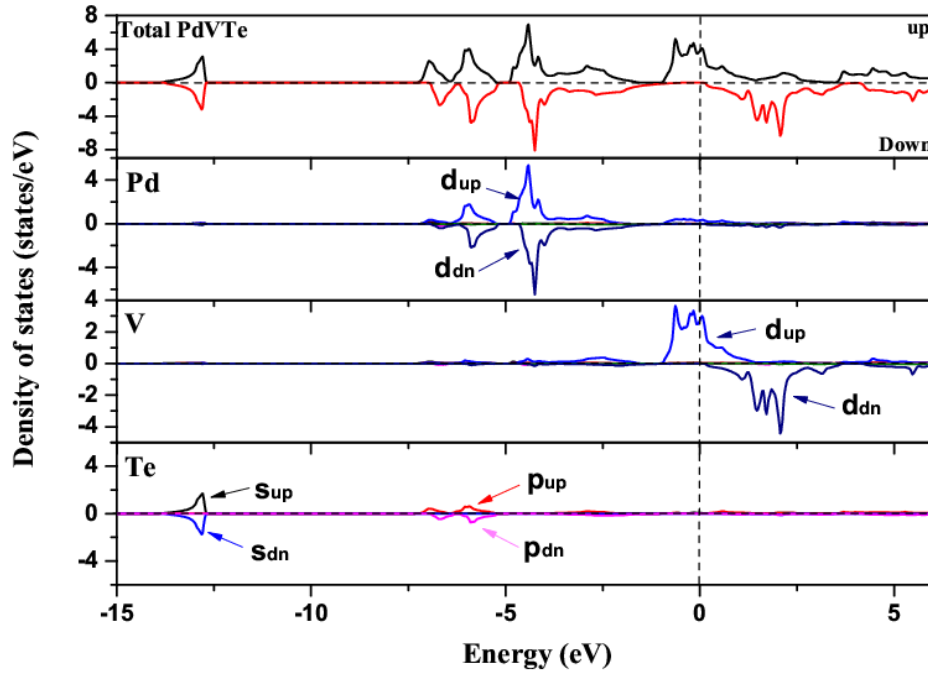


**Fig. 4.5:** Calculated spin-projected total and partial DOS plot for PdVTe alloy

The calculated total magnetic moments $\mu_{tot}$ within GGA and LDA are almost same and are 3 $\mu_B$, which nicely follows the Slater–Pauling rule,i.e. $\mu_{tot} = Z_t$ -18 [45]. It is noticeable that the local magnetic moment of V site is higher as compared to those of Pd and Te as shown in table 2. In fact, the total magnetic moment of all alloy counting Mn and V elements each has a big value as presented in Fig. 6(b). Till now, there have been no experimental values on total and local magnetic moments available to compare with our results.
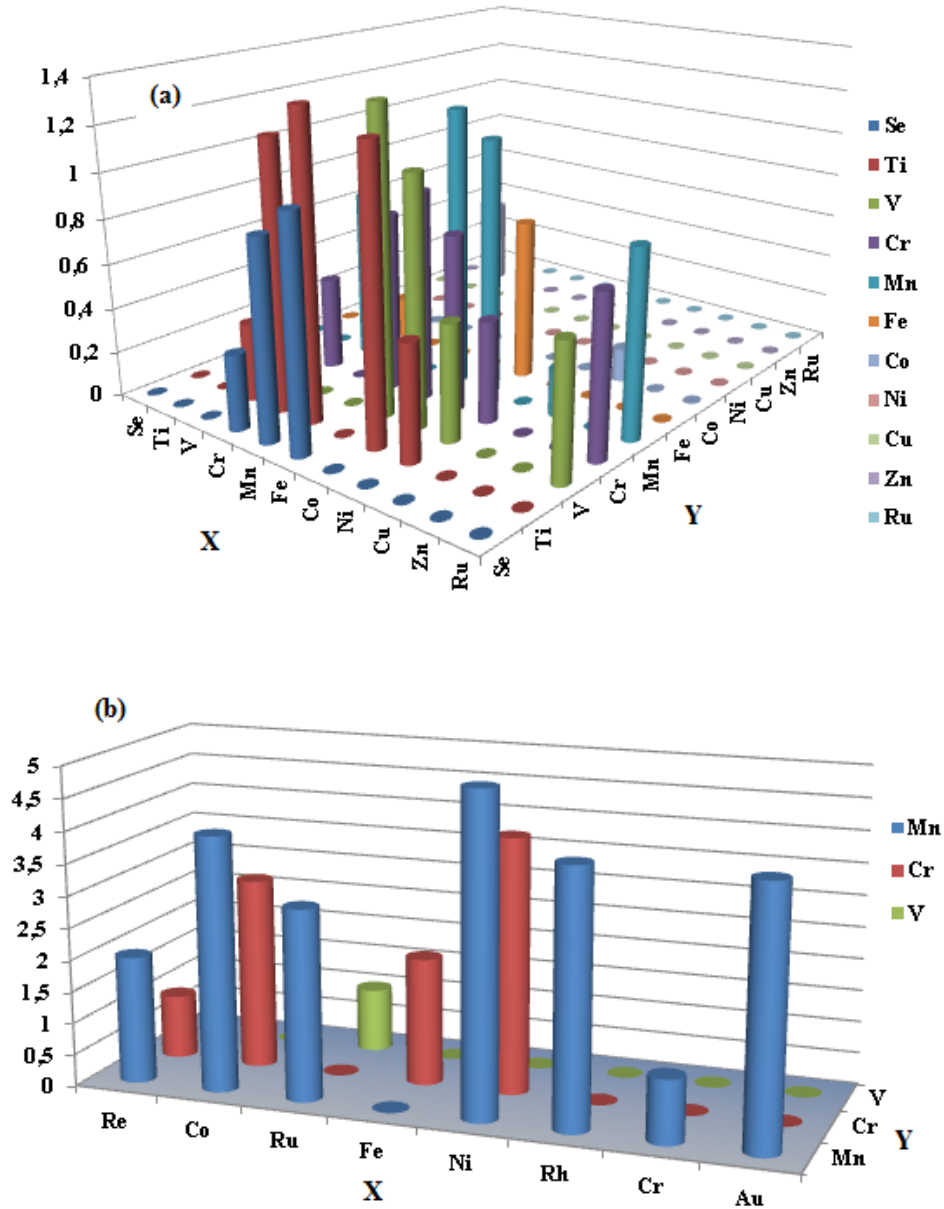
**Fig. 4.6:** (a) Calculated band gaps of minority spin channel, (b) total magnetic moments of Te-based half-Heusler XYTe alloys

**Table 2:** Calculated local and total magnetic moments of PdVTe alloy

| compound | Local magnetic moment ($\mu_B$) | | | | Total ($\mu_B$) |
|---|---|---|---|---|---|
| | Pd | V | Te | int | |
| PdVTe | 0.02768 | 2.60148 | -0.05081 | 0.42225 | 3.00060 |
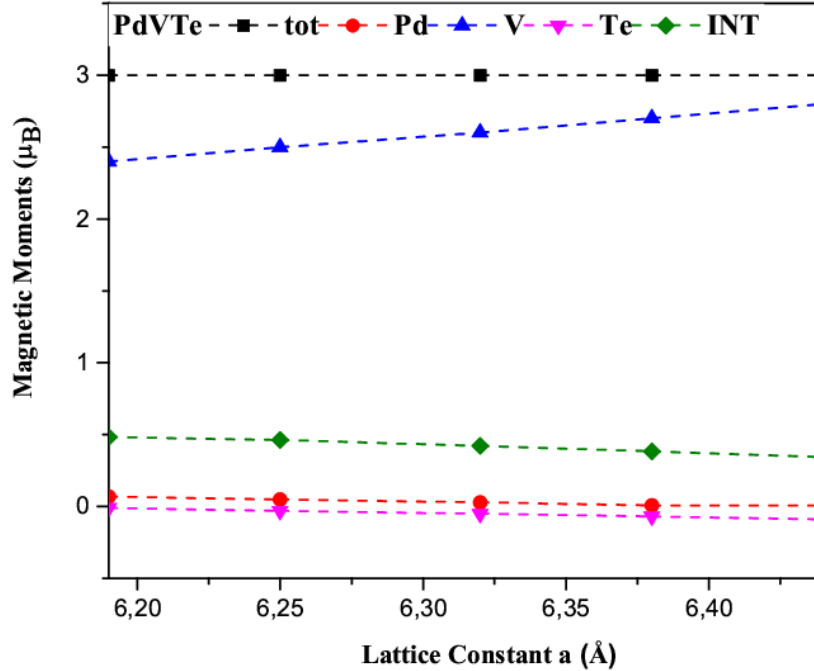
**Fig. 4.7:** Lattice constant dependences of the total and local magnetic moments for PdVTe alloy

In order to examine the strain effects on the magnetism and half metallic behavior of the PdVTe alloy, we have investigated the variation of the local and total magnetic moments as function of the lattice constant under pressure up to 30 GPa. From Fig.7, it is noticeable that during the contraction of the unit cell volume the interactions between Pd and V elements increase; therefore, the V local moment decreases, whereas the local magnetic moment of the Pd increases. However, PdVTe total magnetic moment is kept the same as $3\mu_B$ per unit cell in the interval [6.1Å, 6.45Å].

To verify the ability of this material to maintain its half metallic character under the effect of uniform strain, the half metallic gap variations as function of the lattice constant in a large interval were studied.

We have found that PdVTe alloy conserves its half-metallic feature in the interval of [6Å, 6.5Å], whereas outside this interval, the contraction and the expansion destroy this behavior.

As, the expansion moves the Fermi level $E_F$ downwards and contraction moves it upwards in energy, the Fermi level will eventually be in the conduction band or in the valence band, namely, the half metallic alloy becomes purely metallic. Visibly, PdVTe compound is less robust as compared to RuVTe, which maintains its feature in a large interval of pressure [5.8Å, 6.6Å] because of its big half metallic band gap ($E_g$=0.89 eV). The exceptional magnetic and half metallic properties of PdVTe qualify it as promising functional alloy in the spintronic field such as magnetic tunnel junctions, spin-transfer torque devices, spin valves and giant-magnetoresistance.

## 4.3.2 Elastic properties

To finalize the compound for an engineering product or technological application, it is imperative to recognize its elastic properties. The elastic parameters give important ideas about the nature of the bonding forces in solids and provide information about the materials responses to mechanical strength, pressure, and even phase transition. The elastic properties play a significant role in several technological applications, such as load deflection, thermoelastic stress, internal strain, sound velocities, phase transformation and fracture toughness. Using the "stress–strain" method, the independent elastic constants $C_{ij}$ are evaluated. $C_{11}$ characterizes the elasticity in length, although $C_{44}$ and $C_{12}$ represent the elasticity in shape. While PdVTe is cubic compound, to verify the stability of lattice, we utilize the Born's stability criteria's as shown in the equation (1).

The independent elastic parameters for PdVTe alloy are listed in table 3. Our calculated values show that this compound is mechanically stable. The predicted value of the elastic parameter $C_{11}$ is 225.78 GPa, thus, PdVTe displays more resistance for unidirectional compression than RuVTe ($C_{11}$=161.25 GPa) and LiMgAl ($C_{11}$=32.074 GPa) [32].

**Table 3:** Predicted elastic constants $C_{ij}$ (GPa), bulk modulus $B$ (GPa), shear modulus $G$ (GPa), Pugh's ratio $B/G$, Poisson's ratio $v$, Young's modulus $E$ (GPa) and anisotropy factor $A$.

|  | $C_{11}$ | $C_{12}$ | $C_{44}$ | $B$ | $G$ | $B/G$ | $v$ | $E$ | $A$ |
|---|---|---|---|---|---|---|---|---|---|
| PdVTe | 225.78 | 129.10 | 148.36 | 161.32 | 95.76 | 1.68 | 0.25 | 239.82 | 3.07 |

The bulk modulus $B$ measures the material's resistance to applied pressure. The calculated Bulk modulus value from Murnaghan's equation of state is 161.24 GPa, , which is very close to the value calculated from "stress–strain" method using Eq. (12) (161.32 GPa). The similarity between the two values estimates the accuracy of our elastic calculations. The larger the value of bulk modulus is, the stronger the capacity of the resist deformation is [47]. The large bulk modulus value of PdVTe alloy reveals that it has the strong resistance to volume change by applied pressure.

The shear modulus $G$ is a measure of resist reversible deformation. It is well known that, the larger the value of $G$ is, the stronger the capacity of the resist shear deformation is. The computed value reveals that PdVTe has the largest value as compared to CoCrTe. Hence, the deformation resistant capacity of PdVTe would be much stronger than that of CoCrTe [32].

Poisson's ratio parameter $\nu$ supplies idea about natures of the forces operating in the solids. Our calculated value of Poisson's ratio $\nu$ is about 0.25, which proves that the atomic bondings are dominated by ionic forces. On the other hand, the predicted value of *G/B* is 0.6, which also supports the ionic character of this compound [32]. According to the Pugh's ratio *B/G* and Cauchy pressure ($C_{12}$-$C_{44}$) values we can envisage the ductility or brittleness of the compound. The predicted value of Cauchy pressure ($C_{12}$-$C_{44}$) for PdVTe is negative; thus, this compound is brittle. Also, the calculated value of Pugh's ratio *B/G* for PdVTe (1.68) is less than 1.75 which besides characterized this compound as brittle material [33]. In order to investigate the anisotropy of PdVTe compound, we have calculated the elastic anisotropy parameter *A*. The compound is described as absolutely isotropic when *A* value is equal to 1. The estimated value of elastic anisotropy *A* for PdVTe is about 3.07. The Young's modulus *E* gives idea about the stiffness of the compounds. The matter is stiffer when the Young's modulus value is high. The Young's modulus calculated value is 239.82 GPa. Therefore, PdVTe is stiffer than NaMgAl and RhMnSb compounds [32,33].

The pressure dependence of the elastic parameters is very important for the characterization of the materials. The elastic parameters $C_{ij}$, *B, G, E, A, $\nu$ and G/B* under varying pressure up to 30 GPa by step of 5 GPa, are computed and presented in Fig. 8. Obviously, $C_{11}$ and $C_{12}$ increase at increased pressure values while $C_{44}$ decreases. Therefore, the bulk modulus and Poisson's ratio increase linearly with the pressure, although, the shear modulus, the Young's modulus, the anisotropy factor and the G/B ratio decrease.

The critical value that separates ductile and brittle materials is about 0.6. Fig. 8 reveals that the G/B ratio is smaller than 0.57, therefore, PdVTe remains ductile in the considered interval of pressure.



**Fig. 4.8:** Calculated elastic parameters (*Cij*, *B*, *G*, *E*, *A*,*ν*, *G/B*) of PdVTe under pressure up to 30 GPa.

The pressure dependence of the elastic parameters is very important for the characterization of the materials. The elastic parameters $C_{ij}$, *B, G, E, A*, *ν* *and G/B* under varying pressure up to 30 GPa by step of 5 GPa, are computed and presented in Fig. 8. Obviously, $C_{11}$ and $C_{12}$ increase at increased pressure values while $C_{44}$ decreases. Therefore, the bulk modulus and Poisson's ratio increase linearly with the pressure, although, the shear modulus, the Young's modulus, the anisotropy factor and the G/B ratio decrease.

The critical value that separates ductile and brittle materials is about 0.6. Fig. 8 reveals that the G/B ratio is smaller than 0.57, therefore, PdVTe remains ductile in the considered interval of pressure.
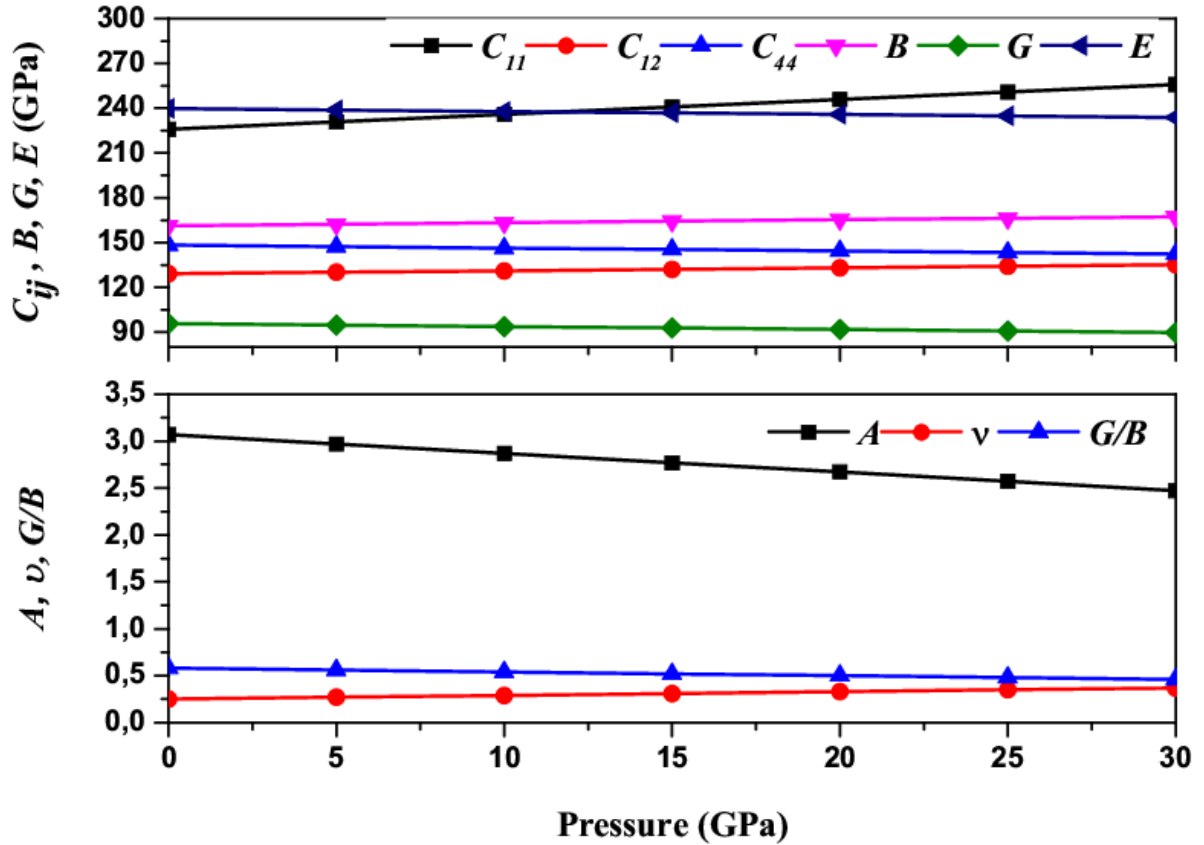
### 4.3.3  Optical properties

The optical properties of matter supply huge information on various aspects of its physical properties, such as the phenomena relating to the presence of impurities and defects and their nature; and give an important idea on vibrational and electronic states. The optical properties of mater play a vital role in several technological applications such as optical instruments counting the light emitting diodes (LED) designed for the photovoltaic cells and lighting, and diode lasers used in the heads of CD and DVD devices.

In order to investigate the optical properties, several optical parameters including imaginary and real parts of complex dielectric function, refractive index, reflectivity, and absorption coefficient are predicted for first time.

We illustrate the calculated imaginary and real parts of the dielectric function in the Fig.9. Obviously, study of the imaginary part of dielectric function $\varepsilon_2(\omega)$ proves that our investigated alloy is optically metallic, due to the high values of $\varepsilon_2(\omega)$ for both pressures 0GPa ($\varepsilon_2(0)=15.03$)  and 10GPa ($\varepsilon_2(0)=26.32$). Transitions of electrons from (p) state of the Te element in valence band to the (d) states of the Pd and V elements inside conduction band generate the high energy peaks observed in the spectra of the imaginary part of dielectric function $\varepsilon_2(\omega)$. At small energies, peaks are extremely low as compared to those close to zero energy, which demonstrate the high degree of optical conductivity at low frequencies.
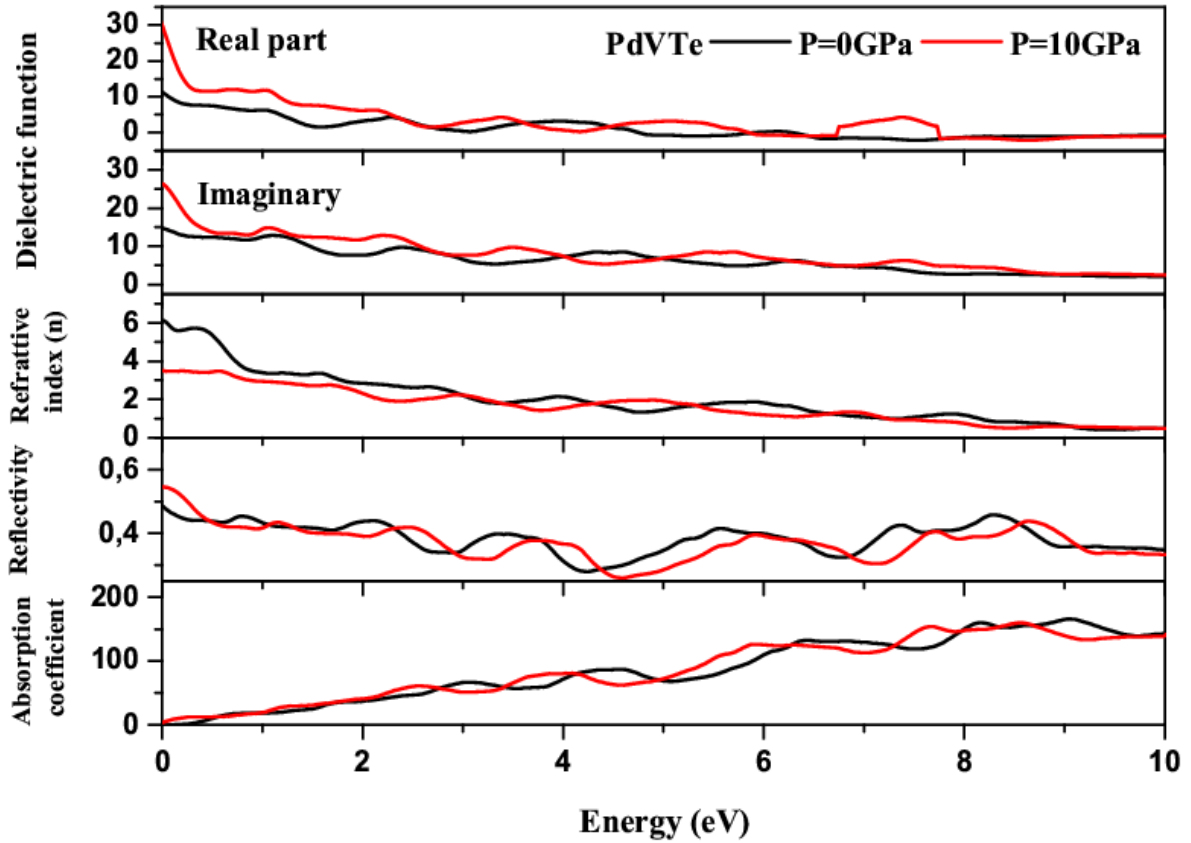
**Fig. 4.9:** Dielectric function, Refractive index, Reflectivity and Absorption coefficient as a function of the energy at various pressures for the PdVTe alloy

From the Fig.9, it is clear that the highest values of real part of dielectric function $\varepsilon_1(\omega)$ for both pressures 0GPa and 10GPa are 11.16 and 31.14 respectively, at zero frequency. The value at 10 GPa is higher than for 0GPa due to decrease of the band gap, the calculated values are in line with the Penn model [46], which suggests inverse relationship between real part of dielectric function $\varepsilon_1(\omega)$ at zero frequency and band gap *Eg*.

The negative values of $\varepsilon_1(\omega)$ in interval [4.75eV,10eV] of energy correspond to the completely attenuation of incident light (photons).

Refractive index is a significant parameter for photoelectric technology, which describes how fast photons pass through the solids. From the Fig.9, the nonlinear behaviour of the refractive index is shown by the presence of peaks in the infrared region. The inter-band transition from the highest valence band to the lowest conduction band generates different peaks in the interval [0,10eV]. The main values are located in the zero frequency for both pressures 0GPa and 10GPa, and slowly diminish in the visible zone reaching approximately zero value.

Reflectivity exposed in Fig.9 illustrates highest values at zero frequency for both pressure 0GPa and 10GPa due to the metallic feature of our studied alloy shown previously in the investigation of the imaginary part. Reflectivity variations decrease from 0.48 and 0.55 for 0GPa and 10GPa respectively to approximately 0.3 at 5eV, and became more important with high peak of 0.45 at approximately 9eV. In the interval of energies where the real part $\varepsilon_1(\omega)$ turn into a negative values, the peaks rise higher, which reveals that the reflectivity of PdVTe is more important to the incident light (photons) in this range of energy.

Absorption coefficient shown in Fig.9 describes how solids take up a light's energy and transforms it to the internal energy. It is obvious that the threshold point is very close to 0 eV due to the small band gap of PdVTe alloy. High peaks are located in the visible region for both pressure 0 GPa and 10 GPa, this peaks describe the greater capability in absorbing light. Highest peaks are located in the visible region because of the transitions between the closely split levels of energy. The features of the absorption variations for both pressures are similar. Our predicted optical results are summarized in table 4.

**Table 4:** Calculated real part of complex dielectric function $\varepsilon_1(0)$, optical band gap (*EOG*), refractive index $n(0)$ and reflectivity $R(0)$ for PdVTe half Heusler alloy.

| PdVTe | $\varepsilon_1(0)$ | $E_{OG}$ | $n(0)$ | $R(0)$ |
|---|---|---|---|---|
| P= 0 GPa | 11.16 | 15.03 | 3.56 | 0.54 |
| P= 10 GPa | 31.14 | 26.32 | 6.21 | 0.57 |

### 4.3.4 Thermodynamic Properties

The thermodynamic parameters supply much more information and detail about the material's specific behaviors under ruthless constraints, such as high pressure or high temperature; therefore, we investigate the thermodynamic properties, by applying the quasi-harmonic Debye model to the half-Heusler PdVTe compound [29], we predict the thermal expansion $\alpha$, specific heats capacity at constant pressure ($C_P$) and constant volume ($C_V$), bulk modulus, Debye temperature ($\theta$) and Grüneisen parameter ($\gamma$) in the temperature range from 0 to 1000K by step of 100K under a series of pressure values from 0 to 30 GPa by step of 10 GPa.

Heat capacity is a significant parameter for the matter thermodynamic properties, defined as the quantity of heat to be furnished to a given mass of a matter to generate a unit change in its temperature. Generally, heat capacity provides large information about the transition of phase and lattice vibration.
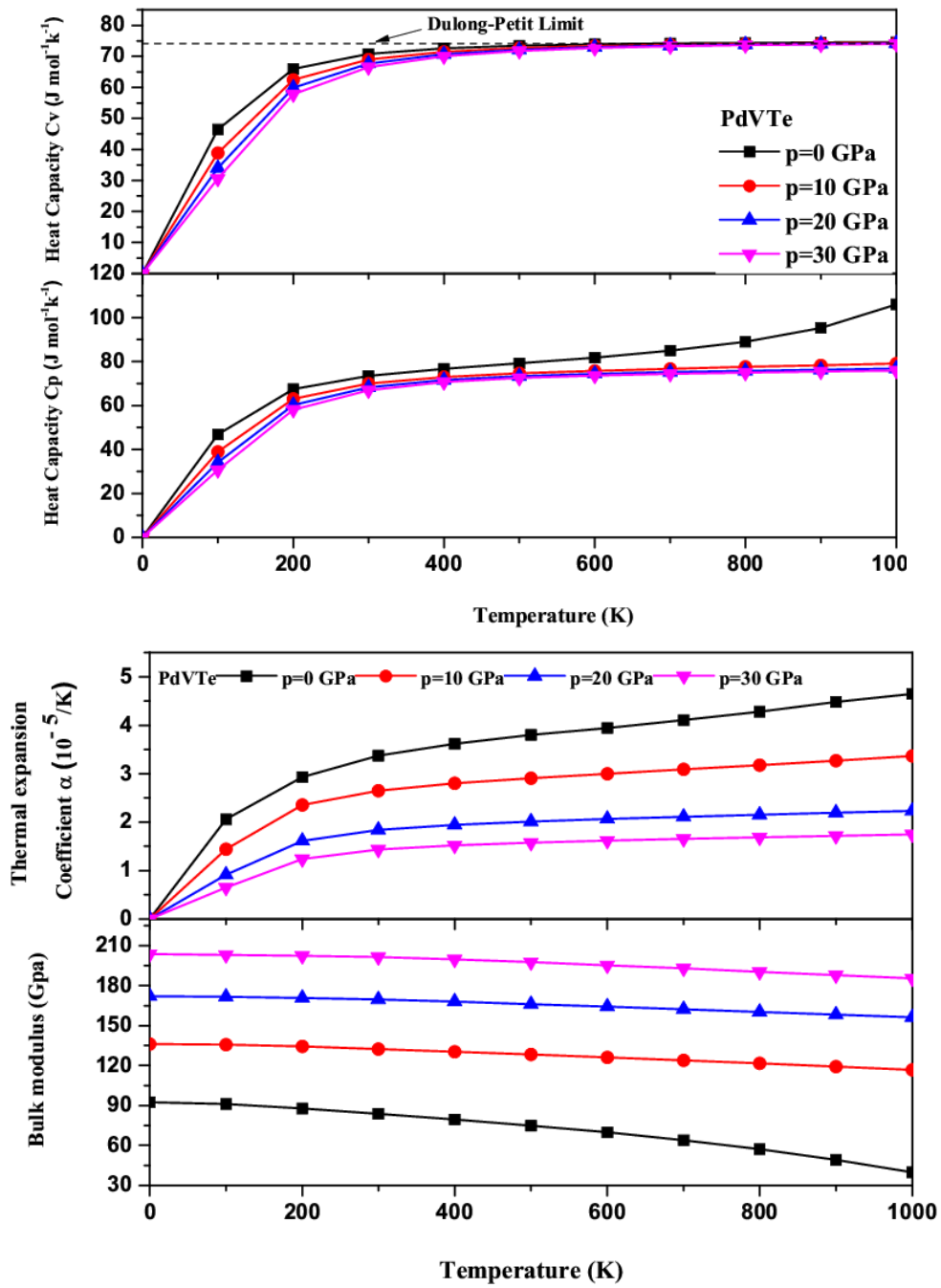
**Fig. 4.10:** Variations of specific heat capacity ($C_v$, $C_p$), thermal expansion $\alpha$ and bulk modulus with temperature at various pressures for PdVTe alloy

Fig. 10 displays the variations of the specific heat capacity at constant volume $C_V$ and at constant pressure $C_P$ as a function of temperature and pressure for the half-Heusler PdVTe compound. It is clear that the temperature has a very strong effect on the $C_V$ and $C_P$ at the low temperature approximately from 0 to 300 K, they are very close together because of the sharp increase of $C_V$ and $C_P$, due to the anharmonic approximation of the Debye model at lower temperature used in the calculations, whereas, at high temperatures, this anharmonic effect is suppressed and $C_V$ turns into a linear increase and saturates quickly to the Dulong-Petit limit, which proves that thermal energy excites all the possible phonon mode, and is frequent to all solids at high temperatures [29].

Although for $C_P$, the values increase monotonically with the temperature. Moreover, the pressure has reverse effect, i.e., both specific heat capacities at constant pressure $C_P$ and at constant volume $C_V$ decrease with increasing pressure. At null pressure and 300 K, the $C_V$ and $C_P$ for the investigated compound are equal to 70.47 JMol$^{-1}$ K$^{-1}$ and 73.31 JMol$^{-1}$ K$^{-1}$, respectively.

The thermal expansion parameter α has both practical and theoretical importance, it is crucial to describe the tendency of material to change its volume, shape, and area in response to a change in temperature at a constant pressure and also it is important to estimate the thermodynamic equation of state.

The calculated values of the thermal expansion parameter $\alpha$ as function of temperature and pressure are displayed in Fig.10. It is obvious that the thermal expansion $\alpha$ increases markedly with temperature from 0 to 1000 K; furthermore, the variation of $\alpha$ increases sharply with temperature lower than 300 K. This phenomenon is because the anharmonic effect of the Debye model at lower temperature, this feature is strongly depressed at high temperature, whereas, for temperature higher than 300 K, the variation of the thermal expansion $\alpha$ increases slowly and increasingly turns into a linear increase. On another side, it is remarkable that, for a given temperature, the values of $\alpha$ decrease continuously with pressure increase, which reveal that high pressure suppresses $\alpha$. At null pressure and 300 K, the calculated value of the thermal expansion $\alpha$ for the studied PdVTe compound is about $3.34\times10^{-5}\mathrm{K}^{-1}$.

We have used the quasi harmonic Debye's approximation to investigate the variation of bulk modulus with respect to temperature and pressure. The plot of Bulk modulus $B$ is significant as it alone can show the pressure and temperature features of elastic constants and also that of other moduli of elasticity. Fig.8 shows that the bulk modulus $B$ decreases at the constant pressure while temperature increases, which reveals that the elastic constants $Cij$ will also decrease with the increase of temperature. Therefore, all of the moduli of elasticity decreases as temperature increases at constant pressure. This feature leads to an important property of PdVTe half Heusler alloy. It reveals the high temperature working interval of this alloy, which is a most important condition for several technological applications like superconductivity and thermoelectricity [30]. On the other hand, the bulk modulus increases at the constant temperature as pressure increases, thereby indicating the increase of elastic constants and consequently the other moduli of elasticity.

The variation of Bulk modulus with respect to pressure at constant temperature shows the disadvantages of the investigated alloy at high pressure ranges. The melting point and the boiling point of PdVTe alloy also increases as pressure increases. This character makes this alloy a poor candidate for a number of applications such as soldering applications and optical applications.
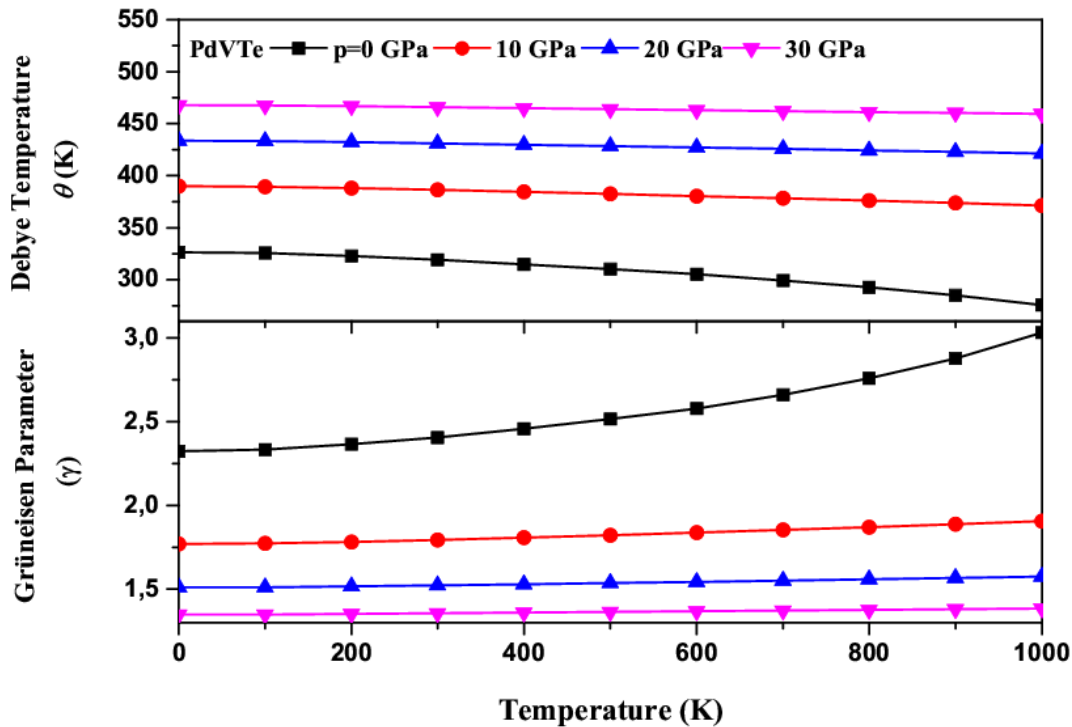


**Fig. 4.11:** Variations of Debye Temperature $\theta$(K) and Grüneisen Parameter with temperature at various pressures for PdVTe alloy

The Grüneisen parameter $\gamma$ is of great significance because it appears in several main thermodynamic relations. $\gamma$ interprets the consequence that changing the volume of a crystal lattice has on its vibrational properties, and, so, the consequence that temperature change has on the dynamics and size of the crystal lattice. The variations of Grüneisen parameter $\gamma$ are shown in Fig.11. It is noticeable that the Grüneisen parameter decreases with pressure increase, when temperature is kept constant.

However, at the constant pressure, the Grüneisen parameter continuously increases as temperature increases, but its variation rate is strongly suppressed by higher pressure. The predicted value of γ of PdVTe compound at zero pressure and 300 K is 2.40.

The Debye temperature is physical parameter, which provides information about physical properties of matter, such as thermal conductivity, electric conductivity, specific heat and broadening. It is defined as the highest temperature that can be achieved due to a single normal vibration. From the Fig.11, it is obvious that the Debye temperature $\theta$ smoothly decreases as temperature increases, when the pressure is kept constant. At low range of temperature from 0 to 300 K, there is a small variation. Whereas, the decreasing rate of Debye temperature becomes stronger at high temperature, while, the variation rate is larger at lower pressure. Nevertheless, at constant temperature, the Debye temperature continuously increases with increasing pressure. The calculated value of the Debye temperature $\theta$ of the studied compound at zero pressure and 300 K is 319.09 K.

### 4.3.5 Dynamical stability

The investigation of phonons is a significant part of condensed matter physics. They play essential roles in thermal properties and dynamical behaviors.

Computations of phonon dispersion curves in high symmetry lines of the B.Z and phonon density of states are performed for PdVTe alloy employing the finite displacement approach, implemented in the Phonopy code [47], using a supercell of size 2x2x2 of primitive lattice type with 24 atoms.

The obtained results of phonon dispersion curves are illustrated in Fig.12(a). Obviously, there are no imaginary modes, and all the phonon modes have positive frequencies, this result reveals that PdVTe alloy is dynamically stable. Nine vibrational modes (3 acoustic and 6 optical modes) appear due to the presence of three atoms in the primitive unit cell of PdVTe alloy. At ($\Gamma$) point, the frequencies of optical modes are 84.62 cm$^{-1}$ (degenerated) and 118.17 cm$^{-1}$ (degenerated). The phonon dispersion curves are divided into two distinct regions with a narrow gap of about 8.2 cm$^{-1}$. The low frequency band region from 0 to 96.3 cm$^{-1}$ contains three optical and three acoustic branches. Whereas, the high frequency band region from 106 to 137cm$^{-1}$ is formed by the remaining three optical phonon branches. The maximum frequency of acoustic modes is 74.61 cm$^{-1}$ and the minimum frequency of optical modes is 69.45 cm$^{-1}$. Noticeably, there is no phonon gap between optical and acoustic branches, indicating a strong acoustic-optical phonon scattering which will suppress the lattice thermal conductivity. Fig. 10(b) illustrates the total and partial phonon density of states of PdVTe alloy which reveals that the phonon density of states in the acoustic region is mostly contributed by the vibration of V atom. Whereas, Pd atom exhibits its largest contribution in the highest optical phonon branches. The highest peak of the total phonon density of states is located at 70.31cm$^{-1}$.

In order to examine the possible experimental formation of PdVTe alloy, we predict its formation energy $E_F$ with the following expression [48]:

$$E_F = E_{total} - (E_b(Pd) + E_b(V) + E_b(Te)) \qquad (18)$$

where $E_b$ is the energy per atom and $E_t$ is the total energy of primitive cell. The estimated $E_F$ of PdVTe alloy is $-0.987$ (eV/atom).

This negative value signifies that the synthesis of the investigated compound is energetically favourable, and consequently it can be easily experimentally fabricated.
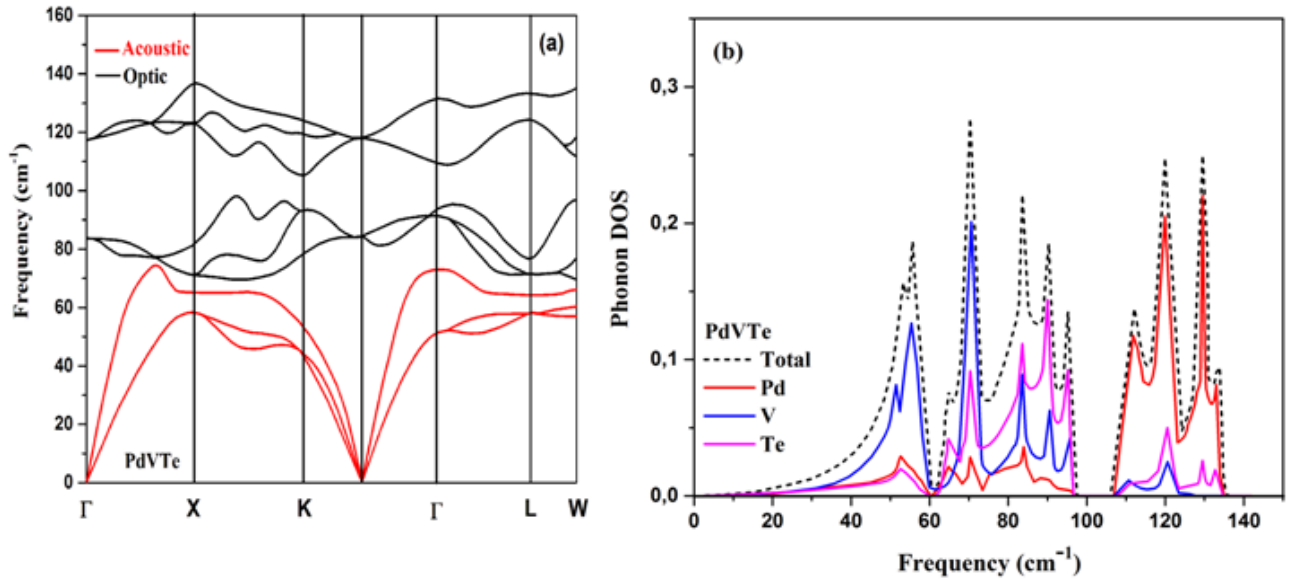


**Fig. 4.12**: Partial and total phonon density of states in PdVTe alloy.

The thermal conductivity ($\lambda$) is the most important parameter for the thermoelectric applications. Cahill, Clarke and Long [49] models are used to predict the minimum thermal conductivity value $\lambda_{min}$ and the diffusion thermal conductivity $\lambda_{diff}$ is given by Synder [49] model.

The obtained results of $\lambda_{min}$ are 0.291, 0.264 and 0.223 w/mk predicted by Cahill, Clarke and Long, respectively, whereas, $\lambda_{diff}$ is about 0.172 w/mk. The computed thermal conductivities of PdVTe are smaller than those of $Tl_4Ag_{18}Te_{11}$ compound [49].

### 4.3.6 Conclusions

We have investigated the strain effects on the magnetism, elasticity, electronic, thermodynamic and optical properties of the PdVTe half-Heusler alloy applying the (FP-LAPW + lo) approach implemented by WIEN2K simulation code. The calculated value of equilibrium lattice constant demonstrates that PdVTe alloy is stable in $C1_b$ structure. The study of the electronic properties reveals the Half-metallic behavior with a small indirect band gap $E_g$ of 0.51 eV around the Fermi level for the minority spin channels. The predicted value of total magnetic moment $\mu_{tot}$ is $3\mu_B$ per unit cell, nicely follows the Slater–Pauling rule $\mu_{tot} = Z_t -$ 18. The imaginary and real parts of complex dielectric function, refractive index, reflectivity, and absorption coefficient are predicted for first time, and they are in line with the Penn model. Imaginary part of dielectric function reveals that the PdVTe alloy is optically metallic. The thermodynamic properties are investigated using the quasi-harmonic Debye model, the calculated variations are in line with the results obtained by the Debye theory. The dynamical stability is confirmed by the calculated phonon dispersion curves, the density of states, and the formation. Finally, the analysis of the strain effects reveals that the PdVTe alloy maintains the ferromagnetic half metallic feature in a large interval of pressure, the studied compound remains mechanically stable, the ionic nature dominates the atomic bonding, and the electronic, thermodynamic and optical properties keep the same features in the investigated pressure interval. The exceptional magnetism, elasticity, half metallicity, electronic, thermodynamic and optical properties of PdVTe qualify it as promising functional alloy in the spintronic and optoelectronic fields.

# References

[1] F. Heusler. Verh. Dtsch. Phys. Ges. 5, 217 (1903)

[2] R. A. de Groot, F. M. Mueller, P. G. van Engen, K. H. J. Buschow. Appl. Phys. 55, 2151 (1984)

[3] I. Zutic, J. Fabian, S. D. Sarma. Rev. Mod. Phys. 76, 323 (2004)

[4] R. A. de Groot, F. M. Müller, P. G. van Engen. Phys. Rev. Lett. 50, 2024 (1983)

[5] Heusler Alloys: Properties, Growth, Applications; Springer Series in Materials Science; Springer Verlag: Dordrecht, The Netherlands; Heidelberg, Germany; New York, NY, USA; London, UK. 222 (2016)

[6] T. Graf, F. Casper, J. Winterlik, B. Balke, G. H. Fecher, C. Felser. Anorg. Allg. Chem. 635, 976 (2009)

[7] Spintronics: From Materials to Devices; Springer Verlag: Dordrecht, The Netherlands; Heidelberg, Germany; New York, NY, USA; London, UK. (2013)

[8] D. J. Singh, and L. Nordstrom, Planewaves, Pseudopotentials, and the LAPW Method. Springer Science & Business Media (2006)

[9] F. Casper, T. Graf, S. Chadov, B. Balke and C. Felser. Semicond. Sci. Technol. 27, 063001 (2012)

[10] Zhao Peng Hao, Ran Liu, Yi Hang Fan, Li Li Wang, Journal of Alloys and Compounds. 820, 153118 (2020),

[11] P. Blaha, K. Schwarz, G. K. H. Madsen, D. Kvasnicka and J. Luitz, WIEN2k, An Augmented Plane Wave + Local Orbitals Program for Calculating Crystal Properties, Karlheinz Schwarz Technical University, Wien (2001)

[12] Z. Wu and R. E. Cohen. Phys. Rev. B. 73, 235116 (2006)

[13] J. P. Perdew, K. Burke, M. Ernzerhof. Phys. Rev. Lett. 77, 3865 (1996)

[14] F. D. Murnaghan, The Compressibility of Media Under Extreme Pressures. Proceedings of the National Academy of Sciences of the United States of America. 30 (9), 244 (1944)

[15] A. Reuss, Z. Angew. Math. Mech. 9, 49 (1929)

[16] J. Wang, J. Li, S. Yip, S. Phillpot, D. Wolf. Phys. Rev. B 52, 12627 (1995)

[17] G. V. Sin'ko, N. A. Smirnov. J. Phys. Condens. Matter. 14, 6989 (2002)

[18] M. Shakil, Sharjeel Hassan, Hafsa Arshad, M. Rizwan, S. S. A. Gillani, M . Rafique, M. Zafar, Shabbir Ahmed, Physica B: Condensed Matter. 575, 411677 (2019)

[19] Rinku Majumder, Md. Moazzem Hossain and Dipali Shen, Modern Physics Letters B. 33, 1950378 (2019)

[20] Besbes Anissa, Djelti Radouan, Bestani Benaouda, International Journal of Modern Physics B, 33 1950247 (2019)

[21] David Kieven, Reiner Klenk, Shahab Naghavi, Claudia Felser, and Thomas Gruhn, Phys. Rev. B 81, 075208 (2010)

[22] Shi-Yuan Lin, Ming Chen, Xiao-Bao Yang, Yu-Jun Zhao, Shu-Chun Wu, Claudia Felser, and Binghai Yan, Phys. Rev. B 91, 094107 (2015)

[23] Peeyush Kumar Kamlesh, Ruchita Gautam, Sarita Kumari,  Ajay Singh Verma, Physica B: Condensed Matter. 615, 412536 (2021)

[24] L. Damewood, B. Busemeyer, M. Shaughnessy, C. Y. Fong,1 L. H. Yang, and C. Felser, Physical Review. B 91, 064409 (2015)

[25] Gokhan Surucu, Mehmet Isik, Abdullah Candan, Xiaotian Wang, Hasan Huseyin Gullu,  Physica B: Condensed Matter. 587, 412146 (2020)

[26]  Aytaç Erkisi, Gokhan Surucu and Recai Ellialtioglu, Philosophical Magazine. 97(26), 2237 (2017)

[27]    Gokhan    Surucu, Abdullah    Candan, Aytaç    Erkisi, Ayşenur Gencer and Hasan Hüseyin Güllü, Mater. Res. Express. 6(10), 106315 (2019)

[28] M. I. Babalola, B. I. Adetunji, B. E. Iyorzor and A. Yaya, International Journal of Modern Physics B. 32, 1850248 (2018)

[29] M. Atif Sattar, Muhammad Rashid, M. Raza Hashmi, S. A. Ahmad, Muhammad Imran, Fayyaz Hussain, Chin. Phys. B. 25(10), 107402 (2016)

[30] A. Kılıç, N. Kervan, S. Kervan. J. Supercond. Nov. Magn. 28, 1767 (2015)

[31] C. Çoban, Y. Ö. Çiftçi, K. Çolakoğlu, Indian Journal of Physics. 90(11), 1233 (2016)

[32] A. Afaq, Abu Bakar, M. Rizwan, M. Aftab Fareed and H. Bushra Munir, Modern Physics Letters B. 33(8), 1950093 (2019)

[33] Iltaf Muhammad, Jian-Min Zhang, Anwar Ali, Majeed Ur Rehman, Shafiq Muhammad, Materials Chemistry and Physics. 251, 123110 (2020)

[34] N. Mehmood, R. Ahmad. J. Supercond Nov. Magn. 31, 233 (2018)

[35] N. Mehmood, R. Ahmed, G. Murtaza. J. supercond. Nov. Mag. 30, 2481 (2017)

[36] Aytac Erkisi and Gokhan Surucu, Mater. Res. Express. 4, 066504 (2017)

[37] Qi Wang, Qianheng Du, Cedomir Petrovic, Hechang Lei, Chin. Phys. Lett. 37, (2) 027502 (2020)

[38] Aytac Erkisi, Bugra Yildiz, Xiaotian Wang, Mehmet Isik, Yusuf Ozcan, Gokhan Surucu, Journal of Magnetism and Magnetic Materials. 519, 167482 (2021)

[39] Gokhan Surucu, Bugra Yildiz, Aytac Erkisi, Xiaotian Wang, Ozge Surucu, Journal of Alloys and Compounds. 838, 155436 (2020)

[40] Muhammad Atif Sattar, S. Aftab Ahmad, Fayyaz Hussain, Claudio Cazorla, Journal of Materiomics. 5(3), 404 (2019)

[41] T. Djaafri, A. Djaafri, A. Elias, G. Murtaza, R. Khenata, R. Ahmed, S. Bin Omran, D. Rached. Chin. Phys. B. 23(8), 087103 (2014)

[42] D. P. Rai, Sandeep, A. Shankar, Anup Pradhan Sakhya, T. P. Sinha, R. Khenata, M. P. Ghimire and R. K. Thapa, Mater. Res. Express. 3, 075022 (2016)

[43] I. Galanakis, P. H. Dederichs, N. Papanikolaou. Phys. Rev. B 66, 134428 (2002)

[44] T. Djaafri, A. Djaafri, F. Saadaoui. J. supercond. Nov. Magn. 31, 2449 (2018)

[45] I. Galanakis, P. H. Dederichs, N. Papanikolaou. Phys. Rev. B 174429, 66 (2002)

[46] D. R. Penn. Phys. Rev. 128(5), 2093 (1962)

[47] A. Togo, I. Tanaka, Scripta Materialia. 108, 1 (2015)

[48] X. Wang, Z. Cheng, G. Liu, X. Dai, A. Bouhemadou, IUCrJ. 4, 758 (2017)

[49] Aysenur Gencer, Ozge Surucu, Gokhan Surucu, Engin Deligoz, Journal of Solid State Chemistry. 289, 121469 (2020)

# Part V

# General Conclusion

# 5 General Conclusion

Within the framework of this thesis, firstly we have reported the description of the Full Heuster and half Heuslet alloys and the difference between them in the point of view of the physical properties and the field of the technological applications. Secondly, we have illustrated the density functional theory (DFT). Finally, In the First-principles DFT studies related to PdVTe are performed. Our studies confirm that this compound is half-metallic ferromagnetic material. It is found that this materials behave as metals for the majority spin bands and exhibit semiconducting characteristics for minority spin bands. Origin of the band gap is traced out in the strong hybridization between the d states of higher valent TM atoms and lower valent TM atoms. The role of the elements containing sp states is crucial in tuning several physical properties of half Heusler compounds and structural stability of $C1_b$ compounds. Our calculated value of total magnetic moment $\mu_{tot}$ is $3\mu B$ per unit cell, and most of the part is contributed from V atom. The total spin moment scale is accurately in agreement with total number of valence electrons contained by the atoms of these compounds. The calculated value of $\mu_{tot}$ is in the line with the rule of $\mu_{tot} = Zt$ -18. The effect of the unit cell volume is found to be decisive for the magnetic properties and the half-metallicity characteristics. The imaginary and real parts of complex dielectric function, refractive index, reflectivity, and absorption coefficient are predicted for first time, and they are in line with the Penn model. Imaginary part of dielectric function reveals that the PdVTe alloy is optically metallic. The thermodynamic properties are investigated using the quasi-harmonic Debye model, the calculated variations are in line with the results obtained by the Debye theory. The dynamical stability is confirmed by the calculated phonon dispersion curves, the density of states, and the formation. Finally, the analysis of the strain effects reveals that the PdVTe alloy maintains the ferromagnetic half metallic feature in a large interval of pressure, the studied compound remains mechanically stable, the ionic nature dominates the atomic bonding, and the electronic, thermodynamic and optical properties keep the

same features in the investigated pressure interval. The exceptional magnetism, elasticity, half metallicity, electronic, thermodynamic and optical properties of PdVTe qualify it as promising functional alloy in the spintronic and optoelectronic fields.

**Canadian Science Publishing**

# ARTICLE

# Ab initio investigation of strain effects on the physical properties of PdVTe alloy

Khodja Djamila, Djaafri Tayeb, Djaafri Abdelkader, Bendjedid Aicha, Hamada Khelifa, and Marbouh Norredine

**Abstract:** The investigations of the strain effects on magnetism, elasticity, electronic, optical, and thermodynamic properties of PdVTe half-Heusler alloy are carried out using the most accurate methods to obtain electronic band structure (i.e., the full-potential linearized augmented plane wave plus a local orbital (FP-LAPW + lo) approach). The analysis of the band structures and the density of states reveals half-metallic behavior with a small indirect band gap $E_g$ of 0.51 eV around the Fermi level for the minority spin channels. The study of magnetic properties led to the predicted value of total magnetic moment $\mu_{tot} = 3\mu_B$, which nicely follows the Slater–Pauling rule $\mu_{tot} = Z_t - 18$. Several optical properties are calculated for the first time and the predicted values are in line with the Penn model. It is shown from the imaginary part of the complex dielectric function that the investigated alloy is optically metallic. The variations of thermodynamic parameters calculated using the quasi-harmonic Debye model agree well with the results predicted by the Debye theory. Moreover, the dynamical stability of the investigated alloy is computed by means of the phonon dispersion curves, the density of states, and the formation energies. Finally, the analysis of the strain effects reveals that PdVTe alloy preserves its ferromagnetic half-metallic behavior, it remains mechanically stable, the ionic nature dominates the atomic bonding, and the thermodynamic and the optical properties keep the same features in a large interval of pressure.

*Key words:* magnetism, elasticity, half-metallicity, half-Heusler, strain effects.

**Résumé :** Nous utilisons les plus précises méthodes de calcul des structures électroniques, i.e. la méthode linéarisée des ondes planes avec augmentations (*linearized augmented plane waves*) à potentiel complet plus une approche d'orbitale locale, afin d'étudier l'effet des déformations sur les propriétés magnétiques, élastiques, électroniques et thermodynamiques de l'alliage demi-Heusler PdVTe. L'analyse des structures de bande et de la densité d'états révèle le caractère demi-métallique avec un petit gap indirect de $E_g = 0.51$ eV autour du niveau de Fermi pour les canaux du spin minoritaire. L'étude des propriétés magnétiques mène à prédire la valeur du moment magnétique total, $\mu_{tot} = 3\mu_B$ qui suit bien la règle de Slater–Pauling $\mu_{tot} = Z_t - 18$. Plusieurs propriétés optiques sont calculées pour la première fois et les valeurs prédites sont en ligne avec le modèle de Penn. Nous montrons, à partir de la partie imaginaire de la fonction diélectrique complexe, que l'alliage étudié est optiquement métallique. Les variations des paramètres thermodynamiques, calculées en utilisant le modèle de Debye quasi-harmonique, sont en bon accord avec les résultats de la théorie de Debye. De plus, nous calculons la stabilité dynamique de l'alliage en utilisant les courbes de dispersion des phonons, la densité d'états et les énergies de formation. Finalement l'analyse des effets de déformation révèle que l'alliage PdVTe préserve son comportement demi-métallique, qu'il demeure mécaniquement stable, que le caractère ionique domine les liens atomiques et que les propriétés optiques et thermodynamiques conservent leurs propriétés sur un large intervalle de pression. [Traduit par la Rédaction]

*Mots-clés :* magnétisme, élasticité, demi-métallicité, demi-Heusler, effets de déformation.

## 1. Introduction

Ferromagnetism and the half-metallic behavior of the half-Heusler compounds have been an active field of experimental and theoretical research, due to their frequently promising novel properties and their technological applications since their first discovery in 1903 by Fritz Heusler [1]. de Groot found that some of these compounds were ferromagnetic, although none of their basic constituents showed magnetic behavior by themselves [2, 3]. It is noticeable that most of their physical properties can be predicted easily by counting their number of valence electrons [3, 4]. The objective of recent investigation related to half-Heusler compounds is to study ferromagnetic

alloys revealing the magnetic field induced super-elasticity, large strain-induced changes in the magnetization, and magnetic shape memory effect [4–8].

One sub-class of more than 200 Heusler alloys have semiconductor behavior [9]. They are the most suitable choice for the spintronic applications and the green energy related fields, such as thermoelectrics or solar cells. Remarkably, their band gaps can easily be changed from 0 to 4 eV by modifying their chemical composition.

Half-Heusler alloys are usually depicted by a generic formula $XYZ$ [10–17], where $X$ and $Y$ are transition metal elements and $Z$ stands for s–p elements. Their physical properties are related to the nature of elements $X$, $Y$, and $Z$, where the compound $XYZ$ can
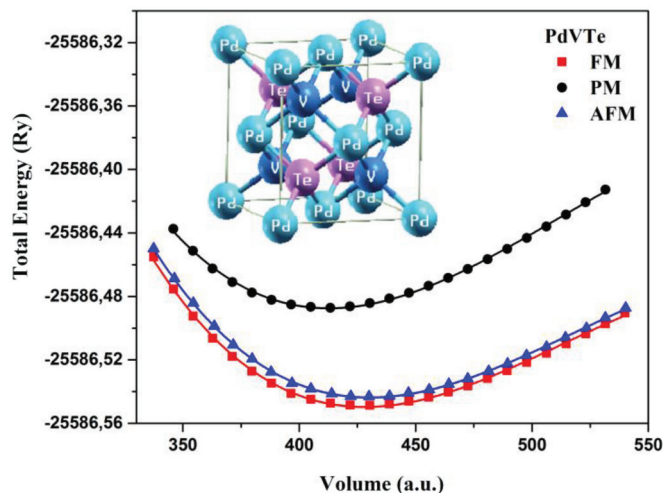
**Fig. 1.** Total energy as a function of the volume per formula unit for the ferromagnetic (FM), antiferromagnetic (AFM), and paramagnetic (PM) states of PdVTe alloy. Inset is the corresponding crystal structure. [Colour online.]



be characterized by ferromagnetism, antiferromagnetism, semi-conductivity, and optical properties [18, 19].

These properties are sensitive to phase change, temperature, and pressure [20]. They are good candidates for use in optoelectronic [21], topological insulator [22], photovoltaic, thermoelectric [23] and spintronic [24] devices. Therefore, Surucu et al. [25] investigated theoretically the structural, electronic, magnetic, and lattice dynamical properties for $X$CoBi ($X$ = Ti, Zr, Hf) half-Heusler compounds. They concluded that $\gamma$-$X$CoBi compounds have suitable electronic characteristic for flexible electronics. Another theoretical study suggests that physical properties of PdCo$X$ ($X$ = Si and Ge) and $X$RhSb ($X$ = Ti and Zr) half-Heusler compounds depend on the different atomic arrangements which are called $\alpha$, $\beta$, and $\gamma$ phases [26, 27].

The investigation of the structural, electronic, elastic, and mechanical properties of ZrNiPb half-Heusler alloy under pressure reveals that the investigated compound is a favorable thermoelectric material [28].

To contribute to this active area of research, we have investigated the strain effects on the magnetism, structure, electronic, elasticity, thermodynamic, and optical properties and the half-metallic behavior of PdVTe alloy by the use of the most accurate methods to electronic band structure (i.e., ab initio density functional theory calculations) [8].

At the stoichiometric composition, PdVTe alloy crystallizes in C1$_b$ structure. As shown in Fig. 1, the atoms Pd, V, and Te take the positions (0, 0, 0), (1/4, 1/4, 1/4), and (3/4, 3/4, 3/4), respectively. The symmetry of its C1$_b$ crystal structure, total number of valence electrons, and the large swap splitting of the d state of Pd and V elements due to the strong hybridization leads to the half-metallic ferromagnetic features of this alloy. This behavior is very similar to that of YCrSb and YMnSb [29]: they display metallic behavior in spin up and semiconducting behavior in the spin down.

The computational value of total magnetic moment for this compound ($3\mu_B$) is in line with the Slater–Pauling rule $\mu_{tot} = Z_t - 18$, which is often applied to several compounds [30]. The local magnetic moment of V dominates the total magnetic moment of this compound, whereas the local magnetic moments of Pd and Te are negligible.

The calculated elastic constants, using the stress–strain approach [31], show that PdVTe is mechanically stable. Furthermore, the study of Poisson's ratio $\nu$ supports the ionic character of this compound. The obtained values of Pugh's ratio $B/G$ and Cauchy pressure ($C_{12} - C_{44}$) demonstrate that this compound is brittle and PdVTe is stiffer than NaMgAl and RhMnSb [32, 33].

The optical properties, including imaginary and real parts of complex dielectric function, refractive index, reflectivity, and absorption coefficient, are predicted for the first time. The imaginary part of dielectric function reveals that the PdVTe alloy is optically metallic. The calculated values are in line with the Penn model [34, 35].

We have investigated the thermodynamic properties using the quasi-harmonic Debye model and we have obtained the dependence on temperature and pressure of numerous parameters including the thermal heat capacities $C_V$ and $C_p$, expansion coefficient $\alpha$, bulk modulus, Debye temperature $\theta$, and Grüneisen constant $\gamma$. The calculated variations of the thermodynamic parameters are in line with the results obtained by the Debye theory applied to several materials.

The phonon dispersion curves, the density of states, and the formation energies are calculated to investigate the dynamical stability.

Finally, the investigation of strain effects on the physical properties reveals that the compound preserves its ferromagnetic half-metallic behavior, remains mechanically stable, the optical and thermodynamic properties keep the same features, and the ionic nature dominates the atomic bonding in a large range of pressures.

## 2. Computational details

Calculations concerning magnetism, structure, elasticity, electronic, and optical properties are carried out within a state of the full-potential linearized augmented plane wave plus a local orbital (FP-LAPW + lo) approach as performed in the WIEN2k code based on density functional theory [8, 11]. To include an exchange correlation potential, generalized gradient approximation (GGA) Perdew–Burke–Ernzerhof and local density approximation (LDA) are adopted [12, 13]. We have applied Koelling and Harmon approach to integrate the relativistic effects on the computations. The convergence test led to the value of cutoff parameter RMT, $K_{max} = 8.0$, $l = 10$, and 3000 $k$-points are sufficient to obtain the energy precision of $10^{-6}$ Ry/formula unit. The values of radius RMT are 2.32, 2.26, and 2.32 for Pd, V, and Te, respectively.

Optimization of the volume ($V_0$), equilibrium lattice constant ($a_0$), and energy ($E_0$) is performed using the Murnaghan method [14].

The "stress–strain" approach is used to predict the independent elastic constants $C_{ij}$ and to study the elastic behavior of the PdVTe compound [15]. While PdVTe alloy crystallizes in C1$_b$ structure Born's stability criteria are applied as [16]

$$C_{11} + 2C_{12} > 0 \qquad C_{11} - C_{12} > 0 \qquad C_{44} > 0 \tag{1}$$

The adiabatic bulk modulus $B$, Poisson's ratio $\nu$, shear modulus $G$, Young's modulus $E$, and anisotropy factor $A$ are predicted using the Voigt–Reuss–Hill approximation [17]

$$B = \frac{C_{11} + 2C_{12}}{3} \tag{2}$$

$$G = \frac{1}{2}\left\{ \left[\frac{5(C_{11} - C_{12})C_{44}}{4C_{44} + 3(C_{11} - C_{12})}\right] + \left(\frac{C_{11} - C_{12} + 3C_{44}}{5}\right) \right\} \tag{3}$$

$$\nu = \frac{3B - 2G}{2(3B + G)} \tag{4}$$

$$E = \frac{9BG}{3B + G} \tag{5}$$

$$A = \frac{2C_{44}}{C_{11} - C_{12}} \tag{6}$$

The optical properties are deduced from the calculated parameters given by the complex dielectric function $\varepsilon(\omega)$ using Ehrenreich and Cohen's equation [18]:

$$\varepsilon(\omega) = \varepsilon_1(\omega) + i\varepsilon_2(\omega) \tag{7}$$

The real and imaginary parts are found using the Kramers–Kronig approach [18]

$$\varepsilon_1(\omega) = 1 + \frac{2}{\pi} P \int_0^\infty \frac{\omega' \varepsilon_2(\omega')}{\omega'^2 - \omega^2} d\omega' \tag{8}$$

$$\varepsilon_2(\omega) = \frac{8}{2\pi\omega^2} \sum_{nn'} \int_{BZ} |P_{nn'}(k)|^2 \frac{dS_k}{\nabla \omega_{nn'(k)}} \tag{9}$$

where $k$ is the wave vector in irreducible Brillouin zone and $P_{if}$ are the momentum matrix elements.

The refractive index $n(\omega)$ is derived from the complex dielectric function [19]

$$n(\omega) = \frac{1}{\sqrt{2}} \left[ \varepsilon_1 + \left( \varepsilon_1{}^2 + \varepsilon_2{}^2 \right)^{1/2} \right]^{1/2} \tag{10}$$

The reflectivity ($R$) describes the quantity of phonons reflected from the incident solids given by [20]

$$R(\omega) = \left| \frac{\sqrt{\varepsilon(\omega)} - 1}{\sqrt{\varepsilon(\omega)} + 1} \right|^2 \tag{11}$$

The thermodynamic properties are predicted using the quasi-harmonic Debye model realized in the Gibbs program. In this model, the thermodynamic parameters are described in the following form [21]:

$$B(P, T) = V \left[ \frac{\partial^2 G^*(V; P, T)}{\partial V^2} \right] \tag{12}$$

$$C_V = 3nk_B \left[ 4D\left(\frac{\theta}{T}\right) - \frac{3\theta/T}{e^{\theta/T} - 1} \right] \tag{13}$$

$$C_P = C_V(1 + \alpha\gamma T) \tag{14}$$

$$\alpha = \frac{\gamma C_V}{BV} \tag{15}$$

$$\gamma = -\frac{d\ln\theta(V)}{d\ln V} \tag{16}$$

## 3. Results and discussion

### 3.1. Magnetism, electronic, and half-metallic behavior

Structural optimization of PdVTe half-Heusler alloy was used to predict its ground state. Three cases were considered (paramagnetic, antiferromagnetic, and ferromagnetic phases). The variations of the total energies as a function of the volume, reported in Fig. 1, reveal that the ferromagnetic phase has lower

**Table 1.** Predicted equilibrium lattice constant $a_0$, energy $E_0$, and volume $V_0$ at the ferromagnetic phase of PdVTe.

| | $a_0$ (Å) | $E_0$ (eV) | $V_0$ (a.u$^3$) |
|---|---|---|---|
| GGA | 6.3284 | −348122.8515 | 427.5823 |
| LDA | 6.1599 | −347789.7684 | 419.1820 |

energy than the paramagnetic or antiferromagnetic phases, thus, the ferromagnetic phase is more stable, thus PdVTe is a ferromagnetic half-Heusler alloy [27, 36–39].

The optimized values obtained using the Murnaghan approach for volume ($V_0$), equilibrium lattice constant ($a_0$), and energy ($E_0$) predicted for the ferromagnetic phase using GGA and LDA approaches are shown in Table 1. The computed lattice constant ($a_0$) is about 6.3284 Å, as predicted by GGA, while that predicted by LDA is lower, as expected, at 6.1599 Å. At the same time, bulk modulus $B$ values are about 161.24 GPa (GGA) and 161.14 GPa (LDA).

The Curie point, or Curie temperature ($T_C$), is defined as the temperature above which some materials lose their permanent magnetic properties, which can be replaced by induced magnetism [38]. This important parameter may be predicted from the mean field approximation [39] using obtained ground state energy difference ($\Delta E$) between ferromagnetic and antiferromagnetic phases as

$$T_C = \frac{2}{3k_B} \Delta E \tag{17}$$

The computed Curie temperature $T_C$ is near room temperature (298 K), thus the magnetic properties of PdVTe alloy are not suppressed. Therefore, PdVTe alloy is suitable for spintronic applications. The obtained Curie temperature $T_C$ is higher than that of NaVTe (150 K) [40].

The predicted band structures for minority and majority spin channels in the ferromagnetic phase are illustrated in Fig. 2 for PdVTe alloy. It is evident that a minority of spin electrons show an indirect band gap, between the Γ point of the valence band and the X point for the conduction band, about 0.51 eV (GGA) around the Fermi level, which reveals its semiconducting nature. Furthermore, most spin channels display metallic character. These features are very similar to those of CoMnTe and RuMnTe and demonstrate that these alloys are ferromagnetic half-metallic [41]. As is well known, the local spin density approximation (LDA) in density functional theory always underestimates the band gaps of solids due to the lack of derivative discontinuity [42]. The band gap within LDA is 0.49 eV.

To better understand the origin of the indirect band gap in the minority spin channels and the attitude of electronic states, partial and total densities of states are estimated. The results are shown in Fig. 3 for the PdVTe alloy; the calculated total and partial densities of states for the minority spin electrons are represented by negative values. The total density of states around the half-metallic gap is largely dominated by the d states of the lower valent transition metal (V) atom, where the main peaks are about 3.73 and −4.49 states/eV situated approximately at −0.64 and 2.07 eV, respectively. In contrast, the main peaks of d states for Pd are 5.42 and −6.25 states/eV located about −4.41 and −4.25 eV, respectively. The influences of the s and p states are negligible around the half-metallic gap, and their contributions are positioned chiefly in the lowest zones of the total density of states around −5.89 eV for p states and −12.81 eV for s states; furthermore, the main peaks in total density of states around the Fermi level maintain the same positions as in the local densities of states. Obviously, the total density of states for PdVTe alloy is a superposition of the contributions of each local density of states.

**Fig. 2.** Electronic band structure for (*a*) majority and (*b*) minority spin electrons of PdVTe alloy. [Colour online.]
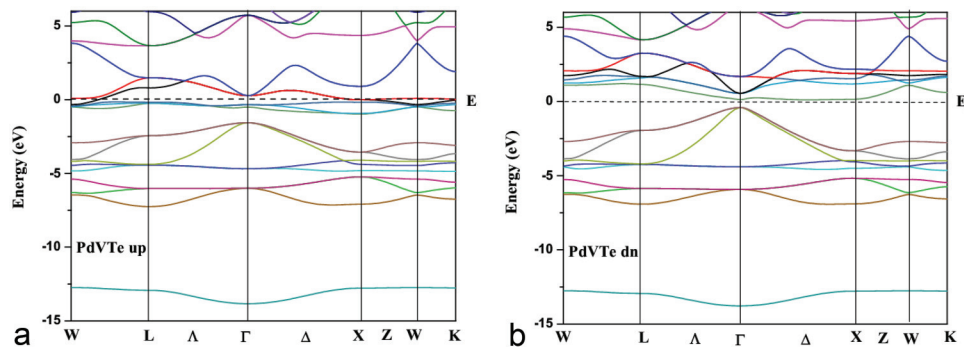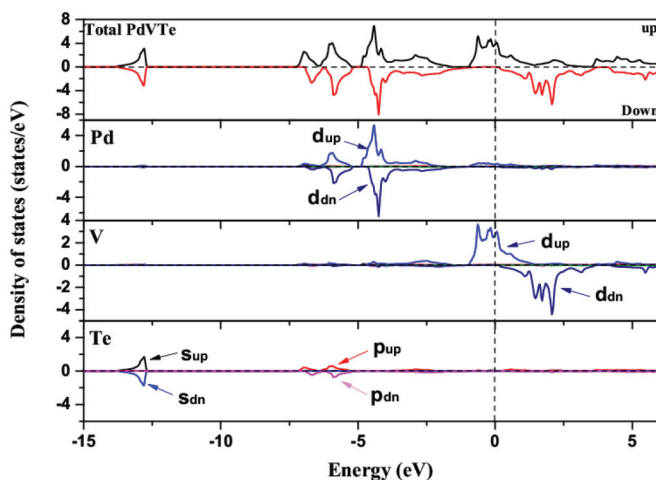


**Fig. 3.** Calculated spin-projected total and partial DOS plot for PdVTe alloy. [Colour online.]



The Fermi level is represented by the vertical dashed line in the densities of states plot presented in Fig. 3.

Noticeably, the behaviors of the calculated densities of states are comparable to those of CoCrSi, though the band gap is narrow at 0.66 eV for CoCrSi [32]. We illustrate in Fig. 4*a* the predicted band gaps of minority spin channels of some Te-based half-Heusler *XYTe* alloys. It is remarkable that the highest value of the half-metallic gap is about 1.4 eV for MnTiTe. The half-metallicity of PdVTe alloy is mainly a consequence of the symmetry of its $C1_b$ crystal structure and the strong hybridization between the d states of the V atom and the d states of the Pd atom [43]. Consequently, the compound PdVTe exhibits semiconducting behavior in the spin-down bands with a band gap $E_g$ around the Fermi level $E_F$ and metallic nature in the spin up bands. Tellurium (Te) with s and p states determines some of the physical properties and the structural stability of this alloy [44].

The calculated total magnetic moments $\mu_{tot}$ within GGA and LDA are almost the same and are $3\mu_B$, which nicely follows the Slater–Pauling rule (i.e., $\mu_{tot} = Z_t - 18$) [45]. It is noticeable that the local magnetic moment of the V site is higher than those of Pd and Te, as shown in Table 2. In fact, the total magnetic moments of all alloys counting Mn and V elements are large, as presented in Fig. 4*b*. Presently, there are no experimental values of total and local magnetic moments available to compare with our results.

To examine the strain effects on the magnetism and half-metallic behavior of the PdVTe alloy, we investigated the variation of the local and total magnetic moments as a function of the lattice constant under pressure up to 30 GPa. From Fig. 5, it is noticeable that during the contraction of the unit cell volume the interactions between Pd and V increase; therefore, the V local moment decreases, whereas the local magnetic moment of Pd increases. However, PdVTe total magnetic moment is kept at $3\mu_B$ per unit cell in the interval [6.1 Å, 6.45 Å].

To verify the ability of this material to maintain its half-metallic character under the effect of uniform strain, the half-metallic gap variations as a function of the lattice constant in a large interval were studied. We have found that PdVTe alloy conserves its half-metallic features in the interval [6 Å, 6.5 Å], whereas outside this interval, the contraction and the expansion destroy this behavior. As the expansion moves the Fermi level $E_F$ downwards and contraction moves it upwards in energy, the Fermi level will eventually be in the conduction band or in the valence band; that is, the half-metallic alloy becomes purely metallic. Visibly, PdVTe is less robust than RuVTe, which maintains its features in a large interval of pressure [5.8 Å, 6.6 Å] because of its large half-metallic band gap ($E_g = 0.89$ eV). The exceptional magnetic and half-metallic properties of PdVTe qualify it as a promising functional alloy in the spintronic field, such as magnetic tunnel junctions, spin-transfer torque devices, spin valves, and giant-magnetoresistance.

### 3.2. Elastic properties

To finalize the compound for an engineering product or technological application, it is imperative to recognize its elastic properties. The elastic parameters give important data about the nature of the bonding forces in solids and provide information about materials' responses to mechanical strength, pressure, and even phase transition. The elastic properties play a significant role in several technological applications, such as load deflection, thermoelastic stress, internal strain, sound velocities, phase transformation, and fracture toughness. Using the "stress–strain" method, the independent elastic constants $C_{ij}$ are evaluated. $C_{11}$ characterizes the elasticity in length, and $C_{44}$ and $C_{12}$ represent the elasticity in shape. While PdVTe is a cubic compound, to verify the stability of the lattice, we utilize Born's stability criteria as shown in eq. (1).

The independent elastic parameters for PdVTe alloy are listed in Table 3. Our calculated values show that this compound is mechanically stable. The predicted value of the elastic parameter $C_{11}$ is 225.78 GPa, thus, PdVTe displays more resistance to unidirectional compression than RuVTe ($C_{11} = 161.25$ GPa) or LiMgAl ($C_{11} = 32.074$ GPa) [32].

The bulk modulus *B* measures the material's resistance to applied pressure. The calculated bulk modulus value from Murnaghan's equation of state is 161.24 GPa, which is very close to the value calculated from "stress–strain" method using eq. (12) (161.32 GPa). The similarity between the two values estimates the accuracy of our elastic calculations. The larger the value of bulk modulus,

**Fig. 4.** (*a*) Calculated band gaps of minority spin channel. (*b*) Calculated total magnetic moments of some Te-based half-Heusler *XYTe* alloys. [Colour online.]
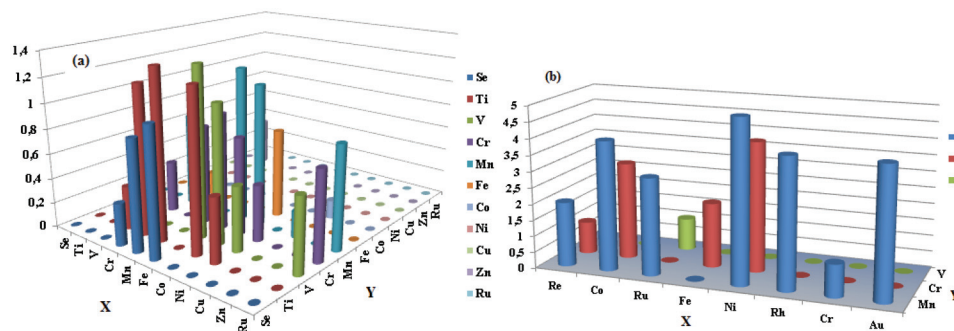
**Table 2.** Calculated local and total magnetic moments of PdVTe alloy.

| Compound | Local magnetic moment, $\mu_B$ | | | Interstitial | Total $\mu_B$ |
| --- | --- | --- | --- | --- | --- |
| | Pd | V | Te | | |
| PdVTe | 0.02768 | 2.60148 | –0.05081 | 0.42225 | 3.00060 |

**Fig. 5.** The lattice constant dependences of the total and local magnetic moments for PdVTe. [Colour online.]
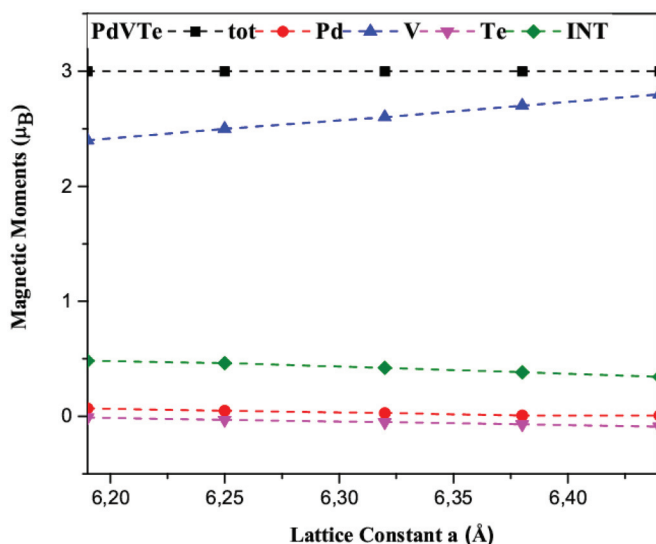


**Table 3.** Predicted elastic constants $C_{ij}$ (GPa), bulk modulus $B$ (GPa), shear modulus $G$ (GPa), Pugh's ratio $B/G$, Poisson's ratio $\nu$, Young's modulus $E$ (GPa), and anisotropy factor $A$.

| | $C_{11}$ | $C_{12}$ | $C_{44}$ | $B$ | $G$ | $B/G$ | $\nu$ | $E$ | $A$ |
| --- | --- | --- | --- | --- | --- | --- | --- | --- | --- |
| PdVTe | 225.78 | 129.10 | 148.36 | 161.32 | 95.76 | 1.68 | 0.25 | 239.82 | 3.07 |

the stronger the capacity to resist deformation [46]. The large bulk modulus value of PdVTe alloy reveals that it has strong resistance to volume change by applied pressure.

The shear modulus $G$ is a measure of resistance to reversible deformation. It is well known that the larger the value of $G$, the

stronger the capacity of the resist shear deformation. The computed value reveals that PdVTe has a larger value than CoCrTe. Hence, the deformation resistance capacity of PdVTe is much stronger than that of CoCrTe [32].

Poisson's ratio parameter $\nu$ supplies data about nature of the forces operating in solids. Our calculated value of Poisson's ratio $\nu$ is about 0.25, which proves that the atomic bonds are dominated by ionic forces. The predicted value of $G/B$ is 0.6, which also supports the ionic character of this compound [32]. According to Pugh's ratio $B/G$ and Cauchy pressure ($C_{12} - C_{44}$) values we can determine the ductility or brittleness of the compound. The predicted value of Cauchy pressure ($C_{12} - C_{44}$) for PdVTe is negative, thus, this compound is brittle. The calculated value of Pugh's ratio $B/G$ for PdVTe (1.68) is less than 1.75, which also characterized this compound as a brittle material [33]. To investigate the anisotropy of PdVTe, we have calculated the elastic anisotropy parameter, $A$. The compound is described as absolutely isotropic when $A$ is equal to 1. The estimated value of elastic anisotropy $A$ for PdVTe is about 3.07. Young's modulus $E$ gives an idea of the stiffness of compounds: the matter is stiffer when Young's modulus is high. The calculated value of the Young's modulus is 239.82 GPa. Therefore, PdVTe is stiffer than NaMgAl and RhMnSb compounds [32, 33].

The pressure dependence of the elastic parameters is very important for the characterization of the materials. The elastic parameters $C_{ij}$, $B$, $G$, $E$, $A$, $\nu$, and $G/B$ under varying pressure up to 30 GPa by steps of 5 GPa, are computed and presented in Fig. 6. Evidently, $C_{11}$ and $C_{12}$ increase at increased pressure values, while $C_{44}$ decreases. Therefore, the bulk modulus and Poisson's ratio increase linearly with the pressure, although the shear modulus, Young's modulus, the anisotropy factor, and the $G/B$ ratio decrease. The critical value of $G/B$ ratio that separates ductile and brittle materials is about 0.6. Figure 6 reveals that the $G/B$ ratio is smaller than 0.57, therefore, PdVTe remains ductile in the considered interval of pressure.

## 3.3. Optical properties

The optical properties of matter supply much information on various aspects of its physical properties, such as the phenomena relating to the presence of impurities and defects and their nature, and give an important idea of vibrational and electronic states. The optical properties of matter play a vital role in several technological applications, such as optical instruments among which are light emitting diodes (LED) designed for the photovoltaic cells and lighting and diode lasers used in the heads of CD and DVD reading devices.

To investigate the optical properties, several optical parameters, including imaginary and real parts of complex dielectric function, refractive index, reflectivity, and absorption coefficient, are predicted for the first time.

**Fig. 6.** Calculated elastic parameters ($C_{ij}$, $B$, $G$, $E$, $A$, $G/B$) of PdVTe under pressure up to 30 GPa. [Colour online.]
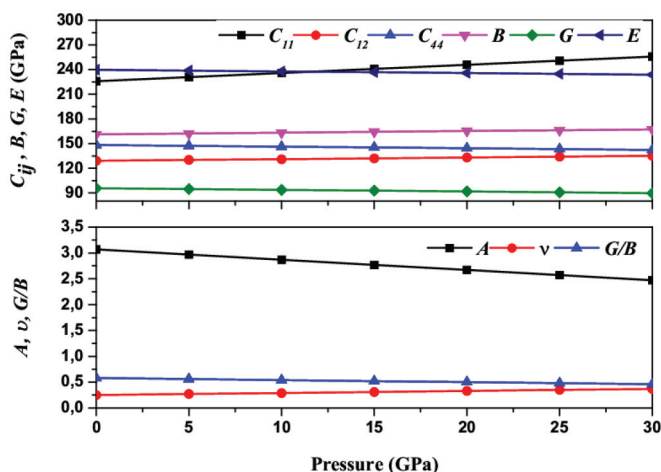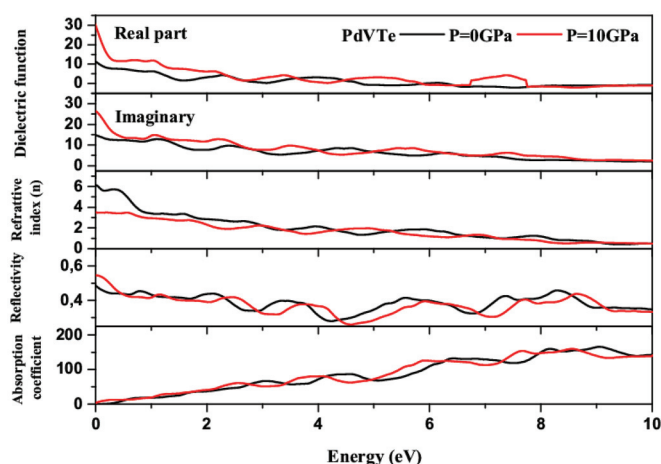


**Fig. 7.** Dielectric function, refractive index, reflectivity, and absorption coefficient as a function of energy at various pressures for the PdVTe alloy. [Colour online.]



We illustrate the calculated imaginary and real parts of the dielectric function in Fig. 7. Obviously, study of the imaginary part of dielectric function $\varepsilon_2(\omega)$ proves that our investigated alloy is optically metallic, due to the high values of $\varepsilon_2(\omega)$ for both pressures 0 GPa ($\varepsilon_2(0) = 15.03$) and 10 GPa ($\varepsilon_2(0) = 26.32$). Transitions of electrons from p state of Te in the valence band to the d states of Pd and V inside the conduction band generate the high-energy peaks observed in the spectra of the imaginary part of dielectric function $\varepsilon_2(\omega)$. At small energies, peaks are extremely low compared to those close to zero energy, which demonstrate the high degree of optical conductivity at low frequencies.

From Fig. 6, it is clear that the highest values of the real part of dielectric function $\varepsilon_1(\omega)$ for pressures 0 and 10 GPa are 11.16 and 31.14, respectively, at zero frequency. The value at 10 GPa is higher than for 0 GPa due to decrease of the band gap, and the calculated values are in line with the Penn model [47], which suggests an inverse relationship between the real part of the dielectric function $\varepsilon_1(\omega)$ at zero frequency and band gap $E_g$. The negative values of $\varepsilon_1(\omega)$ in interval [4.75 eV, 10 eV] of energy correspond to the complete attenuation of incident light (photons).

Refractive index is a significant parameter for photoelectric technology, which describes how fast photons pass through solids.

**Table 4.** Calculated real part of complex dielectric function $\varepsilon_1(0)$, optical band gap ($E_{OG}$), refractive index $n(0)$, and reflectivity $R(0)$ for PdVTe half-Heusler alloy.

| $P$ (GPa) | $\varepsilon_1(0)$ | $E_{OG}$ | $n(0)$ | $R(0)$ |
|---|---|---|---|---|
| 0 | 11.16 | 15.03 | 3.56 | 0.54 |
| 10 | 31.14 | 26.32 | 6.21 | 0.57 |

From Fig. 7, the nonlinear behavior of the refractive index is shown by the presence of peaks in the infrared region. The inter-band transition from the highest valence band to the lowest conduction band generates different peaks in the interval [0 eV, 10 eV]. The main values are located at zero frequency for both pressures 0 and 10 GPa, and slowly diminish in the visible zone reaching an approximate value of zero.

Reflectivity, shown in Fig. 7, exhibits highest values at zero frequency for both pressure 0 and 10 GPa due to the metallic feature of our studied alloy, shown previously in the investigation of the imaginary part. Reflectivity variations decrease from 0.48 and 0.55 for 0 and 10 GPa, respectively, to approximately 0.3 at 5 eV, and become more important with a peak of 0.45 at approximately 9 eV. In the interval of energies where the real part $\varepsilon_1(\omega)$ becomes negative, the peaks rise higher, which reveals that the reflectivity of PdVTe is more important to the incident light (photons) in this range of energy.

Absorption coefficient shown in Fig. 7 describes how solids take up light's energy and transform it into internal energy. It is obvious that the threshold point is very close to 0 eV due to the small band gap of PdVTe alloy. High peaks are located in the visible region for both pressure 0 GPa and 10 GPa, these peaks describe the greater capability to absorb light. The highest peaks are located in the visible region because of the transitions between the closely split levels of energy. The features of the absorption variations for both pressures are similar. Our predicted optical results are summarized in Table 4.

### 3.4. Thermodynamic properties

The thermodynamic parameters supply much more information and detail about the material's specific behaviors under harsh conditions, such as high pressure or high temperature; therefore, we investigate the thermodynamic properties by applying the quasi-harmonic Debye model to the half-Heusler PdVTe compound [29], we predict the thermal expansion $\alpha$, specific heat capacities at constant pressure ($C_P$) and constant volume ($C_V$), bulk modulus, Debye temperature ($\theta$), and Grüneisen parameter ($\gamma$) in the temperature range from 0 to 1000 K in steps of 100 K under a series of pressure values from 0 to 30 GPa in steps of 10 GPa.

Heat capacity is a significant parameter for the matter thermodynamic properties, defined as the quantity of heat to be furnished to a given mass of matter to generate a unit change in its temperature. Generally, heat capacity provides a lot of information about phase transition and lattice vibration.

Figure 8 displays the variations of the specific heat capacities at constant volume $C_V$ and at constant pressure $C_P$ as a function of temperature and pressure for the half-Heusler PdVTe compound. It is clear that the temperature has a very strong effect on $C_V$ and $C_P$ at low temperature, approximately from 0 to 300 K; they are very close together because of the sharp increase of $C_V$ and $C_P$, due to the anharmonic approximation of the Debye model at lower temperature used in the calculations, whereas, at high temperatures, this anharmonic effect is suppressed and $C_V$ undergoes a linear increase and saturates quickly to the Dulong–Petit limit, which proves that thermal energy excites all the possible phonon modes, and is frequent to all solids at high temperatures [29], although for $C_P$, the values increase monotonically with

**Fig. 8.** Variations of (*a*) specific heat capacity ($C_V$, $C_P$) and (*b*) thermal expansion $\alpha$ and bulk modulus $B$ with temperature at various pressures for PdVTe alloy. [Colour online.]
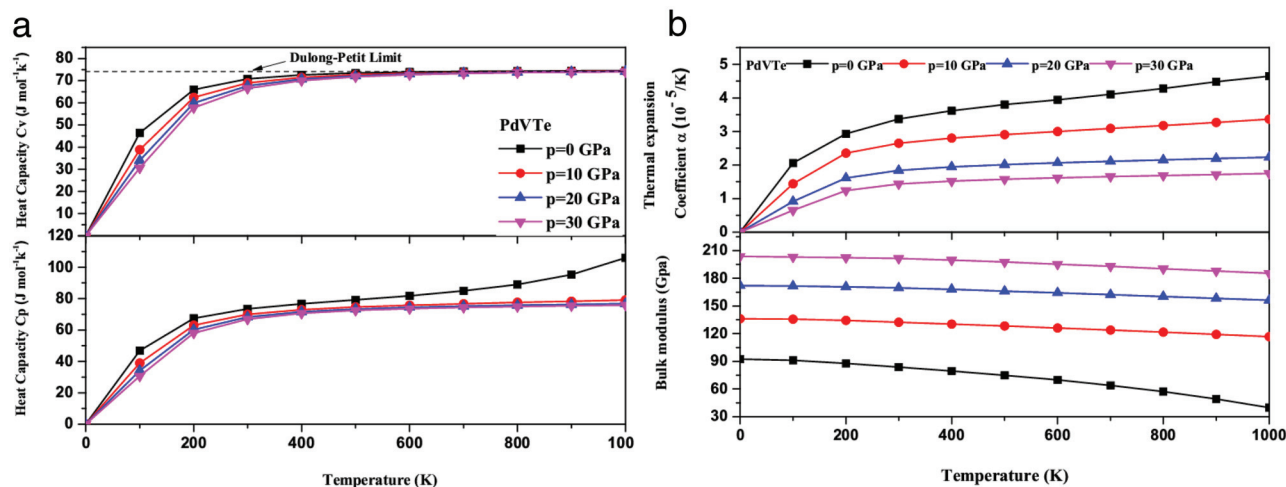


temperature. Moreover, the pressure has the reverse effect (i.e., both specific heat capacities at constant pressure $C_P$ and at constant volume $C_V$ decrease with increasing pressure). At null pressure and 300 K, $C_V$ and $C_P$ for the investigated compound are 70.47 and 73.31 Jmol$^{-1}$K$^{-1}$, respectively.

The thermal expansion parameter $\alpha$ has both practical and theoretical importance: it is crucial to describe the tendency of a material to change its volume, shape, and area in response to a change in temperature at constant pressure and it is also important in estimating the thermodynamic equation of state.

The calculated values of the thermal expansion parameter $\alpha$ as function of temperature and pressure are displayed in Fig. 8. It is obvious that the thermal expansion $\alpha$ increases markedly with temperature from 0 to 1000 K; furthermore, the variation of $\alpha$ increases sharply with temperature lower than 300 K. This phenomenon is because of the anharmonic effect of the Debye model at lower temperature. This feature is strongly depressed at high temperature; for temperature higher than 300 K, the variation of the thermal expansion $\alpha$ increases slowly and increasingly turns into a linear increase. It is remarkable that, for a given temperature, the values of $\alpha$ decrease continuously with pressure increase, which reveal that high pressure suppresses $\alpha$. At null pressure and 300 K, the calculated value of the thermal expansion $\alpha$ for the studied PdVTe compound is about $3.34 \times 10^{-5}$ K$^{-1}$.

We have used the quasi-harmonic Debye's approximation to investigate the variation of bulk modulus with respect to temperature and pressure. The plot of bulk modulus $B$ is significant as it alone can show the pressure and temperature features of elastic constants and also that of other moduli of elasticity. Figure 8 shows that the bulk modulus $B$ decreases at constant pressure while temperature increases, which reveals that the elastic constants $C_{ij}$ will also decrease with the increase of temperature. Therefore, all of the moduli of elasticity decrease as temperature increases at constant pressure. This feature leads to an important property of PdVTe half-Heusler alloy. It reveals the high-temperature working interval of this alloy, which is a most important condition for several technological applications like superconductivity and thermoelectricity [30]. On the other hand, the bulk modulus increases at constant temperature as pressure increases, thereby indicating the increase of elastic constants and consequently the other moduli of elasticity. The variation of bulk modulus with respect to pressure at constant temperature shows the disadvantages of the investigated alloy at high pressure ranges. The melting point and the boiling point of PdVTe alloy also increases as pressure increases. This character makes this alloy a poor

**Fig. 9.** Variations of Debye temperature $\theta$ (K) and Grüneisen parameter $\gamma$ with temperature at various pressures for PdVTe alloy. [Colour online.]
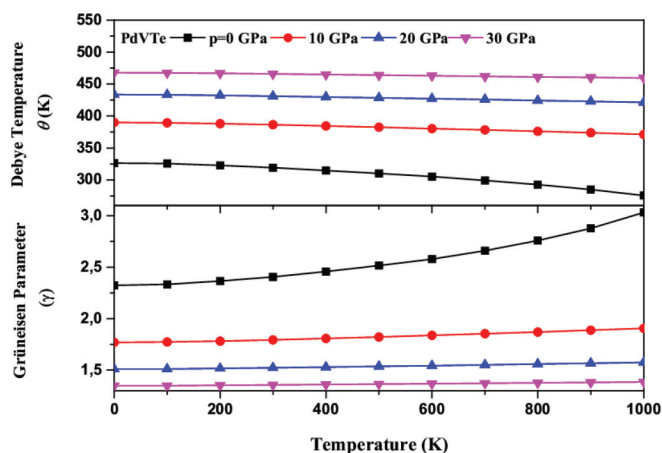


candidate for a number of applications, such as soldering and optical applications.

The Grüneisen parameter $\gamma$ is of great significance because it appears in several main thermodynamic relations: $\gamma$ interprets the consequence that changing the volume of a crystal lattice has on its vibrational properties, and, so, the consequence that temperature change has on the dynamics and size of the crystal lattice. The variations of Grüneisen parameter $\gamma$ are shown in Fig. 9. It is noticeable that the Grüneisen parameter decreases with pressure increase when temperature is kept constant. However, at constant pressure, the Grüneisen parameter continuously increases as temperature increases, but its variation rate is strongly suppressed by higher pressure. The predicted value of $\gamma$ of PdVTe compound at zero pressure and 300 K is 2.40.

The Debye temperature is a physical parameter, which provides information about physical properties of matter, such as thermal conductivity, electric conductivity, specific heat, and broadening. It is defined as the highest temperature that can be achieved due to a single normal vibration. From Fig. 9, it is obvious that the Debye temperature $\theta$ smoothly decreases as temperature increases, when the pressure is kept constant. At low

**Fig. 10.** (*a*) Phonon dispersion curves along the high symmetry directions, the acoustic modes are highlighted in red. (*b*) Partial and total phonon density of states in PdVTe alloy. [Colour online.]
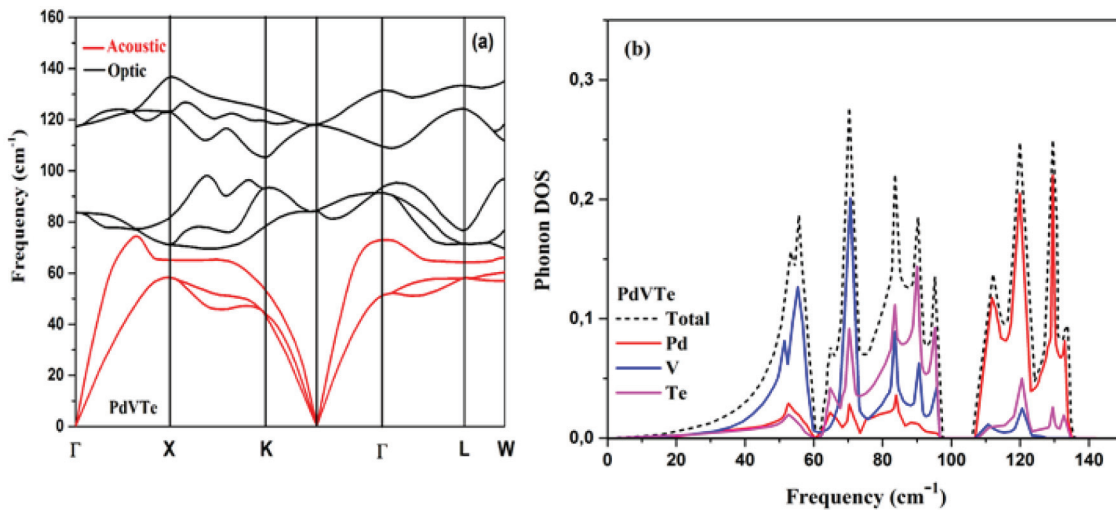
range of temperature from 0 to 300 K, there is a small variation. Whereas, the decreasing rate of Debye temperature becomes stronger at high temperature, while the variation rate is larger at lower pressure. Nevertheless, at constant temperature, the Debye temperature continuously increases with increasing pressure. The calculated value of the Debye temperature $\theta$ of the studied compound at zero pressure and 300 K is 319.09 K.

### 3.5. Dynamical stability

The investigation of phonons is a significant part of condensed matter physics. They play an essential role in thermal properties and dynamical behaviors.

Computations of phonon dispersion curves in high-symmetry lines of the Brillouin zone and phonon density of states are performed for PdVTe employing the finite displacement approach, implemented in the Phonopy code [46], using a supercell of size $2 \times 2 \times 2$ of primitive lattice type with 24 atoms.

The obtained results of phonon dispersion curves are illustrated in Fig. 10*a*. Obviously, there are no imaginary modes, and all the phonon modes have positive frequencies. This result reveals that PdVTe alloy is dynamically stable. Nine vibrational modes (three acoustic and six optical modes) appear due to the presence of three atoms in the primitive unit cell of PdVTe alloy. At the $\Gamma$ point, the frequencies of optical modes are 84.62 cm$^{-1}$ (degenerate) and 118.17 cm$^{-1}$ (degenerate). The phonon dispersion curves are divided into two distinct regions with a narrow gap of about 8.2 cm$^{-1}$. The low-frequency band region from 0 to 96.3 cm$^{-1}$ contains three optical and three acoustic branches. On the other hand, the high frequency band region from 106 to 137 cm$^{-1}$ is formed by the remaining three optical phonon branches. The maximum frequency of acoustic modes is 74.61 cm$^{-1}$ and the minimum frequency of optical modes is 69.45 cm$^{-1}$. Noticeably, there is no phonon gap between optical and acoustic branches, indicating a strong acoustic–optical phonon scattering, which will suppress the lattice thermal conductivity. Figure 10*b* illustrates the total and partial phonon density of states of PdVTe alloy, which reveals that the phonon density of states in the acoustic region is mostly contributed by the vibration of the V atom, whereas the Pd atom exhibits its largest contribution in the highest optical phonon branches. The highest peak of the total phonon density of states is located at 70.31 cm$^{-1}$.

To examine the possible experimental formation of PdVTe alloy, we predict its formation energy $E_F$ with the following expression [48]:

$$E_F = E_{total} - \left[ E_b(Pd) + E_b(V) + E_b(Te) \right] \tag{18}$$

where $E_b$ is the energy per atom and $E_t$ is the total energy of primitive cell. The estimated $E_F$ of PdVTe alloy is –0.987 eV/atom. This negative value signifies that the synthesis of the investigated compound is energetically favorable, and consequently it can be easily experimentally fabricated.

The thermal conductivity ($\lambda$) is the most important parameter for the thermoelectric applications. Cahill, Clarke and Long [49] models are used to predict the minimum thermal conductivity value $\lambda_{min}$ and the diffusion thermal conductivity $\lambda_{diff}$ is given by the Synder [49] model. The obtained results of $\lambda_{min}$ are 0.291, 0.264, and 0.223 W/m K predicted by Cahill, Clarke, and Long, respectively, whereas $\lambda_{diff}$ is about 0.172 W/m K. The computed thermal conductivities of PdVTe are smaller than those of Tl$_4$Ag$_{18}$Te$_{11}$ compound [49].

## 4. Conclusion

We have investigated the strain effects on the magnetism, elasticity, electronic, thermodynamic, and optical properties of the PdVTe half-Heusler alloy applying the FP-LAPW + lo approach implemented by WIEN2k simulation code. The calculated value of equilibrium lattice constant demonstrates that PdVTe alloy is stable in C1$_b$ structure. The study of the electronic properties reveals the half-metallic behavior with a small indirect band gap $E_g$ of 0.51 eV around the Fermi level for the minority spin channels. The predicted value of total magnetic moment $\mu_{tot}$ is $3\mu_B$ per unit cell, and nicely follows the Slater–Pauling rule $\mu_{tot} = Z_t -$ 18. The imaginary and real parts of complex dielectric function, refractive index, reflectivity, and absorption coefficient are predicted for the first time, and they are in line with the Penn model. The imaginary part of the dielectric function reveals that the PdVTe alloy is optically metallic. The thermodynamic properties are investigated using the quasi-harmonic Debye model, and the calculated variations are in line with the results obtained by the Debye theory. The dynamical stability is confirmed by the calculated phonon dispersion curves, the density of states, and the formation. Finally, the analysis of the strain effects reveals that the PdVTe alloy maintains ferromagnetic half-metallic features in a large interval of pressure, the studied compound remains mechanically stable, the ionic nature dominates the atomic bonding, and the electronic, thermodynamic, and optical properties keep the same features in the investigated pressure interval.

The exceptional magnetism, elasticity, half-metallicity, electronic, thermodynamic, and optical properties of PdVTe qualify it as a promising functional alloy in the spintronic and optoelectronic fields.

## References

1. F. Heusler. Verh. Dtsch. Phys. Ges. **5**, 217 (1903).
2. R.A. de Groot, F.M. Mueller, P.G. van Engen, and K.H.J. Buschow. Appl. Phys. **55**, 2151 (1984). doi:10.1063/1.333593.
3. I. Žutić, J. Fabian, and S.D. Sarma. Rev. Mod. Phys. **76**, 323 (2004). doi:10.1103/RevModPhys.76.323.
4. R.A. de Groot, F.M. Mueller, P.G.V. Engen, and K.H.J. Buschow. Phys. Rev. Lett. **50**, 2024 (1983). doi:10.1103/PhysRevLett.50.2024.
5. C. Felser and A. Hirohata, Editors. Heusler alloys, properties, growth, applications. Vol. 222. Springer International Publishing, Basel, Switzerland. 2016.
6. T. Graf, F. Casper, J. Winterlik, B. Balke, G.H. Fecher, and C. Felser. Z. Anorg. Allg. Chem. **635**, 976 (2009). doi:10.1002/zaac.200900036.
7. C. Felser and G.H. Fecher, Editors. Spintronics: from materials to devices. Springer Netherlands, Dordrecht, Netherlands. 2013.
8. D.J. Singh and L. Nordstrom. Planewaves, pseudopotentials, and the LAPW Method. Springer Science+Business Media, Berlin, Heidelberg, Germany. 2006.
9. F. Casper, T. Graf, S. Chadov, B. Balke, and C. Felser. Semicond. Sci. Technol. **27**, 063001 (2012). doi:10.1088/0268-1242/27/6/063001.
10. Z. Peng Hao, R. Liu, Y. Hang Fan, and L. Li Wang. J. Alloys Compd. **820**, 153118 (2020). doi:10.1016/j.jallcom.2019.153118.
11. P. Blaha, K. Schwarz, G.K.H. Madsen, D. Kvasnicka, and J. Luitz. WIEN2k: an augmented plane wave plus local orbitals program for calculating crystal properties. 2nd ed. Vienna University of Technology, Vienna, Austria. 2001.
12. Z. Wu and R.E. Cohen. Phys. Rev. B, **73**, 235116 (2006). doi:10.1103/PhysRevB.73.235116.
13. J.P. Perdew, K. Burke, and M. Ernzerhof. Phys. Rev. Lett. **77**, 3865 (1996). doi:10.1103/PhysRevLett.77.3865.
14. F.D. Murnaghan. Proc. Natl. Acad. Sci. U.S.A. **30**(9), 244 (1944). doi:10.1073/pnas.30.9.244.
15. A. Reuss. Z. Angew. Math. Mech. **9**, 49 (1929). doi:10.1002/zamm.19290090104.
16. J. Wang, J. Li, S. Yip, S. Phillpot, and D. Wolf. Phys. Rev. B, **52**, 12627 (1995). doi:10.1103/PhysRevB.52.12627.
17. G.V. Sin'ko and N.A. Smirnov. J. Phys. Condens. Matter, **14**, 6989 (2002). doi:10.1088/0953-8984/14/29/301.
18. M. Shakil, S. Hassan, H. Arshad, M. Rizwan, S.S.A. Gillani, M. Rafique, M. Zafar, and S. Ahmed. Phys. B Condens. Matter, **575**, 411677 (2019). doi:10.1016/j.physb.2019.411677.
19. R. Majumder, M.M. Hossain, and D. Shen. Mod. Phys. Lett. B, **33**, 1950378 (2019). doi:10.1142/S0217984919503780.
20. B. Anissa, D. Radouan, and B. Benaouda. Int. J. Mod. Phys. B, **33**, 1950247 (2019). doi:10.1142/S0217979219502473.
21. D. Kieven, R. Klenk, S. Naghavi, C. Felser, and T. Gruhn. Phys. Rev. B, **81**, 075208 (2010). doi:10.1103/PhysRevB.81.075208.
22. S.-Y. Lin, M. Chen, X.-B. Yang, Y.-J. Zhao, S.-C. Wu, C. Felser, and B. Yan. Phys. Rev. B, **91**, 094107 (2015). doi:10.1103/PhysRevB.91.094107.
23. P. Kumar Kamlesh, R. Gautam, S. Kumari, and A.S. Verma. Phys. B. Condens. Matter, **615**, 412536 (2021). doi:10.1016/j.physb.2020.412536.
24. L. Damewood, B. Busemeyer, M. Shaughnessy, C.Y. Fong, L.H. Yang, and C. Felser. Phys. Rev. B, **91**, 064409 (2015). doi:10.1103/PhysRevB.91.064409.
25. G. Surucu, M. Isik, A. Candan, X. Wang, and H.H. Gullu. Phys. B. Condens. Matter, **587**, 412146 (2020). doi:10.1016/j.physb.2020.412146.
26. A. Erkisi, G. Surucu, and R. Ellialtioglu. Philos. Mag. **97**(26), 2237 (2017). doi:10.1080/14786435.2017.1329595.
27. G. Surucu, A. Candan, A. Erkisi, A. Gencer, and H.H. Güllü. Mater. Res. Express, **6**(10), 106315 (2019). doi:10.1088/2053-1591/ab4039.
28. M.I. Babalola, B.I. Adetunji, B.E. Iyorzor, and A. Yaya. Int. J. Mod. Phys. B, **32**, 1850248 (2018). doi:10.1142/S021797921850248X.
29. M.A. Sattar, M. Rashid, M.R. Hashmi, S.A. Ahmad, M. Imran, and F. Hussain. Chinese Phys. B, **25**(10), 107402 (2016). doi:10.1088/1674-1056/25/10/107402.
30. A. Kılıç, N. Kervan, and S. Kervan. J. Supercond. Nov. Magn. **28**, 1767 (2015). doi:10.1007/s10948-014-2941-1.
31. C. Çoban, Y.Ö. Çiftçi, and K. Çolakoğlu. Indian J. Phys. **90**(11), 1233 (2016). doi:10.1007/s12648-016-0873-2.
32. A. Afaq, A. Bakar, M. Rizwan, M.A. Fareed, H.B. Munir, and A. Asif. Mod. Phys. Lett. B, **33**(8), 1950093 (2019). doi:10.1142/S0217984919500933.
33. I. Muhammad, J.-M. Zhang, A. Ali, M.U. Rehman, and S. Muhammad. Mater. Chem. Phys. **251**, 123110 (2020). doi:10.1016/j.matchemphys.2020.123110.
34. N. Mehmood and R. Ahmad. J. Supercond. Nov. Magn. **31**, 233 (2018). doi:10.1007/s10948-017-4196-0.
35. N. Mehmood, R. Ahmad, and G. Murtaza. J. Supercond. Nov. Magn. **30**, 2481 (2017). doi:10.1007/s10948-017-4051-3.
36. A. Erkisi and G. Surucu. Mater. Res. Express, **4**, 066504 (2017). doi:10.1088/2053-1591/aa730e.
37. Q. Wang, Q. Du, C. Petrovic, and H. Lei. Chinese Phys. Lett. **37**(2), 027502 (2020). doi:10.1088/0256-307X/37/2/027502.
38. A. Erkisi, B. Yildiz, X. Wang, M. Isik, Y. Ozcan, and G. Surucu. J. Magn. Magn. Mater. **519**, 167482 (2021). doi:10.1016/j.jmmm.2020.167482.
39. G. Surucu, B. Yildiz, A. Erkisi, X. Wang, and O. Surucu. J. Alloys Compd. **838**, 155436 (2020). doi:10.1016/j.jallcom.2020.155436.
40. M.A. Sattar, S.A. Ahmad, F. Hussain, and C. Cazorla. J. Materiomics, **5**(3), 404 (2019). doi:10.1016/j.jmat.2019.04.003.
41. T. Djaafri, A. Djaafri, A. Elias, G. Murtaza, R. Khenata, R. Ahmed, S.B. Omran, and D. Rached. Chinese Phys. B, **23**(8), 087103 (2014). doi:10.1088/1674-1056/23/8/087103.
42. D.P. RaiSandeep, A. Shankar, A.P. Sakhya, T.P. Sinha, R. Khenata, M.P. Ghimire, and R.K. Thapa. Mater. Res. Express, **3**, 075022 (2016). doi:10.1088/2053-1591/3/7/075022.
43. I. Galanakis, P.H. Dederichs, and N. Papanikolaou. Phys. Rev. B, **66**, 134428 (2002). doi:10.1103/PhysRevB.66.134428.
44. T. Djaafri, A. Djaafri, and F. Saadaoui. J. Supercond. Nov. Magn. **31**, 2449 (2018). doi:10.1007/s10948-017-4510-x.
45. I. Galanakis, P.H. Dederichs, and N. Papanikolaou. Phys. Rev. B, **66**, 174429 (2002). doi:10.1103/PhysRevB.66.134428.
46. A. Togo and I. Tanaka. Scr. Mater. **108**, 1 (2015). doi:10.1016/j.scriptamat.2015.07.021.
47. D.R. Penn. Phys. Rev. **128**(5), 2093 (1962). doi:10.1103/PhysRev.128.2093.
48. X. Wang, Z. Cheng, G. Liu, X. Dai, R. Khenata, L. Wang, and A. Bouhemadou. IUCrJ, **4**, 758 (2017). doi:10.1107/S2052252517013264.
49. A. Gencer, O. Surucu, G. Surucu, and E. Deligoz. J. Solid State Chem. **289**, 121469 (2020). doi:10.1016/j.jssc.2020.121469.

# Structural, elastic, electronic and optical investigations of fluoride-perovskite NaBeF₃: first-principles calculations

K. Hamada, T. Djaafri, A. Bendjedid, A. Djaafri, F. Saadaoui & D. Khodja

Published online: 20 Dec 2021.

Submit your article to this journal ⟋

View related articles ⟋

View Crossmark data ⟋

Taylor & Francis
Taylor & Francis Group

Check for updates

# Structural, elastic, electronic and optical investigations of fluoride-perovskite NaBeF₃: first-principles calculations

K. Hamada, T. Djaafri ⬤, A. Bendjedid, A. Djaafri, F. Saadaoui and D. Khodja

Laboratoire des Etudes Physico-Chimiques, Université Dr. Moulay Tahar, Saida, Algeria

**ABSTRACT**

The investigations of the pressure effects on structural, elastic, electronic and optical properties of fluoride-perovskite $NaBeF_3$ are carried out for the first time using the full-potential linearised augmented plane wave plus local orbitals (FP-LAPW + lo) implemented in the Wien2K code. Local density approximation, generalised gradient approximation (GGA), EV-GGA and modified Becke–Johnson (mBJ) approaches are adopted to incorporate the exchange and correlation potential. The calculated structural properties are in good agreement with the previous results. The predicted indirect band gap ($R$–$\Gamma$) is 11.87 eV for $NaBeF_3$ indicating the insulating behaviour of the fluoride perovskite. The calculated formation and cohesion energies assert that this compound can be experimentally realised. The elastic properties indicate that $NaBeF_3$ alloy is mechanically stable, ductile and anisotropic with a mixed bonding nature. The computed optical properties are in line with the Penn model and reveal its transparency for a large interval of energies. The investigation of the pressure effects on some physical properties of the studied alloy reveals that the compressibility module and the energy gaps increase with increasing pressure whereas the lattice constant decreases with increasing pressure. The investigated alloy can be used for high-frequency optical and optoelectronic devices.

## 1. Introduction

The class of materials having $ABX_3$ stoichiometry is recognised as perovskite compounds, where A is frequently alkali, alkaline or rare earth metals whereas B is usually transition, post-transition or non-transition metals whilst X anions are oxides or halides [1]. The perovskite alloys are light absorbers, though these class of compounds has been extensively studied for decades, but only recently, they have been used in LEDs, lasers and solar cells in a dye-sensitized cell applying the compound $CsSnI_3$ as a p-type hole transport layer [2].

Fluoro-perovskites $ABF_3$ exhibit an energy gap and transparency in the ultraviolet field; therefore, they have a huge potential in various technological applications such as optoelectronics, optical lithography, ferroelectricity, memory devices, superconductivity, photovoltaics, spintronics and highly efficient compounds used in solar cells [3–6]. Husain et al. presented for the first time a thorough investigation of the electronic, structural and mechanical properties of cubic fluoro-perovskites $ZnBiF_3$ and $ZnYF_3$ applying the density functional theory (DFT). They discovered that both the materials had a small band gap, were mechanically ductile and were structurally stable [7]. Fen Zhang et al. [8,9] revealed that the ternary fluoro-perovskites $LiMgF_3$, $BaLiF_3$, $KCaF_3$, $LiBaF_3$ and $RbBaF_3$ are good candidates for several technological applications in antiferromagnetic, ferroelectric, optical systems due to their large band gaps. The structural, electronic and mechanical behaviours of sodium-based fluoro-perovskites $NaXF_3$ ($X$ = Zn, Mg) have been investigated using Blaha-modified Becke–Johnson (mBJ) [10].

The ideal perovskite alloys $ABX_3$ crystallize in a simple cubic mesh of space group Pm-3m, where $A$ cations are located in the vertices of the cube, $B$ cations occupy the centre and the $X$ anions are placed on the face centres. The fluoro-perovskites structure like several other structures is very tolerant of numerous types of ionic substitution with the only condition that the local charge balance be preserved [11,12] (Figure 1).

The fluoro-perovskites can be synthesised by mixing alkali metal and alkaline earth metals with fluorine, as suggested by Bouamrane et al. [13], following the equation:
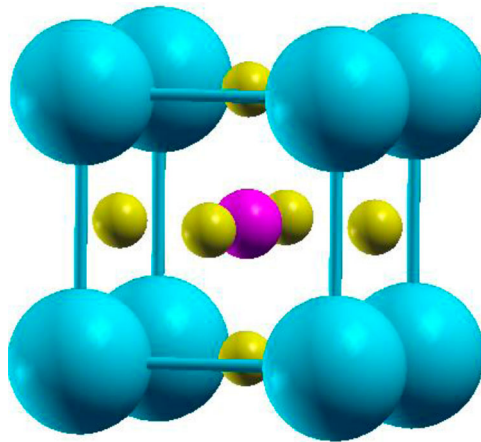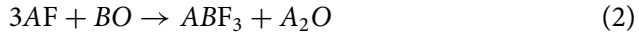
$$3AF + B \rightarrow ABF_3 + 2A \tag{1}$$



**Figure 1.** Crystal structures of $ABF_3$ alloy. Larger spheres stand for A atoms, smaller spheres symbolise F atoms, and medium spheres represent B atoms.

Whereas, Ludekens and Welch [14] proposed mixing metal halide with alkaline metal oxides, through the following reaction:

$$3AF + BO \rightarrow ABF_3 + A_2O \tag{2}$$

where $A$ is the alkali metals and $B$ is alkaline earth metals.

In this paper, we report for the first time, the investigation of the structural, electronic, elastic and optical properties of $NaBeF_3$ alloy applying the full-potential linearised augmented plane wave plus local orbitals (FP-LAPW + lo) implemented in the Wien2K code.

The calculated formation and cohesion energies asserted that this compound can be experimentally realised. The computed physical properties reveal that $NaBeF_3$ alloy can be a promising candidate for several technological applications.

## 2. Computational details

Calculations have been done by using the FP-LAPW + lo method within DFT as implemented in Wien2k code [15]. The local density approximation (LDA) of Honenberg and Kohn [16], the generalised gradient approximation (GGA) of Perdew, Burke and Ernzerhof [17], the Engel and Vosko approach [18] and the Tran–Blaha-modified Becke–Johnson (TB-mBJ) approximation [19] are used to treat the exchange–correlation potential. The unit cell was divided into two distinct regions, the interstitial region and atomic spheres. The values of the smallest muffin-tin radius $RMT$ are chosen to be proportional to their ionic radii such that the spheres do not overlap. These values are taken at 2.14, 1.52 and 1.52 a.u. for Na, Be and F atoms, respectively, in $NaBeF_3$ alloy. The optimisations of $k$-points and $RMT,Kmax$ are illustrated in Figures 2 and 3. Therefore, the calculations are performed with $8 \times 8 \times 8$ Monkhorst-Pack (MP) $k$-point mesh for the cubic structure (700 $k$-points) [20]. The adopted values of cut-off parameter $RMT,Kmax = 7.0$, where $Kmax$ gives the magnitude of the largest $K$ vector in the plane-wave expansion and $l = 10$ is used to control the expansion of the partial waves inside the muffin-tin spheres. The self-consistence calculations are considered to be converged only when the convergence tolerance of energy is $<10^{-4}$ Ry. The electronic configurations of each chemical element involved in the investigated compound are: Na: $3s^1$, Be: $2s^2$, F: $2s^2p^5$. $NaBeF_3$ alloy has cubic structure of space group Pm-3m (No 221), where the atoms are positioned at (0,0,0) for Na, (0.5,0.5,0.5) for Be and (0.5,0.5,0), (0.5,0,0.5), (0,0.5,0.5) for F, as shown in Figure 1. The lattice constants values are computed using Murnaghan's equation of state [21], although the bulk modulus values are estimated by fitting the pressure-volume data to a third-order Birch equation of state [22].
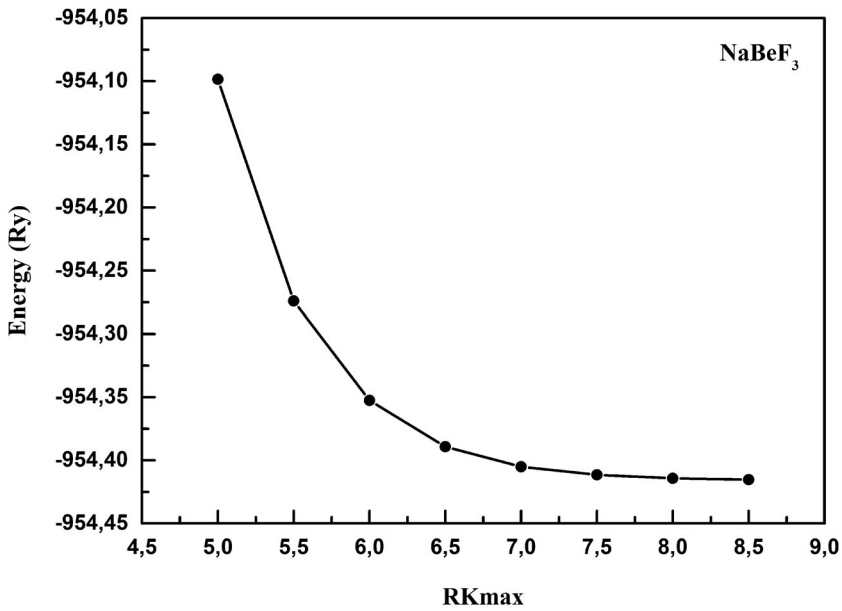
Figure 2. Variation of total energy as a function of RKmax for NaBeF$_3$ alloy.
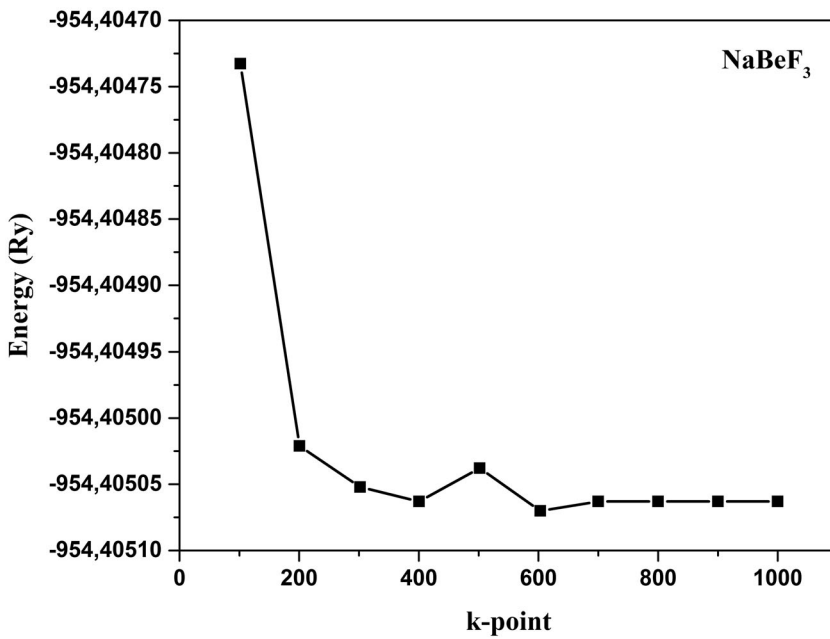


Figure 3. Variation of total energy as a function of the $k$-points for NaBeF$_3$ alloy.

## 3. Results of calculations

### 3.1. Structural properties

Firstly, we have investigated the variation of total energy as a function of volume as shown in Figure 4 to predict the equilibrium lattice constant ($a_0$),

bulk modulus ($B_0$) and its pressure derivative ($B'$) by fitting the obtained data to the Murnaghan's equation of state given by the following relation [23]

$$E(V) = E_0 + \frac{B_0}{B'(B'-1)}\left[V\left(\frac{V_0}{V}\right)^{B'} - V_0\right] + \frac{B_0}{B'}(V - V_0) \qquad (3)$$

The structural parameters evaluated within LDA and GGA approaches are gathered in Table 1. Obviously, the calculated lattice constants ($a_0$) are in good agreement with the previous computational results. Furthermore, the ground state energies ($E_{min}$) computed using LDA and GGA approaches are lower when compared with those obtained previously [24]. The bulk modulus ($B_0$) is one of the most important factor physics and engineering, it is computed to measure and investigate the hardness and brittleness of materials; larger is the bulk modulus, higher is the material hardness. The values of the bulk modulus ($B_0$) of $NaBeF_3$ alloy are higher than that of $RbBaF_3$ ($B_0 = 25.651$ GPa), thus $NaBeF_3$ alloy is more rigid than $RbBaF_3$ alloy [24]. Bulk modulus ($B_0$) is defined as the proportion of volumetric stress related to the volumetric strain for any material. From Table 1, it is remarkable that the bulk modulus ($B_0$) increases with the lattice parameter decrease. The pressure derivative ($B'$) of the bulk modulus is used to determine the thermoelastic properties of materials at high pressures and high temperatures [24].
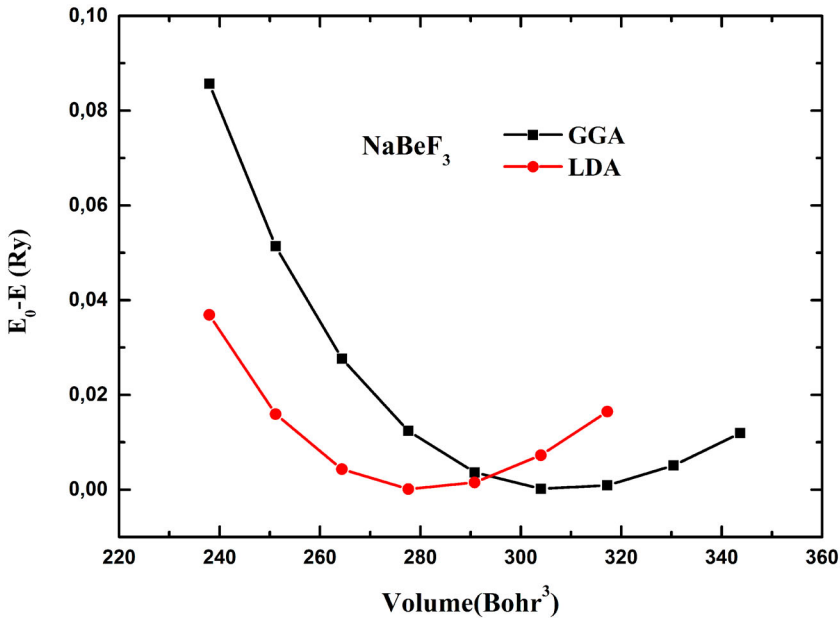


**Figure 4.** Variation of total energy as a function of volume for $NaBeF_3$ alloy using GGA and LDA approaches.

**Table 1.** Calculated equilibrium lattice constant ($a_0$), bulk modulus ($B_0$), its pressure derivative ($B'$), ground state energy ($E_{min}$), formation energy ($E_F$) and cohesion energy ($E_C$) of NaBeF$_3$ alloy, compared to available theoretical data.

| NaBeF$_3$ | $a_0$ (Å) | $B_0$ (GPa) | $B'$ | $E_{min}$ (eV) | $E_F$ (eV) | $E_C$ (eV) |
|---|---|---|---|---|---|---|
| LDA | 3.4641 | 124.5541 | 4.2580 | −12,916.9798 | −2.422 | 20.987 |
| GGA | 3.5739 | 101.6947 | 3.9061 | −12,984.3625 | | |
| Others | 3.3963 [24] | 147.289 [24] | | −14,489.9048 [24] | | |

In order to examine the possible experimental formation of NaBeF$_3$ alloy, we have predicted its formation energy $E_F$ with the following expression [25]:

$$E_F = E_{total} - (E_b(\text{Na}) + E_b(\text{Be}) + 3E_b(\text{F})) \qquad (4)$$

where $E_b$ is the energy per atom and $E_{total}$ is the total energy of primitive cell. The computed $E_F$ of NaBeF$_3$ alloy is −2.422 (eV). This negative value signifies that the synthesis of NaBeF$_3$ alloy is energetically favourable and consequently it can be easily experimentally fabricated.

The cohesive energy $Ec$ is predicted to inspect the structural stability of NaBeF$_3$ alloy after its experimental formation. $Ec$ is calculated utilising the following formula [26]:

$$E_c = (E_a(\text{Na}) + E_a(\text{Be}) + 3E_a(\text{F})) - E_{total} \qquad (5)$$

where $E_a$ symbolises the energy of an isolated atom. The obtained value of $E_c$ is about 20.987 (eV). This positive value indicates that NaBeF$_3$ alloy is structurally stable, namely, the chemical bonds ensuring the cohesion of the compound can be easily stabilised after its experimental formation.

## 3.2. Elastic properties

The elastic properties are related to the elastic parameters, which measure the proportionality between strain and stress in a solid. Computationally, the elastic parameters are estimated by applying a strain to a solid, measuring the energy as a function of the strain and determining the elastic parameters from the curvature of this function at zero strain [27,28]. They provide information on the nature of the forces operating in the solid, the rigidity, the stability and the anisotropy of solid. $C_{11}$, $C_{12}$ and $C_{44}$ are three independent elastic constants characterising the elastic properties for cubic systems, including diamond. $C_{11}$ typifies the elasticity in length, whilst $C_{44}$ and $C_{12}$ characterise the elasticity in shape. The conditions used to verify the elastic stability of cubic solids are the Born's stability criteria's: $C_{11} > 0$, $C_{44} > 0$, $C_{11} > C_{12}$, ($C_{11} + 2C_{12} > 0$) [29]. Furthermore, the derived parameters from the independent elastic constants $C_{ij}$, for instance, Young's modulus $E$, shear modulus $G$ and shear

anisotropic factor $A$ are also estimated with the following relations [30]:

$$G_V = \frac{C_{11} - C_{12} + 3C_{44}}{5} \tag{6}$$

$$G_R = \frac{5(C_{11} - C_{12})C_{44}}{4C_{44} + 3(C_{11} - C_{12})} \tag{7}$$

$$G = \frac{G_V + G_R}{2} \tag{8}$$

$$B = \frac{C_{11} + 2C_{12}}{3} \tag{9}$$

$$E = \frac{9BG}{3B + G} \tag{10}$$

$$A = \frac{2C_{44}}{C_{11} - C_{12}} \tag{11}$$

The elastic parameters calculated within the LDA and GGA approaches for NaBeF$_3$ alloy are grouped in Table 2. Since the investigated material satisfies all the Born's stability criteria's then it is mechanically stable. Pugh suggests that the compound is ductile when the ratio $B/G > 1.75$, whereas the opposite is associated with brittle. According to the calculated values listed in Table 3, the ratio $B/G$ is >1.75, thus NaBeF$_3$ alloy is ductile. Moreover, the positive Cauchy pressure ($C_{12} - C_{44}$) proves its ductility [30].

The anisotropy characterises the dependence of the properties of a substance on the direction. To predict the elastic anisotropy of this compound, we have computed the anisotropy factor $A$, for $A$ equals to 1, the material is considered as totally isotropic, whilst the deviation from 1 typifies the degree of the elastic anisotropy [31]. Obviously, the calculated values of $A$ are 0.15 and 0.2 using LDA and GGA approaches, respectively. Therefore, NaBeF$_3$ alloy has a low degree of anisotropy.

The Young modulus $E$ is a mechanical parameter that quantifies the tensile stiffness of a material and characterises the relationship between tensile stress and axial strain in the linear elastic region of a material. The solid is described as rigid when $E$ is higher [32]. The obtained results of $E$ (131.6765 LDA, 109.997 GGA) illustrate that NaBeF$_3$ is more rigid than RbBaF$_3$ alloy (50.09 LDA and 48.75 GGA) [24].

**Table 2.** Calculated elastic constant $C_{ij}$ at equilibrium volume for NaBeF$_3$ alloy.

| NaBeF$_3$ | $C_{11}$ (GPa) | $C_{12}$ (GPa) | $C_{44}$ (GPa) |
|---|---|---|---|
| LDA | 160.8870 | 108.646 | 96.0040 |
| GGA | 123.9115 | 89.6445 | 85.4273 |

**Table 3.** Computed bulk modulus $B_0$, shear modulus $G$, Young's modulus $E$, anisotropy factor $A$ and Pugh's ratio $B/G$ of NaBeF$_3$ alloy.

| NaBeF$_3$ | $B_0$ (GPa) | $G$ (GPa) | $E$ (GPa) | $A$ | $B/G$ |
|---|---|---|---|---|---|
| LDA | 126.06 | 57.2127 | 131.676 | 3.6754 | 2.2033 |
| GGA | 101.06 | 45.5187 | 109.997 | 4.9859 | 2.2203 |

### 3.3. Electronic properties

### 3.3.1. Band structure

To predict the electronic properties, we have inspected the electronic band structures using LDA, GGA, EV-GGA and mBJ approaches for NaBeF$_3$ alloy as illustrated in Figure 5. The band structure illustrates the possible energies of an electron as a function of the wave vector. The mBJ appears mainly in the conduction bands. Usually, it is used to correct the well-known underestimation of the GGA, LDA and EV-GGA approximations on the band gap and gives gap values fairly close to the experimental one.

Obviously, the minimum of the conduction bands is situated at the Γ point of the Brillouin zone, whereas the maximum of the valence band is located at the symmetry point R, thus, NaBeF$_3$ alloy exhibits an indirect band gap ($R$–$\Gamma$) about 11.8722 eV computed by mBJ significantly higher than those obtained by GGA (7.4555 eV), LDA (7.8144 eV) and EV-GGA (8.5577 eV) as shown in Table 4.
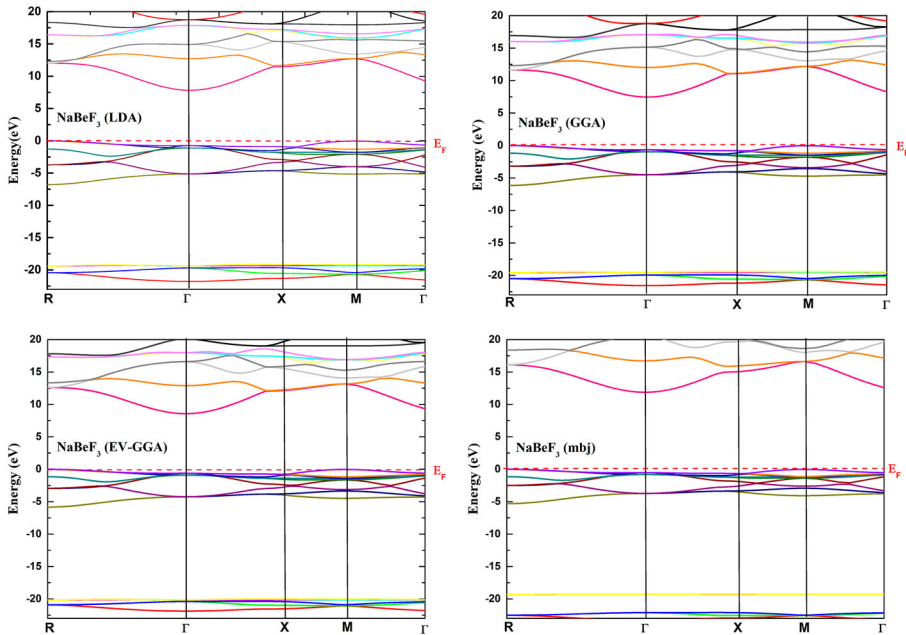


**Figure 5.** Electronic band structures of NaBeF$_3$ alloy calculated using the LDA, GGA, EV.GGA and mBJ approaches.

### 3.3.2. Densities of states

To further depict the electronic distributions of different states and the origin of band structure, the partial and total density of states are also studied and illustrated in Figure 6 for $NaBeF_3$ alloy predicted by the EV-GGA and mBJ approaches in the range of energy $[-24, 20\ eV]$. Obviously, the total densities of states are the result of the contribution of each partial density of states. Visibly, the main peaks in total densities of states maintain approximately the same locations as in the partial densities of states. Noticeably, the states of the valence band close to Fermi level are largely formed by F-p states with a very weak contribution from Be-d and Be-p states; whereas, the contributions of Na-p states and F-s states are located mainly in the lowest parts of the total densities of states at $-20$ and $-22\ eV$, respectively. In the conduction band, the total densities of states are dominated by the Be-p, whilst the contributions of Be-s and d states are small.

### 3.3.3. Electronic charge density

Electron density denotes the nature of the bond between different atoms. In order to predict the bonding forces and the charge transfer in $NaBeF_3$ alloy, the charge density behaviours in 2D and 3D are computed in the (110) plane for this compound and have been depicted in Figure 7. There is an interaction between the charges of F and Be caused by the hybridisation between the p orbitals of halogen F, and the p and s orbitals of Be, due to the high electronegativity of the halogen F. Thus, the bonding forces are covalent between Be and halogen F. The charge distribution in the F anion and Na cation is totally spherical which reveals the strong ionic nature of the F–Na bond; furthermore, the charge is transferred from the Na cation to F anion caused by the large difference in electronegativities. This alloy is of mixed ionic and covalent type.

### 3.4. Optical properties

The complex dielectric function is directly connected to the energy band structure of solids. The optical spectroscopy investigation is a great means to denote the overall band feature of a solid. Thus, precise FP-LAPW computations are attractive to comprehend the optical spectra. Whilst $NaBeF_3$ alloy is characterised by a cubic symmetry, it is sufficient to calculate only one component of the dielectric tensor, which can entirely establish the linear optical properties. Most

**Table 4.** Computed values of the different gaps of $NaBeF_3$ alloy using LDA, GGA, EV-GGA and mBJ approaches.

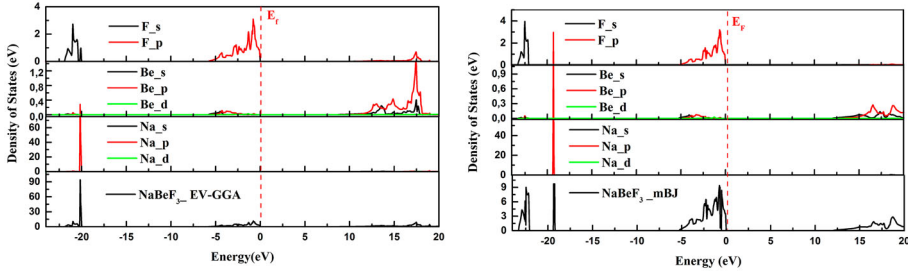| Energy gaps (eV) | | | | | |
|---|---|---|---|---|---|
| R–Γ | M–M | X–X | R–R | Γ–Γ | $NaBeF_3$ |
| 7.8144 | 12.7623 | 12.3421 | 12.0208 | 8.5475 | LDA |
| 7.4555 | 12.2191 | 11.8295 | 11.6422 | 8.11014 | GGA |
| 8.5577 | 13.1876 | 12.8032 | 12.6089 | 9.1809 | EV-GGA |
| 11.8722 | 16.6461 | 15.6314 | 16.1194 | 12.4002 | mBJ -GGA |

**Figure 6.** Projected DOS diagrams of the NaBeF$_3$ alloy computed using the EV-GGA and mBJ approaches.

of the optical properties such as the reflectivity, the absorption coefficient, the refractivity index can be predicted from the complex dielectric function [33,34]:

$$\varepsilon(\omega) = \varepsilon_1(\omega) + j\varepsilon_2(\omega) \qquad (12)$$

where $\omega$ is the frequency and $\varepsilon_1(\omega)$ and $\varepsilon_2(\omega)$ are the real and imaginary parts of the dielectric function $\varepsilon(\omega)$ at zero pressure, respectively.

$\varepsilon_2(\omega)$ is given by the relation

$$\varepsilon_2(\omega) = \left(\frac{4\pi^2 e^2}{m^2\omega^2}\right) \sum_{i,j} i|M|j^2 f_i(1 - f_i)\delta(E_{f-}E_i - \omega)d^3k \qquad (13)$$

where the integral is taken over the first Brillouin zone and $\delta(E_f - E_i - \omega)$ is the condition for the conservation of total energy, $i$ and $j$ are the initial and final states, respectively, $M$ is the dipole matrix and $f_i$ is the Fermi distribution function. The real part of the complex dielectric function $\varepsilon_1(\omega)$ is calculated
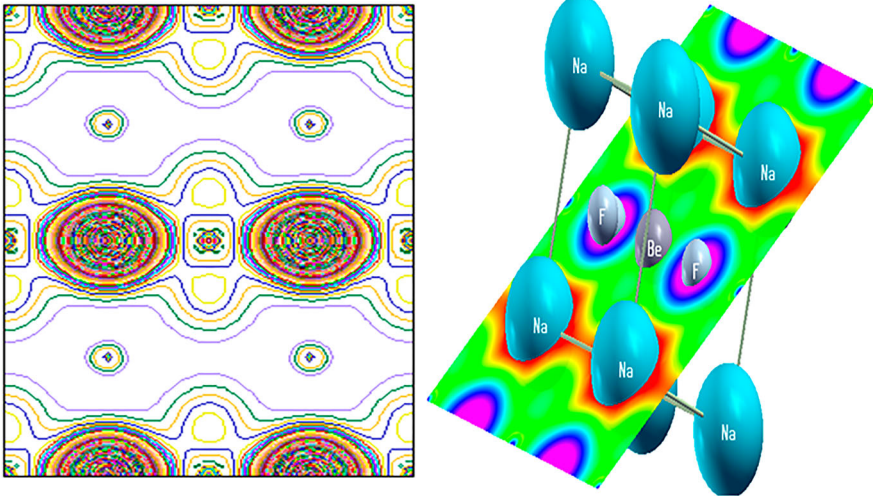


**Figure 7.** The mBJ valence charge density plots (2D and 3D) for the NaBeF$_3$ alloy in the (110) plane.

**Table 5.** Different static optical properties.

| Compounds | $\mathscr{E}_1(0)$ | $n(0)$ | $R(0)$ |
|---|---|---|---|
| NaBeF$_3$ | 1.56 | 1.253 | 0.013 |

from the imaginary part $\varepsilon_2(\omega)$ using the Kramers–Kronig relation [35,36] as:

$$\varepsilon_1(\omega) = 1 + \frac{2}{\pi} p \int_0^\infty \frac{\omega' \varepsilon_2(\omega')}{\omega'^2 - \omega^2} \, d\omega' \tag{14}$$

where $P$ implies the most important value of the integral. The other optical properties, such as the refractive index $n(\omega)$, the absorption coefficient $I(\omega)$ and the reflectivity $R(\omega)$, are obtained from the dielectric function using mBJ approach, which provides a gap energies close to the experience. The computed results are gathered in Table 5. The optical properties are closely related to the band structure.

Figure 8(a) illustrates the spectrum of the real $\varepsilon_1(\omega)$ and imaginary $\varepsilon_2(\omega)$ parts of the complex dielectric function versus the photon energy of NaBeF$_3$ alloy in the interval [0, 40 eV]. The analysis of this spectrum in terms of electronic structure, shown in Figure 5, discloses the manner by which this alloy absorbs the incident radiation.
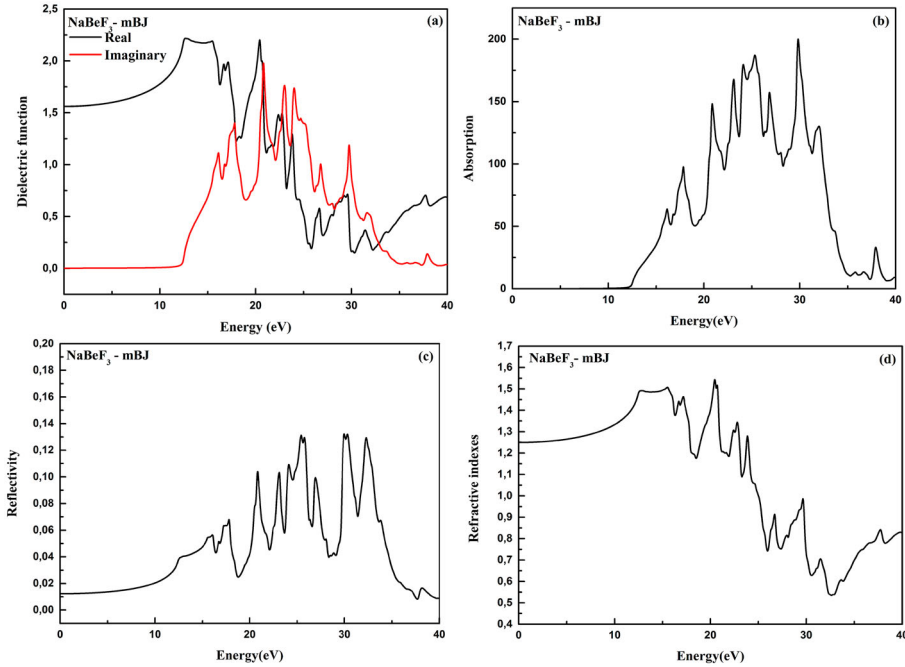


**Figure 8.** The real and imaginary parts of dielectric function, absorption, reflectivity and refractive index of NaBeF$_3$ alloy using mBJ approach.

Obviously, $\varepsilon_1(\omega)$ increases with increasing photon energy to reach the highest peak of 2.23 at 12.69 eV. The analysis of the peaks of the imaginary part curve of the dielectric function, which is related to the electronic transitions from the occupied to the unoccupied states [37], reveals that the first peak of 12.29 occurs at about 16.25 eV and the highest once of 19.95 at 21.86 eV, which is related to the direct transition (Γ–Γ) between the lowest conduction band and the highest valence band. The peaks at 16.10 and 17.74 eV are caused by the interband transitions along the band gap (R–R) and (M–M) in the band structures, respectively.

From Figure 8(b), illustrating the absorption coefficient as a function of the energy, we perceive that there are high absorptions peaks at high energies located in the energy interval [19,32 eV] for $NaBeF_3$ alloy. The optical gap is around 12.29 eV for $NaBeF_3$ alloy, thus, this fluoro-perovskite has high optical absorption.

The computed reflectivity $R(\omega)$ is represented in Figure 8(c). This curve demonstrates that the maximum reflectivity is at 32.1 eV. From this curve, the zero-frequency limit of reflectivity is found to be 0.013, showing that the reflectivity starts at very small values about 4% at 12.72 eV, whereas the maximum of about 13.3% is located at 30.14 eV. At higher energy, the reflectivity decreases quickly, the investigated alloy can be used for high-frequency optical and optoelectronic devices and as possible materials for ultraviolet rays.

The most significant parameter amongst the other computed optical constants is the refractive index, which is connected with the linear electro-optical coefficient which determines the photorefractive sensitivity. The dispersion curve of refractive index for $NaBeF_3$ alloy along the three different directions is illustrated in Figure 8(d). This compound in low energy shows a maximum value of refractive indices. Noticeably, the refraction index attains higher values for the energies close to the absorption threshold.

The static values obtained from these curves of the real dielectric function $\varepsilon_1(0)$, refractive index $n(0)$ and the reflectivity $R(0)$ are presented in Table 5.

## 3.5. Pressure effects

In 1996, Schwarz et al. [38] investigated the pressure effects on the optical absorption gaps and the crystal structures of $CsGeBr_3$ and $CsGeCl_3$ alloys, they observed that the band gaps of $CsGeBr_3$ and $CsGeCl_3$ alloys decrease with pressure increase.

In this regard, we present a thorough study of the pressure effects on the physical properties such as electronic, structural and elastic features in the pressure range [0, 25 GPa]. The pressure effects on the lattice parameter, the energy gaps and compressibility module are shown in Figures 9 and 10. Obviously, the lattice constant decreases with increasing pressure, whereas
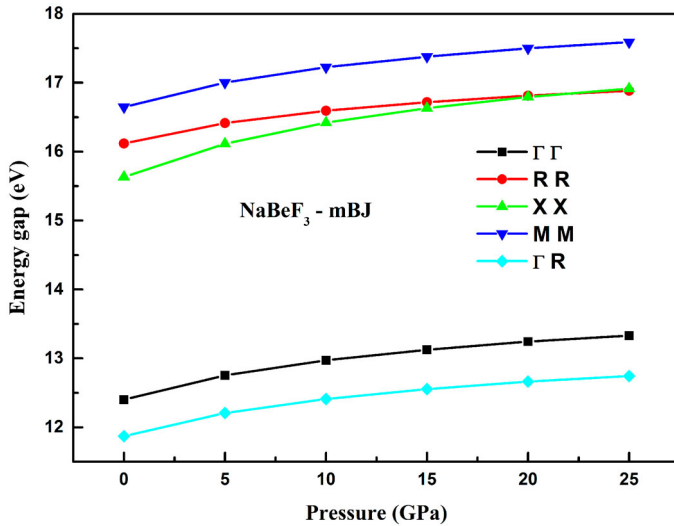
**Figure 9.** Direct and indirect band gap energies versus pressure for NaBeF$_3$ alloy.
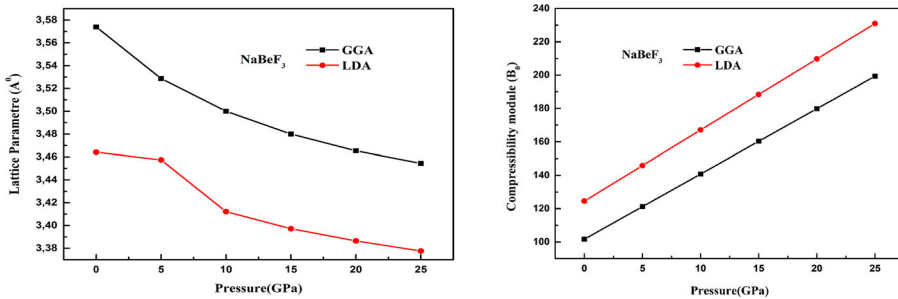


**Figure 10.** Lattice parameter and compressibility module as a function of the pressure of NaBeF$_3$ alloy.

the compressibility module increases with pressure increase, whilst, the energy gaps increase slowly with increasing pressure.

## 4. Conclusions

Computations concerning structural, elastic, electronic and optical properties of fluoride-perovskite NaBeF$_3$ are carried out within the FP-LAPW approaches as performed in Wien2K package. From the electronic properties, it is obvious that the investigated alloy exhibits a wide indirect band gap ($R$–$\Gamma$) about 11.8722 eV computed by mBJ approach significantly higher than those obtained by GGA, LDA and EV-GGA approximations. The calculated results accord well with those of the previous values. Obviously, the states of the valence band close to Fermi level are largely formed by F-p states, whereas, in the conduction band, the total densities of states are dominated

by the Be-p states. The calculated formation and cohesion energies assert that this compound can be experimentally realised. The elastic constants $C_{ij}$ are calculated via the stress–strain method. Since $NaBeF_3$ alloy is cubic compound and the Born's stability criteria's are satisfied then the compound is mechanically stable. The calculated values of Cauchy pressure ($C_{12}$–$C_{44}$) and Pugh's ratio $B/G$ reveal that $NaBeF_3$ alloy is ductile. The investigation of the electron charge density proves that this alloy has a mixed bonding nature. The computed results illustrate that $NaBeF_3$ alloy is more rigid than $RbBaF_3$ alloy and it has a low degree of anisotropy. The dispersion of imaginary part of the dielectric function reveals its transparency for a large interval of energies. Finally, the study of the pressure effects on some physical properties in the pressure range [0, 25 GPa] reveals that the lattice constant decreases with increasing pressure, whereas the compressibility module increases with pressure increase. The energy gaps increase slowly with increasing pressure. The investigated alloy can be used for high-frequency optical and optoelectronic devices.

## Disclosure statement

## ORCID

*T. Djaafri* 🆔 http://orcid.org/0000-0001-7965-4792

## References

[1] R. El Ouenzerfi, S. Ono, A. Quema, M. Goto, M. Sakai, N. Sarukura, T. Nishimatsu, N. Terakubo, H. Mizuseki, Y. Kawazoe, et al., *Design of wide-gap fluoride heterostructures for deep ultraviolet optical devices*. J. Appl. Phys. 96 (2004), pp. 7655–7659.

[2] W.J. Yin, J.H. Yang, J. Kang, Y. Yan and S.H. Wei, *Halide Perovskite materials for solar cells:a theoretical review*. J. Mater. Chem. A. 3 (2015), pp. 8926–8942.

[3] I. Chung, B. Lee, J. He, R.P.H. Chang and M.G. Kanatzidis, *All-solid-state dye-sensitized solar cells with high efficiency*. Nature 485 (2012), pp. 486–489.

[4] N.K. Noel, S.D. Stranks, A. Abate, C. Wehrenfennig, S. Guarnera, A.A. Haghighirad, A. Sadhanala, G.E. Eperon, S.K. Pathak, M.B. Johnston, et al., *Lead-free organic–inorganic tin halide perovskites for photovoltaic applications*. Energy Environ. Sci. 7 (2014), pp. 3061–3068.

[5] A.C. Garcia-Castro, N.A. Spaldin, A.H. Romero and E. Bousquet, *Geometric ferroelectricity in fluoro-perovskites*. Phys. Rev. B 89 (2013), pp. 1–6.

[6] W. Shockley and H.J. Queisser, *Detailed balance limit of efficiency of p-n junction solar cells*. J. Appl. Phys. 32 (1961), pp. 510–519.

[7] A. Hadj-Larbi, S. Hiadsi, M. Hadjab and M.A. Saeed, *Optical study of cubic, and orthorhombic structures of XCaCl₃ (X = K, Rb) compounds: comparative ab initio calculations*. Optik. (Stuttg) 166 (2018), pp. 169–176.

[8] F. Zhang, S. Chen, C. Lin and Y. Yin, *Anodic-hydrothermal preparation of prism-shaped CaTiO₃ structure on titanium surface*. Appl. Surf. Sci. 257 (2011), pp. 3092–3096.

[9] F. Zhang, Y. Mao, T.-J. Park and S.S. Wong, *Green synthesis and propertycharacterization of single-cristalline Perovskite Fluoride Nanorods*. Adv. 18 (2008), pp. 103–112.

[10] P. Blaha, K. Schwarz, G.K.H. Madsen, D. Kvasnicka and J. Luitz, *WIEN2k, An Augmented Plane Wave Plus Local Orbitals Program for Calculating Crystal Properties*, 2nd ed., Vienna University of Technology, Vienna, 2001.

[11] E. Sjöstedt, L. Nordström and D.J. Singh, *An alternative way of linearizing the augmented plane-wave method*. Solid State Commun. 114 (2000), pp. 15–20.

[12] P. Hohenberg and W. Kohn, *Inhomogeneous electron gas*. Phys. Rev. B 136 (1964), pp. 864–871.

[13] A. Bouamrane, J.P. Laval, J.-P Soulie and J.P. Bastide, *Structural characterization of NaMgH₂F and NaMgH₃*. Mater. Res. Bull. 35 (2000), pp. 545–549.

[14] W.L.W. Ludekens and A.J.E. Welch, *Reactions between metal oxides and fluorides: some new double-fluoride structures of type ABF₃*. Acta Crystal. 5 (1952), pp. 841.

[15] J.P. Perdew, K. Burke and M. Ernzerhof, *Generalized gradient approximation made simple*. Phys. Rev. Lett. 77 (1996), pp. 3865–3868.

[16] E. Engel and S.H. Vosko, *Exact exchange-only potentials and the virial relation as microscopic criteria for generalized gradient approximations*. Phys. Rev. B 47 (1993), pp. 13164–13174.

[17] F. Tran and P. Blaha, *Accurate band gaps of semiconductors and insulators with a semi-local exchange-correlation potential*. Phys. Rev. Lett. 102 (2009), pp. 226401.

[18] P.E. Blochl, O. Jepsen and O.K. Andersen, *Improved tetrahedron method for Brillouin-zone integrations*. Phys. Rev. B 49 (1994), pp. 16223–16233.

[19] F.D. Murnaghan, *The compressibility of media under extreme pressures*. Proc. Natl Acad. Sci. USA 30 (1944), pp. 244–247.

[20] J.F. Nye, *Physical Properties of Crystals: Their Representation by Tensors and Matrices*, Oxford University Press, Oxford, 1985.

[21] G.J. Ackland, *High-pressure phases of group IV and III–V semiconductors*. Rep. Prog. Phys. 64 (2001), pp. 483–516.

[22] M.J. Mehl, J.E. Osburn, D.A. Papaconstantopoulous and M.B. Klein, *Structural properties of ordered high-melting-temperature intermetallic alloys from first-principles total-energy calculations*. Phys. Rev. B 41 (1990), pp. 10314–10323.

[23] L.D. Landau and E.M. Lifshitz, *Theory of Elasticity*. 3rd English ed. Nauka, Moscow, 1987.

[24] R. Hill, *The elastic behaviour of a crystalline aggregate*. Proc. Phys. Soc. A 65 (1952), pp. 349–354.

[25] X. Wang, Z. Cheng, G. Liu, X. Dai, R. Khenata, L. Wang and A. Bouhemadou, *Rare earth-based quaternary heusler compounds MCoVZ (M = Lu, Y; Z = Si, Ge) with tunable band characteristics for potential spintronic applications*. IUCrJ 4 (2017), pp. 758–768.

[26] S. Hiadsi, H. Bouafia, B. Sahli, B. Abidri, Bouaza A. and A. Akriche, *Structural, mechanical, electronic and thermal properties of KZnF3 and AgZnF3 perovskites: FP-(L)APW + lo calculations*. Solid State Sci. 58 (2016), pp. 1–13.

[27] S.F. Pugh, *XCII. Relations between the elastic moduli and the plastic properties of polycrystalline pure metals*. London, Edinburgh, Dublin Philos. Mag. J. Sci. 45 (1954), pp. 823–843.

[28] D.G. Pettifor, *Theoretical predictions of structure and related properties of intermetallics*. Mater. Sci. Technol. 8 (1992), pp. 345–349.

[29]  W. Voigt, *Lehrbuch der Kristallphysik*, B.G. Teubner, Leipzig, 1928.

[30]  A. Reuss and Z. Angew, *Berechnung der Fließgrenze von Mischkristallen auf Grund der Plastizitätsbedingung für Einkristalle*. J. A. Math. Mech. 9 (1929), pp. 49–58.

[31]  M. Sahnoun, M. Zbiri, C. Daul, R. Khenata, H. Baltache and M. Driz, *Full potential calculation of structural, electronic and optical properties of KMgF$_3$*. Mater. Chem. Phys. 91 (2005), pp. 185–191.

[32]  F. Birch, *Finite strain isotherm and velocities for single-crystal and polycrystalline NaCl at high pressures and 300°K*. J. Geophys. Res.: Solid Earth 83 (1978), pp. 1257–1268.

[33]  H. Ehrenreich and M.H. Cohen, *Self-consistent field approach to the many-electron problem*. Phys. Rev. 115 (1959), pp. 786–790.

[34]  M. Dressel and G. Gruner, *Electrodynamics of Solids: Optical Properties of Electrons in Matter*, Cambridge University Press, UK, 2002.

[35]  R. Abt, C. Ambrosh-Draxl and P. knoll, *Optical response of high temperature superconductors by full potential LAPW band structure calculations*. Physica B 194 (1994), pp. 1451–1452.

[36]  R. Padmavathy, A. Amudhavalli, R. Rajeswarapalanichamy and K. Iyakutti, *Electronic and optical properties of cubic perovskites CsPbCl$_{3-y}$I$_y$ (y = 0, 1, 2, 3)*. Z. Naturforsch. 74 (10) (2019), pp. 905–913.

[37]  de L. Kronig R., *On the theory of dispersion of X-rays*. J. Opt. Soc. Am. 12 (1926), pp. 547–557.

[38]  U. Schwarz, F. Wagner, K. Syassen and H. Hillebrecht, *Effect of pressure on the optical-absorption edges of CsGeBr$_3$ and CsGeCl$_3$*. Phys. Rev. B 53 (1996), pp. 12545–12548.

**Abstract**:

The investigations of the strain effects on magnetism, elasticity, electronic, optical and thermodynamic properties of PdVTe half-Heusler alloy are carried out using the most accurate methods to electronic band structure, i.e. the full-potential linearized augmented plane wave plus a local orbital (FP-LAPW + lo) approach. The analysis of the band structures and the density of states reveals the Half-metallic behavior with a small indirect band gap $E_g$ of 0.51 eV around the Fermi level for the minority spin channels. The study of magnetic properties led to the predicted value of total magnetic moment $\mu_{tot} = 3\mu_B$, which nicely follows the Slater–Pauling rule $\mu_{tot} = Z_t$ -18. Several optical properties are calculated for the first time and the predicted values are in line with the Penn model. It is shown from the imaginary part of the complex dielectric function that the investigated alloy is optically metallic. The variations of thermodynamic parameters calculated using the quasi-harmonic Debye model, accord well with the results predicted by the Debye theory. Moreover, the dynamical stability of the investigated alloy is computed by means of the phonon dispersion curves, the density of states, and the formation energies. Finally, the analysis of the strain effects reveals that PdVTe alloy preserves its ferromagnetic half metallic behavior, it remains mechanically stable, the ionic nature dominates the atomic bonding, and the thermodynamic and the optical properties keep the same features in a large interval of pressure.

**Résumé :**

L'étude de l'effet de la déformation sur le magnétisme, l'élasticité, et les propriétés électroniques, optiques et thermodynamiques de l'alliage semi-Heusler PdVTe sont effectuées en utilisant la méthode les plus précises basée sur les structure de bande électronique, c'est-à-dire l'onde plane augmentée linéarisée à plein potentiel plus l'orbitale locale (FP-LAPW + lo). L'analyse des structures de bande et de la densité d'états révèle le comportement semi-métallique avec une petite bande interdite indirecte Eg de 0,51 eV autour du niveau de Fermi pour les spins minoritaires. L'étude des propriétés magnétiques a conduit à la valeur prédite du moment magnétique total $\mu_{tot} = 3\mu_B$, qui suit bien la règle de Slater–Pauling $\mu_{tot} = Z_t$ -18. Plusieurs propriétés optiques sont calculées pour la première fois et les valeurs obtenues sont en bon accord avec le modèle de Penn. A partir de la partie imaginaire de la fonction diélectrique complexe on peut constater que l'alliage étudié est optiquement métallique. Les variations des paramètres thermodynamiques calculées s'accordent bien avec les résultats prédits par la théorie de Debye. De plus, la stabilité dynamique de l'alliage étudié est calculée au moyen des courbes de dispersion des phonons, de la densité d'états des phonons et de l'énergie de formation. Enfin, l'analyse des effets de déformation révèle que l'alliage PdVTe conserve son comportement ferromagnétique et semi-métallique, il reste mécaniquement stable, la nature ionique domine la liaison atomique, et les propriétés thermodynamiques et optiques conservent les mêmes caractéristiques dans un grand intervalle de pression.

الخلاصة:

تمت دراسة تأثير الاجهاد على الخصائص المغناطيسية و المرونية و الالكترونية و الضوئية و الديناميكية الحرارية لشبه الهاسلر PdVTe باستخدام أكثر الطرق دقة. أجريت الحسابات على أساس مقاربة الكمون التام للموجات الخطية المتزايدة (FP-LAPW+lo) من خلال التحليل البنيوي لأشرطة الطاقة و كثافة المستويات المحسوبة من أجل المركب لوحظ سلوك نصف المعدني مع فجوة طاقوية صغيرة غير مباشرة بقيمة 0.51 فولط حول مستوى فارمي. الخصائص المغناطيسية الى القيمة المتوقعة للعزم المغناطيسي الكلي $\mu_{tot} = 3\mu_B$، و التي تتبع بشكل جيد قاعدة سلاتار و باولي المعطاة بالعلاقة التالية $\mu_{tot} = Z_t$ -18. تم حساب العديد من الخصائص البصرية لأول مرة و اليم المتوقعة تتماشى مع نموذج Penn. يتضح من الجزء التخيلي لوظيفة العزل الكهربائي المعقدة التي تم فحصها معدنيا بصريا. تتفق تغيرات المعاملات الديناميكية الحرارية المحسوبة بشكل جديد مع النتائج التي تنبأت بها نظرية ديباي. علاوة على ذلك يتم حساب الثبات الديناميكي للمادة التي تم فحصها عن طريق منحنيات تشتت الفونون، و كثافة الحالات، وطاقة التكوين. أخيرا يكشف تحليل تأثيرات الاجهاد أن PdVTe يحافظ على سلوكه النصف المعدني المغناطيسي، و يظل مستقرا ميكانيكيا، و تهيمن الطبيعة الايونية على الروابط الذرية، و تحتفظ الخصائص الديناميكية الحرارية و الخصائص البصرية على نفس الميزات في مجال كبير من الضغط.